

# Naval Research Laboratory

Stennis Space Center, MS 39529-5004



NRL/FR/7322--98-9682

## Coastal Tide Prediction Using the ADCIRC-2DDI Hydrodynamic Finite Element Model: Model Validation and Sensitivity Analyses in the Southern North Sea/English Channel

CHERYL ANN BLAIN

*Ocean Dynamics and Prediction Branch  
Oceanography Division*

W. ERICK ROGERS

*Planning Systems Incorporated  
Slidell, LA 70458*

December 18, 1998

19990114 038

Approved for public release; distribution unlimited.

# REPORT DOCUMENTATION PAGE

Form Approved  
OMB No. 0704-0188

Public reporting burden for this collection of information is estimated to average 1 hour per response, including the time for reviewing instructions, searching existing data sources, gathering and maintaining the data needed, and completing and reviewing the collection of information. Send comments regarding this burden or any other aspect of this collection of information, including suggestions for reducing this burden, to Washington Headquarters Services, Directorate for Information Operations and Reports, 1215 Jefferson Davis Highway, Suite 1204, Arlington, VA 22202-4302, and to the Office of Management and Budget, Paperwork Reduction Project (0704-0188), Washington, DC 20503.

1. AGENCY USE ONLY (Leave blank)	2. REPORT DATE	3. REPORT TYPE AND DATES COVERED	
	December 18, 1998	Final	
4. TITLE AND SUBTITLE Coastal Tide Prediction Using the ADCIRC-2DDI Hydrodynamic Finite Element Model: Model Validation and Sensitivity Analyses in the Southern North Sea/English Channel			5. FUNDING NUMBERS Job Order No. 573672008 Program Element No. 0602435N Project No. Task No. BE-35-2-15 Accession No. DN163783
6. AUTHOR(S) Cheryl Ann Blain and W. Erick Rogers*			
7. PERFORMING ORGANIZATION NAME(S) AND ADDRESS(ES) Naval Research Laboratory Oceanography Division Stennis Space Center, MS 39529-5004			8. PERFORMING ORGANIZATION REPORT NUMBER NRL/FR/7322--98-9682
9. SPONSORING/MONITORING AGENCY NAME(S) AND ADDRESS(ES) Office of Naval Research 800 N. Quincy St. Arlington, VA 22217-5000			10. SPONSORING/MONITORING AGENCY REPORT NUMBER
11. SUPPLEMENTARY NOTES *Planning Systems Incorporated, 115 Christian Lane, Slidell, LA 70458			
12a. DISTRIBUTION/AVAILABILITY STATEMENT Approved for public release; distribution unlimited.		12b. DISTRIBUTION CODE	
13. ABSTRACT (Maximum 200 words) Details of the barotropic hydrodynamic model, ADCIRC-2DDI, including formulation of the governing equations and their numerical solution are presented. Validation of ADCIRC-2DDI predicted tidal heights and currents in the North Sea/English Channel is undertaken in the context of the Tidal Flow Forum as outlined by Werner and Lynch (1988). Sensitivity studies examine the effects of nonlinear mechanisms, forms of the tidal forcing, and the behavior of various model parameters on the computed tidal response. Mesh resolution issues are also investigated in the context of tidal dynamics. Throughout this report, model experiments and the discussion of results are focused on improving understanding of the ADCIRC-2DDI hydrodynamic model and its application to coastal tide prediction.			
14. SUBJECT TERMS wave modeling, tide modeling, coupled waves and tides			15. NUMBER OF PAGES 96
			16. PRICE CODE
17. SECURITY CLASSIFICATION OF REPORT Unclassified	18. SECURITY CLASSIFICATION OF THIS PAGE Unclassified	19. SECURITY CLASSIFICATION OF ABSTRACT Unclassified	20. LIMITATION OF ABSTRACT Same as report

## CONTENTS

EXECUTIVE SUMMARY .....	E-1
1.0 INTRODUCTION .....	1
2.0 THE HYDRODYNAMIC MODEL .....	2
2.1 Criteria for Selection .....	2
2.2 Current Numerical Modeling Approaches .....	3
2.3 The ADCIRC-2DDI Hydrodynamic Model .....	4
3.0 THE TIDAL FLOW FORUM BENCHMARK CASE .....	11
3.1 Description .....	11
3.2 Field Observations .....	13
4.0 MODEL VALIDATION EXPERIMENTS .....	14
4.1 Description .....	14
4.2 Quantitative Analyses .....	14
4.3 Base Simulation .....	15
5.0 RESULTS FOR THE BASE SIMULATION .....	16
5.1 Elevation Time Series Comparisons .....	16
5.2 Velocity Time Series Comparisons .....	23
5.3 Performance Comparison to Other Models .....	24
6.0 SENSITIVITY ANALYSES .....	27
6.1 Description .....	27
6.2 Nonlinearities .....	27
6.3 Forcing .....	35
6.4 Parameters .....	40
6.5 Implementation of Wetting and Drying .....	46
7.0 MESH RESOLUTION ISSUES .....	49
7.1 Computation of Grid Errors .....	49
7.2 Sensitivity of Nonlinearities to Mesh Resolution .....	55

8.0 CONCLUSIONS .....	58
9.0 ACKNOWLEDGMENTS .....	59
10.0 REFERENCES .....	60
APPENDIX A — Raw Model-Data Elevation Comparisons for the Base Simulation .....	67
APPENDIX B — “Filtered” Model-Data Elevation Comparisons for the Base Simulation .....	71
APPENDIX C — Tidal Constituent Comparisons for the Base Simulation .....	75
APPENDIX D — Model-Data Velocity Comparisons for the Base Simulation .....	87

## **EXECUTIVE SUMMARY**

Details of the barotropic hydrodynamic model, ADCIRC-2DDI, including formulation of the governing equations and their numerical solution are presented. Validation of ADCIRC-2DDI predicted tidal heights and currents in the North Sea/English Channel is undertaken in the context of the Tidal Flow Forum as outlined by Werner and Lynch (1988). Sensitivity studies examine the effects of nonlinear mechanisms, forms of the tidal forcing, and the behavior of various model parameters on the computed tidal response. Mesh resolution issues are also investigated in the context of tidal dynamics. Throughout this report, model experiments and the discussion of results are focused on improving understanding of the ADCIRC-2DDI hydrodynamic model and its application to coastal tide prediction.

# COASTAL TIDE PREDICTION USING THE ADCIRC-2DDI HYDRODYNAMIC FINITE ELEMENT MODEL: MODEL VALIDATION AND SENSITIVITY ANALYSES IN THE SOUTHERN NORTH SEA/ENGLISH CHANNEL

## 1.0 INTRODUCTION

Numerical modeling has become an essential tool for assessing the hydrodynamics of continental margin waters. It is important to recognize that the computed response of these waters is controlled by the various components that make up the model, including the governing equations, boundary conditions, forcing functions, discrete equations, grid structure, and the computational domain itself. The more that is understood about a numerical model, how its various components influence computations and is put into practice, the more successful the model will be in representing hydrodynamic processes within shallow waters. The work described herein focuses on the numerical modeling of tidal circulation in coastal waters. In particular, sensitivities of the tidal elevations and currents computed by the ADCIRC-2DDI hydrodynamic model simulator are investigated. Important considerations in the numerical modeling of tidal dynamics are the capture of nonlinear interactions, the specification of boundary conditions, and the adequacy of the grid resolution. The North Sea Benchmark (Werner and Lynch 1988) provides the backdrop for this sensitivity study and validation of tidal predictions. Results included herein provide guidelines for future applications of the ADCIRC-2DDI hydrodynamic model to the simulation of tidal circulation in the coastal ocean.

Tides are long period waves generated by gravitational forces of the sun and the moon on the ocean waters (Hendershott 1981). The period, wavelength, and amplitude characteristics of the tide depend on geometric properties of a specific water body, i.e., the coastal outline and bathymetric profile. Tidally generated water heights and currents can be the dominant feature in a coastal area or they may serve as background circulation that contributes in an influential manner to overall coastal dynamics. Tidal predictions are a necessary component of any description of the coastal environment for navigational purposes, coastal fisheries, and military operations, to name a few applications. The success of each of these endeavors rests upon accurate prediction of the tidal response of the coastal ocean and, consequently, on the formulation of an accurate numerical hydrodynamic model.

Justification for selection of the ADCIRC-2DDI finite element (FE) numerical model is based on accuracy, mesh flexibility, and computational efficiency. ADCIRC-2DDI (Luettich et al. 1992) implements the generalized wave-continuity equation (GWCE) and momentum balance equations for which accuracy is well documented with respect to the solution of various shallow-water problems (Foreman 1988; Lynch et al. 1988; Walters 1988; Werner and Lynch 1989; Walters and Werner 1989; Gray 1989; Lynch and Werner 1991; Luettich et al. 1992). In addition, the FE formulation of ADCIRC-2DDI leads to tremendous grid flexibility, allowing easy incorporation of coastline detail and nodal densities that range over 3 to 4 orders of magnitude. The wide variation in nodal density permits significant resolution of shoreline geometry, as well as high levels of refinement near shallow, coastal areas and in regions of rapid bathymetric change. Moreover, the discrete problem remains well within computational limits despite the large variation in nodal density.

Following a detailed presentation of the numerical hydrodynamic model, its development, equations, and numerical solution, validation of predicted tidal heights and currents in the North Sea/English Channel is undertaken within the context of the Tidal Flow Forum as outlined by Werner and Lynch (1988). Discussion of sensitivity studies examines the effects and behavior of nonlinear terms in the model equations, forms of the tidal forcing, and a variety of model parameters. Issues relating to mesh resolution are investigated within the context of tidal dynamics. A final statement summarizes major conclusions and observations that augment our understanding of tidal dynamics and increase our capabilities in applying the ADCIRC-2DDI hydrodynamic model to coastal tide prediction.

## 2.0 THE HYDRODYNAMIC MODEL

The purpose of a barotropic hydrodynamic model is to characterize the important flow features of surface waters driven by tides, wind, and atmospheric pressure gradients. The complexity of circulation patterns in coastal and continental shelf margin waters necessitates use of a numerical hydrodynamic model. Such models compute spatial and temporal distributions of velocity and sea surface elevation from which circulation patterns can be inferred. Success of the computed tidal response in resembling the actual coastal ocean depends in part on selection of an appropriate hydrodynamic model. An optimal model is one that captures tidal-induced dynamics, yet remains computationally feasible.

### 2.1 Criteria for Selection

The theoretical basis of a hydrodynamic model is found in the principles of mass and momentum conservation. For vertically well-mixed surface waters experiencing tidal and atmospheric forcing, the flow physics are described by the shallow-water equations, a depth-integrated form of the conservation laws (Le Mehaute 1976). The shallow-water equations have been used successfully by engineers and researchers for many years to predict tidal circulation (e.g., Reid and Whitaker 1981; Gray and Kinnmark 1983; LeProvost and Vincent 1986; Flather 1988; Foreman 1988; Baptista et al. 1989; Al-Rabeh et al. 1990; Westerink et al. 1989, 1992a, 1994a, 1995; Luettich and Westerink 1995).

Naturally, formulation of the hydrodynamic model and the solution strategy for the discrete problem must be accurate. Wavelength and phase propagation characteristics, mass conservation properties, and performance in idealized test cases and field applications are all used to evaluate model accuracy.

A second consideration in selection of a model is efficiency of the numerical solution algorithm. Meaningful boundary forcing can necessitate the use of large model domains that cover the continental shelf, coastal regions, and include portions of the deep ocean (Blain et al. 1994). Furthermore, the time frame for typical simulations ranges from hours to months. The feasibility of a model that utilizes large domains and extended simulation periods depends upon the efficiency of the numerical solution algorithm. Efficiency is achieved by minimizing the number of degrees of freedom and the number of operations per degree of freedom at each computational timestep.

Lastly, both efficiency and accuracy of the hydrodynamic model formulation are intertwined with the characteristics of the discrete mesh and its relation to the numerical solution algorithm. Grid flexibility allows minimization of the number of degrees of freedom, while simultaneously providing the localized resolution needed for accurate model predictions.

The selection criteria for any hydrodynamic model is summarized as follows: governing equations based on conservation principles, an efficient and accurate numerical solution algorithm, and a significant level of grid flexibility.

## 2.2 Current Numerical Modeling Approaches

The search for accurate and efficient solution algorithms for the shallow-water equations has led to a variety of equation formulations and the use of several numerical solution techniques. Two prevalent numerical discretization strategies utilize the finite difference and FE approaches. Finite difference methods discretize derivative operators contained in the model equations using point difference expressions (Lapidus and Pinder 1982), while FE techniques approximate the solution to the model equations through the use of interpolation functions (Celia and Gray 1992). A review of several FE solution techniques for the shallow-water equations is given by Lee and Froehlich (1986). Westerink and Gray (1991), in their recent review, note increasing similarities between finite difference- and FE-based models, especially with regard to the accurate propagation of short wavelengths, grid flexibility, and complex boundary representation. Further comparison and discussion of these methods is given by Blain and McManus (1998).

Early finite difference solutions of the shallow-water equations were quite accurate, owing in part to implementation of a staggered grid approach, which successfully avoided the introduction of artificial short waves (Westerink and Gray 1991). In contrast, early FE schemes were plagued by spurious oscillations or numerical noise due to the introduction of  $2 \cdot \Delta x$  wavelengths, a consequence of folded dispersion characteristics (Lynch 1983; Kolar et al. 1994b). Note that  $2 \cdot \Delta x$  wavelengths are the smallest wavelengths captured by a mesh having a minimum spacing  $\Delta x$ . Early FE algorithms included excessive damping mechanisms to counter the generation of spurious modes and, as a result, yielded inaccurate solutions (Gray 1982; Gray and Kinnmark 1983). It wasn't until Lynch and Gray (1979) introduced the wave-continuity equation (WCE) formulation for the shallow-water equations that the viability of FE approaches improved.

The WCE formulation simply involves a rearrangement of the shallow-water equations prior to spatial discretization. Solutions using the WCE successfully suppress short wavelengths without resorting to nonphysical dissipation. Understanding the origin and behavior of spurious oscillations within FE formulations (Walters and Carey 1983), together with extensive numerical testing of the WCE formulation (Kinnmark and Gray 1984, 1985; Luettich et al. 1992; Westerink et al. 1992b; Kolar et al. 1994 a,b) has resulted in very accurate WCE-based FE solutions (Lynch and Gray 1979; Foreman 1983).

In addition to accuracy, efficiency of a numerical algorithm must also be considered. Representation of complex circulation patterns by a hydrodynamic model often requires highly refined grids having very small nodal spacings. As a consequence, the stability criteria for various time-stepping schemes dictate use of a very small time interval for computations. The practicality of using small timesteps for long period simulations depends on the efficiency of the numerical solution algorithm. Implicit time-stepping schemes are generally more stable and allow larger timesteps, but result in time-dependent matrices that require reassembly and resolution at every timestep. This procedure is computationally intensive. Many finite difference models overcome this problem by implementing the alternating direction implicit (ADI) solution algorithm that reduces a two-dimensional (2D) problem to a sequence of one-dimensional (1D) problems, thus significantly reducing the computational effort (Leendertse 1987). The ADI approach, however, cannot be applied to unstructured grid algorithms such as FE solution strategies.

In contrast to an application of FEs to the primitive shallow-water equation, a WCE-based FE formulation leads to decoupled elevation and velocity solutions and sparse, symmetric matrices (Lynch and Gray 1979). Solutions for elevation are time independent due to a reformulation of the WCE by Kinnmark (1984) into a GWCE. Matrices resulting from an application of the FE method to the momentum equations remain time dependent, but this time dependence is overcome by lumping these matrices (that is, summing off-diagonal terms and adding the sum to the diagonal term), which causes only a slight degradation in accuracy. As a consequence, velocities are computed by solving a trivial tridiagonal system of equations (Lynch and Gray 1979).

One final consideration in selecting a numerical solution algorithm is grid flexibility. To date, the finite difference method is not readily amenable to providing high levels of refinement in localized areas. Restrictions on acceptable grid skewness and maximum cell-to-cell size ratios (i.e., Heath et al. 1990; Celia and Gray 1992) often result in finite difference grids that are over-refined, causing unnecessary computational burden. To represent detailed coastline geometry, coordinate transformation techniques were developed in the context of finite difference schemes, but these methods still do not allow for increased resolution in localized areas.

In contrast, the advantage of the FE approach lies in its tremendous flexibility of nodal placement to represent the complexity of the shoreline and provide varying degrees of resolution throughout the model domain as warranted. In particular, FE schemes based on triangular elements result in optimal flexibility for achieving local refinement (e.g., Luettich et al. 1992; Westerink et al. 1995; Blain et al. 1998). With the ever increasing size and complexity of shallow-water problems, the degree of mesh flexibility inherent in the discretization strategy directly affects the efficiency and accuracy of the hydrodynamic model.

### 2.3 The ADCIRC-2DDI Hydrodynamic Model

A careful evaluation of the accuracy, efficiency, and grid flexibility characteristics of current numerical solution algorithms for the shallow-water equations has led to selection of a GWCE FE-based formulation of the shallow-water equations. One such hydrodynamic model is ADCIRC-2DDI, the depth-integrated portion of a system of 2D and three-dimensional (3D) codes named ADCIRC (ADvanced CIRCulation Model for Shelves, Coasts, and Estuaries), developed by Luettich et al. (1992) and Westerink et al. (1992b).

The efficiency and accuracy of ADCIRC-2DDI are well understood due to extensive numerical testing and analysis of the model code. The algorithms that comprise ADCIRC-2DDI effectively minimize the required number of degrees of freedom for a desired level of accuracy, show good stability characteristics, generate no spurious artificial modes, utilize minimum inherent artificial numerical damping, efficiently separate the partial differential equations into systems of algebraic equations with time-independent matrices, and are capable of running months to years of simulation while providing detailed computations of the circulation patterns within a water body (Luettich et al. 1992). Other studies that address specific characteristics of the ADCIRC-2DDI model formulation are the investigation of mass conservation properties of the GWCE formulation by Kolar et al. (1994b) and the accuracy of the boundary condition formulation within ADCIRC-2DDI (Westerink et al. 1994b).

The ADCIRC-2DDI hydrodynamic model produces computations that are in agreement with two established benchmark problems, the quarter annular test case (Gray 1982) and the North Sea/English Channel system (Werner and Lynch 1988). The ADCIRC-2DDI model has also been applied

to a number of field studies with excellent results (Westerink et al. 1989, 1992 a,b, 1994a; Kolar 1994 a,b). Detailed documentation (Luettich et al. 1992), as well as an instructive commentary regarding appropriate setup of the ADCIRC-2DDI model (Westerink et al. 1992b), facilitates its application in the coastal ocean.

### 2.3.1 Governing Equations

The generalized wave-continuity equation formulation in ADCIRC-2DDI is based on the well-known, shallow-water equations (Le Mehaute 1976; Kinnmark 1984). The primitive form of the shallow-water equations is derived by averaging conservation laws of mass and momentum over the timescale of turbulent fluctuations and ocean depth. Turbulent fluctuations at the microscale present in all hydrodynamic flows are characterized by spatial and temporal variations in velocity and pressure fields and are a mechanism for momentum transfer. Time averaging the conservation laws generates macroscale quantities representing microscale fluctuations that must be parameterized. The scale for time averaging is selected to be long enough to span a statistically significant sample of turbulent fluctuations, and yet short enough so that macroscopic variations of the averaged quantity are not included (Gray et al. 1993). Within the shallow-water equations, turbulent fluctuations are characterized by momentum diffusion terms.

Depth averaging the conservation laws reduces a 3D problem to 2D, leaving as unknowns the surface water elevation  $\zeta$  and the depth-averaged lateral velocities  $U$  and  $V$ . For flows having small, vertical velocity gradients (e.g., well-mixed systems) or environments where lateral flows are quite large in comparison to vertical velocities (e.g., nearly horizontal flow), application of the shallow-water equations is accepted practice.

Derivation of the shallow-water equations from the time- and depth-averaged conservation laws involves the Boussinesq approximation in addition to hydrostatic and incompressibility assumptions. In practice, incompressibility of a fluid implies that density variations seen while moving with the fluid are negligible (i.e.,  $\frac{D\rho}{Dt} = 0$ ). Furthermore, the Boussinesq approximation specifies density as a constant value,  $\rho = \rho_o$ , except when gradients of density are considered. In flows appropriate for 2D, depth-averaged equations, vertical acceleration is assumed negligible. Consequently, the momentum equation over the vertical reduces to a balance between pressure and gravitational forces. This is commonly referred to as the hydrostatic assumption. Other simplifications implicit within the shallow-water equations include neglecting changes in the position of the ocean floor with respect to time and excluding mass exchanges with the environment (i.e., evaporation, precipitation, overland flow, and groundwater interactions).

For a Cartesian coordinate system, the conservative form of the shallow-water equations are written:

$$\frac{\partial \zeta}{\partial t} + \frac{\partial UH}{\partial x} + \frac{\partial VH}{\partial y} = 0 \quad (2.1)$$

$$\frac{\partial UH}{\partial t} + \frac{\partial UUH}{\partial x} + \frac{\partial UVH}{\partial y} - f VH = -H \frac{\partial}{\partial x} \left[ \frac{p_s}{\rho_o} + g(\zeta - \alpha\eta) \right] + M_x + D_x + B_x + \frac{\tau_{sx}}{\rho_o} - \frac{\tau_{bx}}{\rho_o} \quad (2.2)$$

$$\frac{\partial VH}{\partial t} + \frac{\partial VUH}{\partial x} + \frac{\partial VVH}{\partial y} + f UH = -H \frac{\partial}{\partial y} \left[ \frac{p_s}{\rho_o} + g(\zeta - \alpha\eta) \right] + M_y + D_y + B_y + \frac{\tau_{sy}}{\rho_o} - \frac{\tau_{by}}{\rho_o}, \quad (2.3)$$

where  $t$  represents time,  $x, y$  are the Cartesian coordinate directions,  $\zeta$  is the free surface elevation relative to the geoid,  $U, V$  are the depth-averaged horizontal velocities,  $H = \zeta + h$  is the total water column depth,  $h$  is the bathymetric depth relative to the geoid,  $f$  is the Coriolis parameter,  $p_s$  is the atmospheric pressure at the free surface,  $g$  is the acceleration due to gravity,  $\alpha$  is the Earth elasticity factor,  $\eta$  is the Newtonian equilibrium tide potential,  $\rho_o$  is the reference density of water,  $M_x, M_y$  represents the depth-integrated horizontal momentum diffusion,  $D_x, D_y$  are the depth-integrated horizontal momentum dispersion terms,  $B_x, B_y$  are the depth-integrated baroclinic forcings, and  $\tau_{sx}, \tau_{sy}$  are the applied free surface stresses. Further justification regarding the appropriateness of these equations in modeling tidal and atmospheric forces flows is provided by Blumberg and Mellor (1987), Westerink et al. (1989), and Luettich et al. (1992).

In operator notation, a relationship between the conservative and nonconservative momentum equations is given (Kolar 1992):

$$M^{NC} = \frac{1}{H} (M^C - v C), \quad (2.4)$$

where  $M^{NC}$  are the nonconservative momentum equations,  $M^C$  represents the conservative momentum Eqs. (2.2) and (2.3),  $v$  is the horizontal velocity vector, and  $C$  is the primitive continuity Eq. (2.1). Substituting Eqs. (2.1)–(2.3) into Eq. (2.4) leads to a reformulation of the momentum equations into primitive, nonconservative form:

$$\frac{\partial U}{\partial t} + U \frac{\partial U}{\partial x} + V \frac{\partial U}{\partial y} - f V = - \frac{\partial}{\partial x} \left[ \frac{p_s}{\rho_o} + g(\zeta - \alpha \eta) \right] + \frac{1}{H} \left[ M_x + D_x + B_x + \frac{\tau_{sx}}{\rho_o} - \frac{\tau_{bx}}{\rho_o} \right] \quad (2.5)$$

$$\frac{\partial V}{\partial t} + U \frac{\partial V}{\partial x} + V \frac{\partial V}{\partial y} + f U = - \frac{\partial}{\partial y} \left[ \frac{p_s}{\rho_o} + g(\zeta - \alpha \eta) \right] + \frac{1}{H} \left[ M_y + D_y + B_y + \frac{\tau_{sy}}{\rho_o} - \frac{\tau_{by}}{\rho_o} \right]. \quad (2.6)$$

A rigorous derivation of Eqs. (2.1)–(2.6) is presented by Kolar (1992) and will not be repeated here.

Implementation of a standard quadratic parameterization for bottom stress and the neglect of baroclinic and lateral diffusion/dispersion terms leads to a modified form of the primitive, nonconservative, shallow-water equations:

$$\frac{\partial \zeta}{\partial t} + \frac{\partial U H}{\partial x} + \frac{\partial V H}{\partial y} = 0 \quad (2.7)$$

$$\frac{\partial U}{\partial t} + U \frac{\partial U}{\partial x} + V \frac{\partial U}{\partial y} - f V = - \frac{\partial}{\partial x} \left[ \frac{p_s}{\rho_o} + g(\zeta - \alpha \eta) \right] + \frac{\tau_{sx}}{\rho_o H} - \tau_* U \quad (2.8)$$

$$\frac{\partial V}{\partial t} + U \frac{\partial V}{\partial x} + V \frac{\partial V}{\partial y} + f U = - \frac{\partial}{\partial y} \left[ \frac{p_s}{\rho_o} + g(\zeta - \alpha \eta) \right] + \frac{\tau_{sy}}{\rho_o H} - \tau_* V, \quad (2.9)$$

with  $\tau_*$  given by the expression  $C_f (U^2 + V^2)^{1/2}/H$ , for  $C_f$  equal to the bottom friction coefficient.

Recall that one objective of the ADCIRC-2DDI hydrodynamic model is to be able to consider very large domain problems. The use of large domains coupled with a recognition that tidal forcing is a global phenomena necessitates the inclusion of effects caused by curvature of the Earth's surface. Thus, shallow-water Eqs. (2.7)–(2.9) are recast into spherical coordinates (Flather 1988; Kolar et al. 1994a):

$$\frac{\partial \zeta}{\partial t} + \frac{1}{R \cos \phi} \left[ \frac{\partial u_\lambda H}{\partial \lambda} + \frac{\partial (v_\phi H \cos \phi)}{\partial \phi} \right] = 0 \quad (2.10)$$

$$\frac{\partial u_\lambda}{\partial t} + \frac{u_\lambda}{R \cos \phi} \frac{\partial u_\lambda}{\partial \lambda} + \frac{v_\phi}{R} \frac{\partial u_\lambda}{\partial \phi} - \left[ \frac{\tan \phi u_\lambda}{R} + f \right] v_\phi = - \frac{1}{R \cos \phi} \frac{\partial}{\partial \lambda} \left[ \frac{p_s}{\rho_o} + g(\zeta - \eta) \right] + \frac{\tau_{s\lambda}}{\rho_o H} - \tau_* u_\lambda \quad (2.11)$$

$$\frac{\partial v_\phi}{\partial t} + \frac{u_\lambda}{R \cos \phi} \frac{\partial v_\phi}{\partial \lambda} + \frac{v_\phi}{R} \frac{\partial v_\phi}{\partial \phi} + \left[ \frac{\tan \phi u_\lambda}{R} + f \right] u_\lambda = - \frac{1}{R} \frac{\partial}{\partial \phi} \left[ \frac{p_s}{\rho_o} + g(\zeta - \eta) \right] + \frac{\tau_{s\phi}}{\rho_o H} - \tau_* v_\phi, \quad (2.12)$$

where  $\lambda$ ,  $\phi$  are degrees longitude (east of Greenwich positive) and degrees latitude (north of the equator positive),  $u_\lambda$ ,  $v_\phi$  are depth-averaged velocities in spherical coordinates,  $R$  is the radius of the Earth,  $f$  is given by  $2\Omega \sin \phi$ ,  $\Omega$  is the angular speed of the Earth, and  $\tau_{s\lambda}$ ,  $\tau_{s\phi}$  are the applied free surface stresses.

A practical expression for the Newtonian equilibrium tide potential is given by Reid (1990) as:

$$\eta(\lambda, \phi, t) = \sum_{n,j} C_{jn} f_{jn}(t_0) L_j(\phi) \cos [2\pi(t - t_0)/T_{jn} + j\lambda + \nu_{jn}(t_0)], \quad (2.13)$$

where  $t$  is time relative to the reference time,  $t_0$ ,  $C_{jn}$  is a constant characterizing the amplitude of tidal constituent  $n$  of species  $j$ ,  $f_{jn}$  is a time-dependent nodal factor,  $\nu_{jn}$  is the time-dependent astronomical argument,  $j = 0, 1, 2$  are the tidal species ( $j = 0$  declinational;  $j = 1$  diurnal,  $j = 2$  semidiurnal),  $L_0 = 3\sin^2 \phi - 1$ ,  $L_1 = \sin(2\phi)$ ,  $L_2 = \cos^2(\phi)$ , and  $T_{jn}$  is the period of constituent  $n$  for species  $j$ . Values for  $C_{jn}$  are presented by Reid (1990) and the Earth elasticity factor is often taken as 0.69 for all tidal constituents (Schwiderski 1980; Hendershott 1981), although its value has been shown to be slightly constituent-dependent, ranging between 0.693 and 0.736 (Wahr 1981; Woodworth 1990).

The Earth's curvature must be accounted for, not only in the governing equations, but also in the FE discretization (Kolar et al. 1994a). In the FE method, the solution to the governing equations is approximated using interpolating functions. These interpolating functions are defined over elements and these elements are most often cast within the framework of a Cartesian coordinate system. To conveniently implement the FE method, governing equations in spherical coordinates are projected onto a planar surface using cartographic projection techniques. Mapping spherical Eqs. (2.10)–(2.12) to a rectilinear coordinate system is accomplished using a Carte Parallelogrammatique Projection (CP) (Pearson 1990):

$$x' = R(\lambda - \lambda_o) \cos \phi \quad (2.14)$$

$$y' = R\phi, \quad (2.15)$$

where  $(\lambda_0, \phi_0)$  is the center point of the projection. An application of the CP projection to Eqs. (2.10)–(2.12) yields shallow-water equations in primitive, nonconservative form expressed in the CP coordinate system:

$$\frac{\partial \zeta}{\partial t} + \frac{\cos \phi_0}{\cos \phi} \frac{\partial (UH)}{\partial x'} + \frac{1}{\cos \phi} \frac{\partial (VH \cos \phi)}{\partial y'} = 0 \quad (2.16)$$

$$\frac{\partial U}{\partial t} + \frac{\cos \phi_0}{\cos \phi} U \frac{\partial U}{\partial x'} + V \frac{\partial U}{\partial y'} - \left[ \frac{\tan \phi}{R} U + f \right] V = - \frac{\cos \phi_0}{\cos \phi} \frac{\partial}{\partial x'} \left[ \frac{P_s}{\rho_0} + g(\zeta - \eta) \right] + \frac{\tau_{s\lambda}}{\rho_0 H} - \tau_* U \quad (2.17)$$

$$\frac{\partial V}{\partial t} + \frac{\cos \phi_0}{\cos \phi} U \frac{\partial V}{\partial x'} + V \frac{\partial V}{\partial y'} + \left[ \frac{\tan \phi}{R} U + f \right] U = - \frac{\partial}{\partial y'} \left[ \frac{P_s}{\rho_0} + g(\zeta - \eta) \right] + \frac{\tau_{s\phi}}{\rho_0 H} - \tau_* V. \quad (2.18)$$

As discussed in Sec. 2.2, utilizing the FE method to resolve spatial dependencies in the primitive shallow-water equations leads to inaccurate solutions with severe artificial, near  $2 \cdot \Delta x$  modes (Gray 1982; Lynch 1983; Westerink et al. 1989). Reformulation of the primitive equations into a GWCE gives highly accurate, noise-free, FE-based solutions to the shallow-water equations (Lynch and Gray 1979; Kinnmark 1984). The high accuracy of GWCE-based FE solutions is a result of their excellent numerical amplitude and phase propagation characteristics. In fact, Fourier analysis indicates that for constant-depth water using linear interpolation, a linear tidal wave resolved with 25 nodes per wavelength is more than adequately represented over the range of Courant numbers,  $C = \sqrt{gh} \Delta t / \Delta x$ , less than or equal to one (Luettich et al. 1992). Furthermore, the monotonic dispersion behavior of GWCE-based FE solutions avoids generating artificial, near  $2 \cdot \Delta x$  modes that have plagued the primitive FE-based solutions on the interior and at the boundary (Platzman 1981; Foreman 1983; Westerink et al. 1994b). Note that the monotonic dispersion behavior of GWCE-based FE solutions is very similar to that associated with staggered finite difference solutions to the primitive shallow-water equations (Westerink and Gray 1991). GWCE-based FE solutions to the shallow-water equations allow extremely flexible spatial discretizations that effectively minimize the discrete size of any problem (LeProvost and Vincent 1986; Foreman 1988; Vincent and LeProvost 1988; Westerink et al. 1994a, 1995; Luettich and Westerink 1995).

Derivation of the GWCE is presented concisely using the operator notation invoked by Kinnmark (1984) and Kolar (1992):

$$GWCE = \frac{dC}{dt} + \tau_o C - \nabla \cdot \mathbf{M}^c, \quad (2.19)$$

where  $GWCE$  is the generalized wave-continuity equation and  $\tau_o$  is a nonphysical constant in time and space that controls the balance between primitive and wave equation formulations (Lynch and Gray 1979; Kinnmark 1984; Luettich et al. 1992; Kolar et al. 1994b). Substituting continuity Eq. (2.16) and the conservative form of momentum Eqs. (2.17) and (2.18) into Eq. (2.19), the GWCE in the CP coordinate system is:

$$\frac{\partial^2 \zeta}{\partial t^2} + \tau_0 \frac{\partial \zeta}{\partial t} + \frac{\cos \phi_0}{\cos \phi} \frac{\partial}{\partial x'} \left[ U \frac{\partial \zeta}{\partial t} - \frac{\cos \phi_0}{\cos \phi} UH \frac{\partial U}{\partial x'} - VH \frac{\partial U}{\partial y'} + \left[ \frac{\tan \phi}{R} U + f \right] VH \right]$$

$$\begin{aligned}
& -H \frac{\cos \phi_0}{\cos \phi} \frac{\partial}{\partial x'} \left( \frac{P_s}{\rho_0} + g(\zeta - \alpha \eta) \right) - (\tau_* - \tau_0) UH + \frac{\tau_{s\lambda}}{\rho_0} \Big] \\
& + \frac{\partial}{\partial y'} \left[ V \frac{\partial \zeta}{\partial t} - \frac{\cos \phi_0}{\cos \phi} UH \frac{\partial V}{\partial x'} - VH \frac{\partial V}{\partial y'} - \left[ \frac{\tan \phi}{R} U - f \right] UH \right. \\
& \left. - H \frac{\partial}{\partial y'} \left( \frac{P_s}{\rho_0} + g(\zeta - \alpha \eta) \right) - (\tau_* - \tau_0) VH + \frac{\tau_{s\phi}}{\rho_0} \right] \\
& - \frac{\partial}{\partial t} \left[ \frac{\tan \phi}{R} VH \right] - \tau_0 \left[ \frac{\tan \phi}{R} VH \right] = 0 . \tag{2.20}
\end{aligned}$$

Advection terms in the GWCE, written in nonconservative form, improve global and local mass conservation (Kolar et al. 1994b), as well as numerical stability, especially for advection dominant flows (Westerink et al. 1992b). The ADCIRC-2DDI hydrodynamic model solves the GWCE, Eq. (2.20), in conjunction with the primitive momentum equations in nonconservative form, Eqs. (2.17) and (2.18).

### 2.3.2 Numerical Solution

Numerical discretization of GWCE Eq. (2.20) and momentum Eqs. (2.17) and (2.18) is implemented in three stages. First, the symmetrical weak weighted residual (SWWR) statements for Eqs. (2.17), (2.18), and (2.20) are developed. This procedure is based on a standard Galerkin FE formulation (Becker et al. 1981; Celia and Gray 1992). One consequence of the SWWR is that the order of the derivatives in the governing equations is reduced, leading to a requirement of only  $C_0$  functional continuity (i.e., only the interpolating functions themselves and not their derivatives need be continuous between discrete points). Next, the stable and accurate time discretization strategies of Kinnmark (1984) and Werner and Lynch (1989) are implemented. A variably weighted three-time-level implicit scheme is applied to linear terms in the GWCE. The nonlinear Coriolis, atmospheric pressure, and tidal potential terms are all treated explicitly. Alternatively, advective terms within the GWCE are evaluated at two known time levels. This time discretization results in a system of linear algebraic equations associated with the GWCE, which is solved for unknown elevations. In the momentum equations, a Crank-Nicolson two-time-level implicit scheme is applied to all terms except the bottom friction and advective terms, which are treated explicitly.

The final step in the numerical discretization scheme is approximation of the spatial domain using the FE method. Variables are expanded using a  $C_0$  interpolation basis over three-node, linear triangular elements. Elemental equations are summed over the global domain and inter-element  $C_0$  functional continuity is enforced. Details of the FE implementation on a term-by-term basis is presented by Luettich et al. (1992) and Westerink et al. (1992b).

The fully discretized model equations are written in matrix notation (Luettich et al. 1992):

$$M^{GWCE \zeta k+1} = P^{GWCE} \tag{2.21}$$

$$\mathbf{M}^{\lambda\lambda ME} \mathbf{U}^{k+1} + \mathbf{M}^{\lambda\phi ME} \mathbf{V}^{k+1} + \mathbf{P}^{\lambda ME} \quad (2.22)$$

$$\mathbf{M}^{\phi\lambda ME} \mathbf{U}^{k+1} + \mathbf{M}^{\phi\phi ME} \mathbf{V}^{k+1} + \mathbf{P}^{\phi ME}, \quad (2.23)$$

where  $\mathbf{M}^{GWCE}$  is the banded, time-independent mass matrix in the GWCE equation,  $\zeta^{k+1}$  is the vector of unknown surface elevations at time level  $k+1$ ,  $\mathbf{P}^{GWCE}$  is the load vector of known forcings in the GWCE equation,  $\mathbf{M}^{\lambda\lambda ME}$ ,  $\mathbf{M}^{\lambda\phi ME}$ ,  $\mathbf{M}^{\phi\lambda ME}$ , and  $\mathbf{M}^{\phi\phi ME}$  are the time-dependent, lumped mass matrices in the  $\lambda, \phi$  directions,  $\mathbf{U}^{k+1}$ ,  $\mathbf{V}^{k+1}$  are the vectors of unknown velocity components at the  $k+1$  time level, and  $\mathbf{P}^{\lambda ME}$ ,  $\mathbf{P}^{\phi ME}$  are the load vectors of known forcings for the momentum equations.

Elevation boundary conditions are enforced within the load vector  $\mathbf{P}^{GWCE}$  of the GWCE Eq. (2.21) and zero normal velocity boundary conditions are enforced in the momentum Eqs. (2.22) and (2.23). Westerink et al. (1994b) have shown that solutions to the GWCE equation are insensitive to this standard boundary condition formulation.

The decoupled discrete GWCE and momentum Eqs. (2.21)–(2.23) lead to a sequential solution procedure. GWCE Eq. (2.21) is solved at each timestep for the surface water elevations  $\zeta^{k+1}$ . The GWCE mass matrix  $\mathbf{M}^{GWCE}$  is time-independent, so it is assembled and decomposed only once. The banded structure of this matrix is not utilized by the iterative preconditioned conjugate gradient matrix solver used for computations performed in this work (Press et al. 1986; Kincaid and Cheney 1991). A preconditioned conjugate gradient solver is implemented because of its efficiency at minimizing memory requirements within ADCIRC-2DDI for larger problems. The load vector  $\mathbf{P}^{GWCE}$  is updated at each timestep with newly computed surface water elevations and velocities from the previous timestep.

After solving the GWCE for surface water elevations, these computed elevations are substituted into momentum Eqs. (2.22) and (2.23) prior to solution for the velocity components and  $\mathbf{U}^{k+1}$  and  $\mathbf{V}^{k+1}$ . The time-dependent mass matrices in the momentum equations  $\mathbf{M}^{\lambda\lambda ME}$ ,  $\mathbf{M}^{\lambda\phi ME}$ ,  $\mathbf{M}^{\phi\lambda ME}$ , and  $\mathbf{M}^{\phi\phi ME}$  are lumped to yield diagonal matrices that require trivial solution. The lumping procedure applied here does not introduce significant errors as shown by Lynch and Gray (1979).

The numerical solution algorithm just described for the ADCIRC-2DDI model is implemented in fully vectorized form. A consequence of this solution procedure is a highly efficient code in terms of central processing unit (CPU) requirements per node. This efficiency is largely due to the fact that GWCE-based FE solutions to the shallow-water equations allow for extremely flexible spatial discretizations that result in minimization of the discrete size of any problem (LeProvost and Vincent 1986; Foreman 1988; Vincent and LeProvost 1988; Westerink et al. 1992 a,b, 1994a, 1995).

### 2.3.3 Summary

Numerical formulation of the hydrodynamic model is critical to achieving successful predictions of tidal circulation on the continental shelf. The depth-averaged shallow-water equations are an appropriate theoretical framework for the barotropic hydrodynamic model with additional requirements of accuracy, efficiency, and grid flexibility imposed on the numerical solution technique. In considering available numerical solution techniques for the shallow-water equations, a GWCE-based FE approach is thought to be an optimal solution strategy.

The hydrodynamic model, ADCIRC-2DDI, solves the GWCE-based FE equations and has demonstrated the desired characteristics of accuracy, efficiency, and a high degree of grid flexibility in numerous idealized tests, analyses, and field applications. For all tidal simulations presented in this work, the ADCIRC-2DDI hydrodynamic model is utilized. Modularity of the model allows the user to render various terms and/or forcing mechanisms within the model active or inactive. This modularity is found to be a necessary asset both for the study described herein and for future diagnostic examinations of coastal tidal dynamics.

### 3.0 THE TIDAL FLOW FORUM BENCHMARK CASE

#### 3.1 Description

Tidal Flow Forums 1 (TFF) (Lisbon, Portugal 1986) and 2 (Cambridge, MA 1988) provide benchmark test cases for the quantitative skill assessment of coastal tidal hydrodynamic models. The southern North Sea/English Channel is chosen by TFF organizers as an appropriate study area for several reasons: (1) the hydrodynamics of the region have been studied extensively, (2) a fairly complete set of model input data is readily available, and (3) field observations of both elevation and currents are available. Characteristic nonlinearity and spatial variability of tides in the region provide a good test for any tidal hydrodynamic model. Furthermore, the small size of the domain makes a tractable problem for a variety of numerical model formulations and computer resources, facilitating model-model comparisons. Essential information for model setup and validation data provided by Verboom and LeProvost (1986) include bathymetry, computational meshes, domain boundary tidal forcing, sea surface height, and current meter field data. The TFF standardizes a single tide model application for the purpose of validation and inter-comparison of numerical tidal models.

In the spirit of the TFF, model-to-model and model-to-data comparisons using both finite difference (Ozer and Jamart 1988; Jamart and Ozer 1989; Yu et al. 1989; Praagman et al. 1989 a,b) and FE (Werner and Lynch 1987; Gray et al. 1987; Walters 1987; Lynch and Werner 1988; Werner and Lynch 1989; Gray 1989; Baptista et al. 1989; Walters and Werner 1989; Werner 1995) models were conducted. The TFF study area has been modeled previously using ADCIRC-2DDI by Luettich et al. (1992). For this application of ADCIRC-2DDI in the southern North Sea/English Channel, Luettich et al. (1992) publish only a cursory comparison to TFF data from a limited number of model simulations. The present study is a considerable extension of that initial validation effort. The model experiments presented herein are intended to provide greater insight into simulating tidal physics with the ADCIRC-2DDI hydrodynamic model.

##### 3.1.1 Model Domain

The model domain, shown in Fig. 1, extends from the Dutch and English coasts in the southern North Sea to the French and English coasts at the western end of the English Channel. The original bathymetric data provided by Verboom and LeProvost (1986) has since been revised to resolve inconsistencies in the data (Werner and Lynch 1988). The FE grid, shown in Fig. 2, consists of 911 nodes and 1613 elements. Nodal spacings for this mesh (labeled G9 indicating a maximum resolution of 9 km) range between 9–15 km. Islands are not represented in this bathymetric grid; one notable omission is the Isle of Wight near Christchurch.

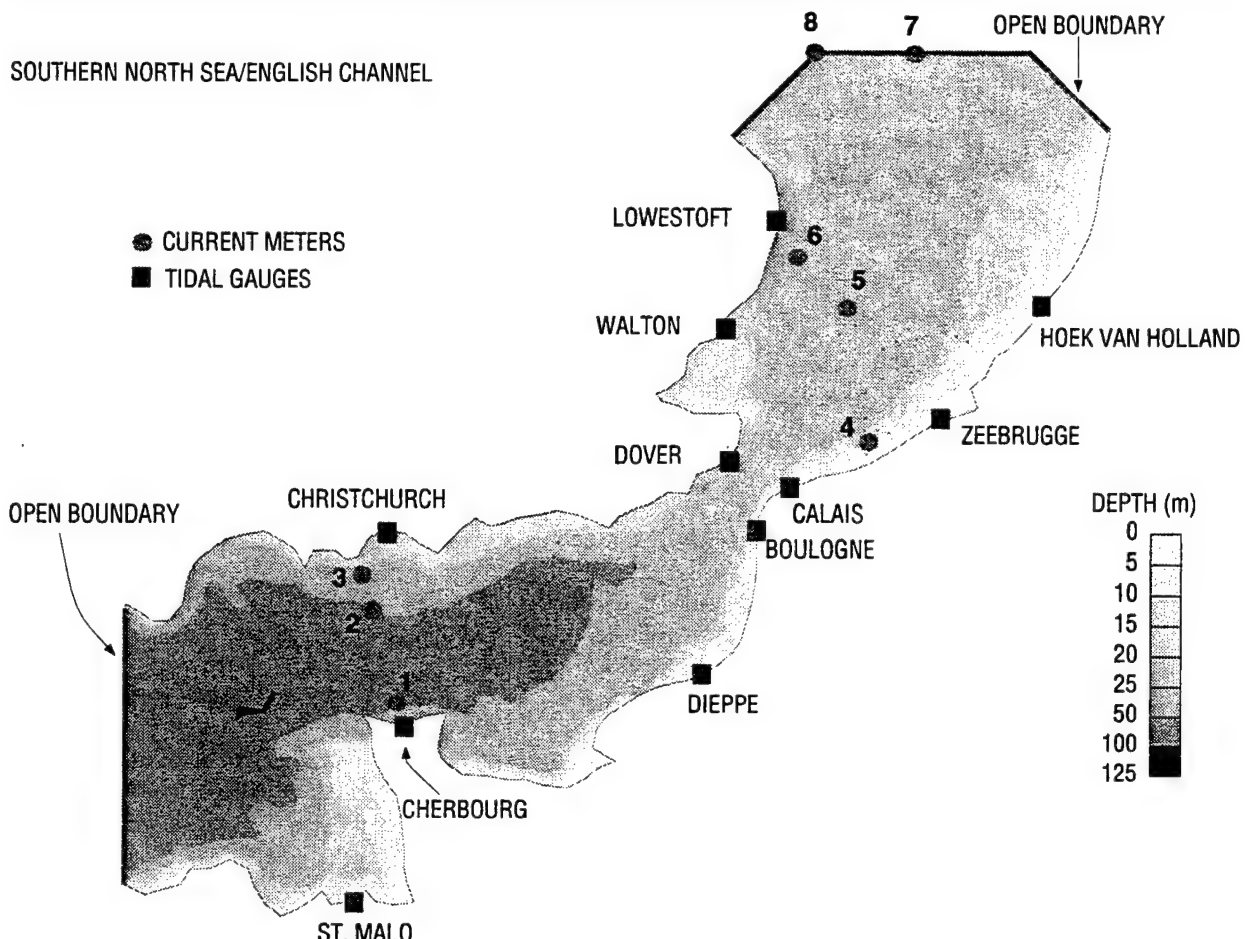


Fig. 1 — Southern North Sea/English Channel bathymetry

### 3.1.2 Open Boundary Forcing

Tidal elevation data in the form of tidal phases and amplitudes are provided at 23 locations on two open-ocean boundaries (identified in Fig. 1) for 11 constituents. The 11 tidal constituents include six primary components—two diurnal ( $O_1, K_1$ ), four semidiurnal ( $M_2, S_2, N_2, K_2$ ), and five nonlinear constituents ( $M_4, MS_4, MN_4, M_6, 2MS_6$ ). These 11 components will be referred to as "TFF constituents." This set of data is derived from the harmonic decomposition of measured elevations and are supplemented by the physical model study of d'Hieres and LeProvost (1979). The TFF constituent data are linearly interpolated onto boundary nodes of the FE mesh and constitute the sole means of forcing in this study unless otherwise indicated.

### 3.1.3 Bottom Friction Parameterization

For purposes of standardization, TFF organizers suggest a value for the Chezy bottom friction coefficient equal to  $65 \text{ m}^{0.5}/\text{s}$  (Verboom and LeProvost 1986). For a quadratic bottom friction representation, the Chezy coefficient translates to a value of  $C_f$  equal to  $2.322 \times 10^{-3}$ . This is the frictional coefficient used in ADCIRC-2DDI for those simulations that utilize a nonlinear representation of bottom friction.

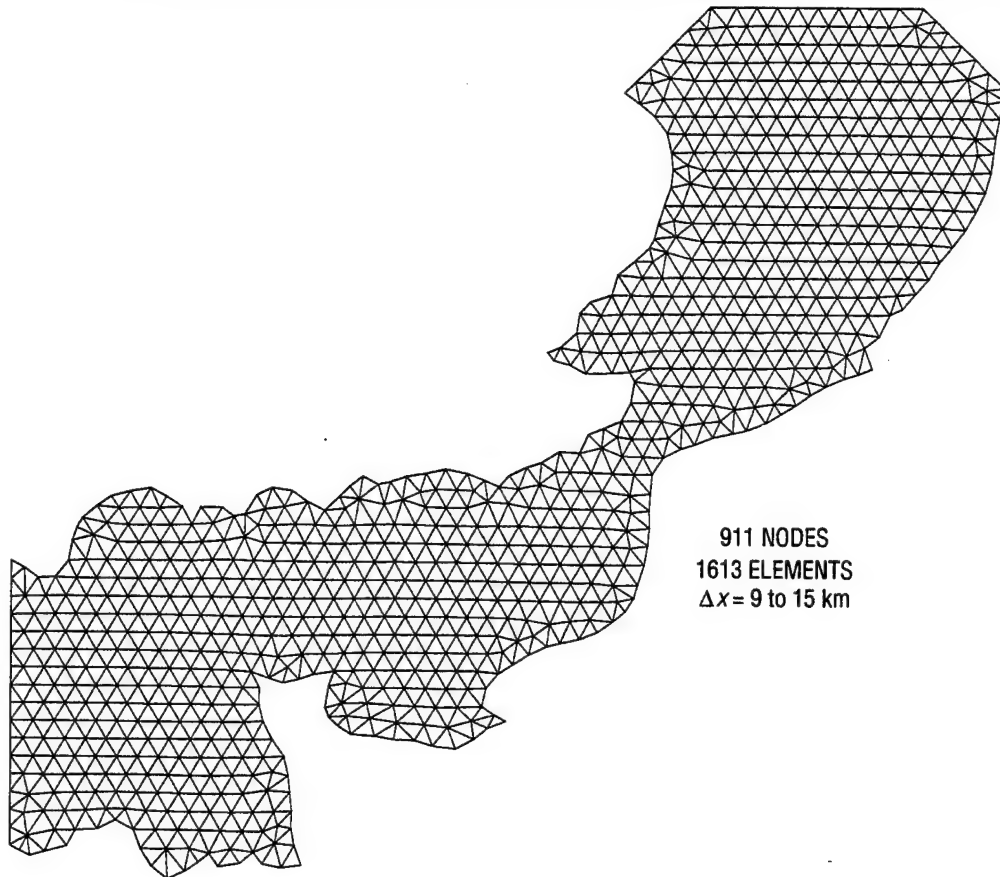


Fig. 2 — Revised finite element grid (Werner and Lynch 1988)

### 3.2 Field Observations

Amplitudes and phases for 11 tidal constituents constitute the tidal elevation data provided at 11 coastal locations shown in Fig. 1. These same TFF tidal constituents are used for boundary forcing and are thought to be of high quality since they are derived from long-term observations. However, as will be discussed in Sec. 5.1.2, these 11 tidal constituents do not provide a complete representation of the true tidal signal; other constituents are shown to make significant contributions in most areas of the domain. The field data available to the TFF organizers was not adequate to allow inclusion of these other important tidal constituents in the harmonic analyses. As such, the time series of elevation at each elevation gauge location is constructed from available tidal constituent information using the well-known harmonic relation for tides (Schureman 1958):

$$h = \sum_{i=1}^n f_i A_i \cos (\omega_i t - G_i + E_i). \quad (3.1)$$

Here,  $h$  is the sea surface elevation,  $n$  is the number of tidal constituents included in the time series,  $f$  is the constituent nodal factor,  $A$  is the constituent amplitude at that location,  $\omega$  is the constituent frequency,  $t$  is time,  $G$  is the constituent phase at that location, and  $E$  is the constituent equilibrium argument phase correction. Henceforth, time series reconstructed from the data are referred to as the observed elevation time series.

At eight offshore locations also shown in Fig. 1, velocity data taken from JONSDAP'76 (Ramster 1977) are based on direct measurement at a single location in the water column. From comparisons of the velocity data to ADCIRC model solutions, as well as from previous TFF discussions, overall speed observations are of questionable value. Further discussion pertaining to the velocity data is found in Sec. 5.2.

## 4.0 MODEL VALIDATION EXPERIMENTS

### 4.1 Description

In general, model experiments performed for this study are classified according to two broad categories based on length of the simulation. In keeping with the TFF benchmark case, a preliminary simulation of 3 d from 15–17 Mar 1976 is conducted. The first 2 d serve as a ramp-up period with analysis during the last 24 h. In addition, 45-d experiments using a 30-d spin-up period allow time for full dissipation of the free Helmholtz modes (Westerink et al. 1994a). The 45-d experiments include a 15-d period at the beginning of the simulation during which ADCIRC's hyperbolic tangent ramp function is applied to the model forcing (Luettich et al. 1992). Application of the hyperbolic tangent function results in zero forcing at the initiation of the experiment ( $t = 0$ ) and full-strength forcing at the end of the 15-d ramp-up period ( $t = 15$  d). Some minor differences are observed between the 45-d and 3-d experiments, so a 45-d duration is used for all short-term model experiments presented. The model reference time, used to compute the tidal nodal factors and equilibrium arguments, is defined 42 d into the short duration simulations; the date corresponding to this reference time is 15 Mar 1976. Model solutions from these short simulations are compared to observed time series of elevation and velocity.

Harmonic decomposition based on the least squares analysis method (e.g., van Ette and Schoemaker 1967; Foreman 1977) is implemented to decompose the model-computed time series into tidal constituent frequencies. Harmonic analyses of model solutions for short (45-d) simulations are unsuccessful, largely because of the inability of the method to distinguish the  $K_2$  and  $S_2$  frequencies using an abbreviated time signal. In fact, Godin (1972) recommends a time series length greater than 183 d to accurately extract the  $K_2$  and  $S_2$  tidal constituents. Therefore, a set of long-term simulations of 205 d in length was designed. These model experiments have 15 d for an initial ramp-up period and the remaining 190 d of the simulation are used in the harmonic analyses for 56 primary, compound, and overtide constituents. The harmonically decomposed time series of elevations are then utilized in model-to-model and model-to-data comparisons for individual tidal constituents or groups of tidal constituents.

### 4.2 Quantitative Analyses

#### 4.2.1 Error Measures

In analyzing model performance, two error measures are used for the time series comparisons: the root-mean-square (RMS) error,  $e_{rms}$ , and a proportional error  $\varepsilon^2$ . The RMS error is expressed:

$$e_{rms} = \sqrt{\frac{\sum_{j=1}^n (x_{mod} - x_{obs})^2}{n}} \quad (4.1)$$

and the proportional error is computed

$$\epsilon^2 = \frac{\sum_{j=1}^n (x_{mod} - x_{obs})^2}{\sum_{j=1}^n x_{obs}^2}. \quad (4.2)$$

Here,  $x_{mod}$  and  $x_{obs}$  are the modeled and observed elevation, current speed, or direction, respectively, and  $n$  is the number of observation stations. Computations of these two errors are based on comparisons between model-computed elevation, speed, direction, and observations of the same fields over the last 3 d of the model simulation, 15–17 Mar 1976. These error measures are intended to gauge accuracy of the ADCIRC-2DDI tidal predictions.

Errors for individual tidal constituents are quantified by distance in the complex plane  $D$ , calculated (Foreman and Henry 1993):

$$D = \sqrt{(A_o \cos P_o - A_m \cos P_m)^2 + (A_o \sin P_o - A_m \sin P_m)^2}, \quad (4.3)$$

where  $A_o$ ,  $A_m$ ,  $P_o$ , and  $P_m$  are the observed and modeled amplitudes and phases, respectively.

#### 4.2.2 Mass Balance Check

An important property of any coastal circulation model is mass conservation. For several model experiments, global mass balance checks are conducted by comparing changes in water volume within the domain to the flux in/out of the domain. The methodology used for these calculations is described in detail by Kolar et al. (1994b).

### 4.3 Base Simulation

Taking into consideration the suggestions of TFF organizers and participants, as well as using experience gained from numerous ADCIRC model simulations, a base simulation is created that offers an ideal combination of simplicity and performance (accuracy) without tuning model parameters. The model equations implemented are fully nonlinear and include a quadratic parameterization of nonlinear bottom friction forces, nonlinear convective acceleration terms (both space and time derivatives), and nonlinear finite amplitude terms. The quadratic nonlinear friction factor  $C_f$  is set equal to  $2.322 \times 10^{-3}$  and the GWCE weighting factor is defined by  $\tau_o = 0.0006$ . The meaning for these parameters was given in Sec. 2.3.1. Along the open boundary, 11 tidal constituents (six primary, five nonlinear) are forced. For all simulations, no normal flow, free tangential slip land boundaries are used. Tidal potential forcing is not activated and the Coriolis parameter is spatially constant, a consequence of the Cartesian coordinate system that is employed. Wind forcing is not included in this study.

The coefficient for lateral eddy viscosity is equal to zero, and a minimum depth of 10 m is specified to prevent drying of mesh elements. A complete description of the ADCIRC-2DDI model equations was provided previously in Sec. 2.3.

## 5.0 RESULTS FOR THE BASE SIMULATION

Semidiurnal frequencies dominate the tidal response in the southern North Sea/English Channel. For the primary semidiurnal tides, which include  $M_2$ ,  $S_2$ ,  $K_2$ , and  $N_2$ , one amphidrome is present in the southern North Sea and one virtual amphidrome is evident in the English Channel near Christchurch. Relative to the southern North Sea, sea surface heights associated with the semidiurnal tides tend to be higher on the continental side of the water body and in the English Channel. These characteristics are shown in Fig. 3a and b for the dominant  $M_2$  tide. Diurnal tides tend to be larger in the North Sea than in the English Channel and exhibit no real amphidromes. The quarter-diurnal tides have amphidromes evenly distributed throughout the model domain with two in the English Channel and one or more in the southern North Sea.

The tidal response at three transects across the model domain are shown in Fig. 4a, which includes the underlying bathymetry and Fig. 4b, which places the transects in the Cartesian coordinate framework. Amplitudes of the dominant diurnal, semidiurnal, and  $M_2$  overtide frequencies across each transect are compared in Fig. 5a–c. Minima observed in these plots are indicative of proximity to an amphidrome or virtual amphidrome. In general, the higher frequency nonlinear tides exhibit greater spatial variability and sensitivity to bathymetry as expected.

Across transect 1, a virtual amphidrome of the  $K_1$  tide is apparent near the channel constriction at the Dover Strait. The dominant  $M_2$  frequency and its  $M_4$  overtide are both larger at the southern end of this transect, which is located in waters slightly shallower than those at the northern reach of the transect. Again, local lows in the  $M_6$  amplitude indicate positions of two amphidromes. Amplitudes of the nonlinear tides,  $M_4$  and  $M_6$ , are approximately 10–12% of the  $M_2$  tidal amplitude; these nonlinear tides are largest near the Dover Strait, suggesting possible excitation by the geometry at the constriction.

Transects 2 and 3 clearly show that the dominant astronomical tides are larger near the French side of the English Channel. This is attributed to a Kelvin wave that propagates northward through the channel (Proudman 1953). Across transect 2, the  $M_4$  and  $M_6$  constituents are excited on the shallow, broad shelf along the northern coast; the same is true for the  $M_4$  constituent on the mildly sloped northern coast of transect 3. In contrast, the  $M_6$  constituent over transect 3 is small due to the presence of an amphidrome.

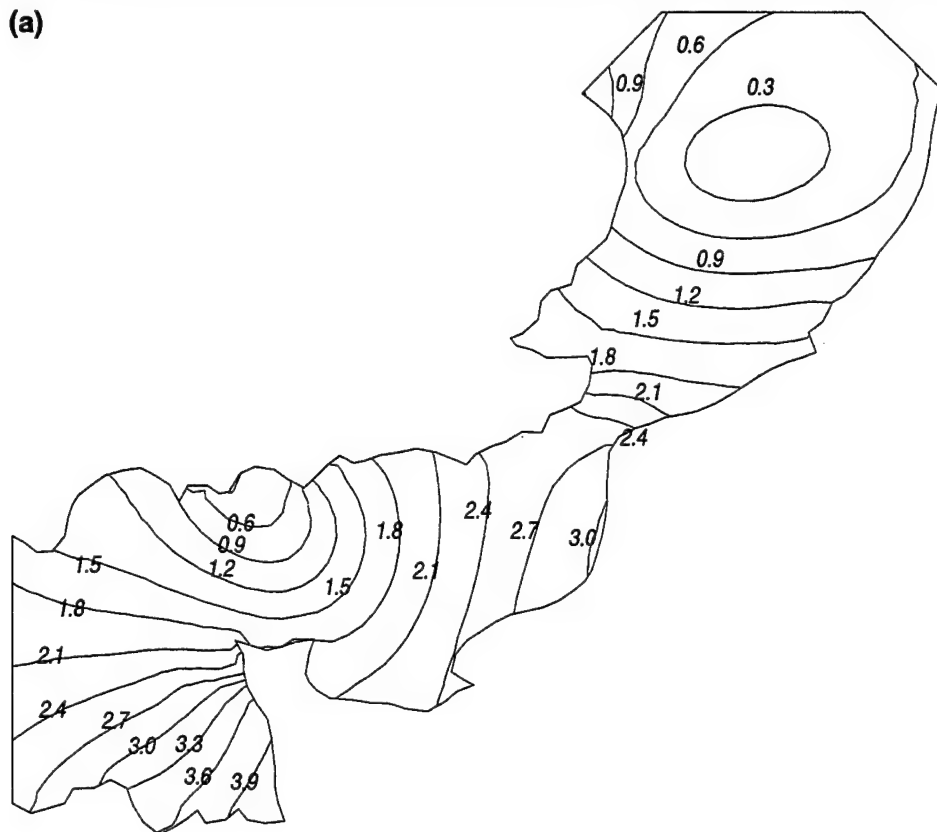
No overall conclusions can be drawn regarding the generation of nonlinear tides in the North Sea/English Channel model domain. Depths everywhere in the model domain are considered shallow in relation to tidal dynamics and, thus, nonlinear tides are largely affected by local bathymetric changes.

### 5.1 Elevation Time Series Comparisons

#### 5.1.1 Observations vs. Raw Model Predictions

Initially, raw model computations for the base simulation are compared to observations. In general, the observed time series for elevation that contains only 11 tidal constituents compares favorably with raw model predictions comprised of an infinite number of internally generated constituents. Table 1 presents an RMS error for each of the elevation stations. The full set of tidal elevation time series model-data comparisons using the base simulation, raw model predictions is found in App. A. Differences evident in these time series warrant further investigation and a truer model-data comparison using “filtered” model computations.

(a)



(b)

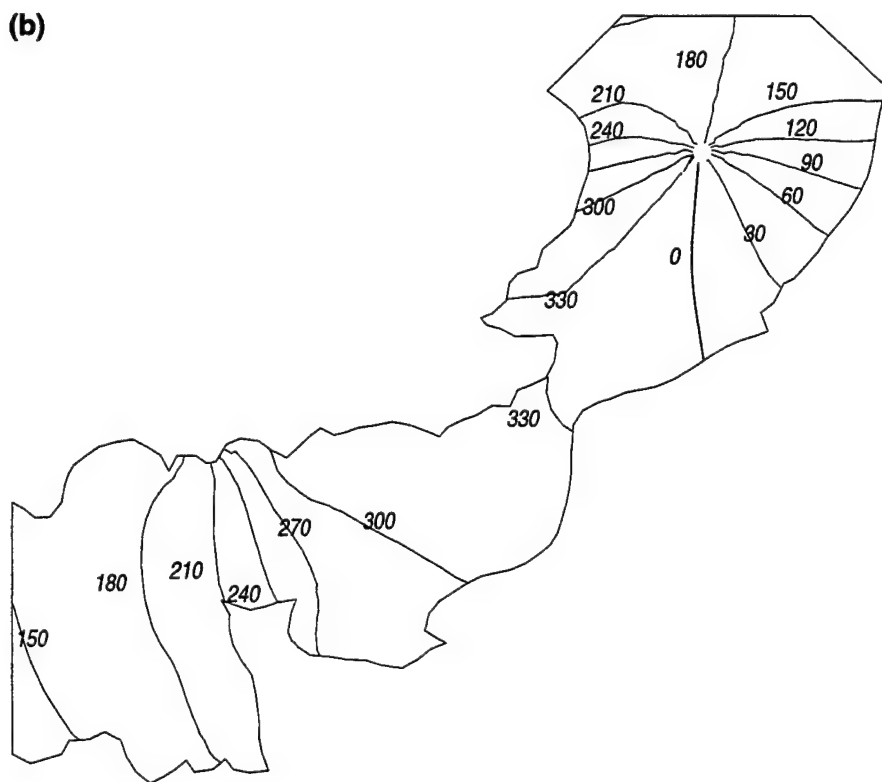


Fig. 3 — M2 base simulation, (a) amplitudes (meters) and (b) phases (degrees)

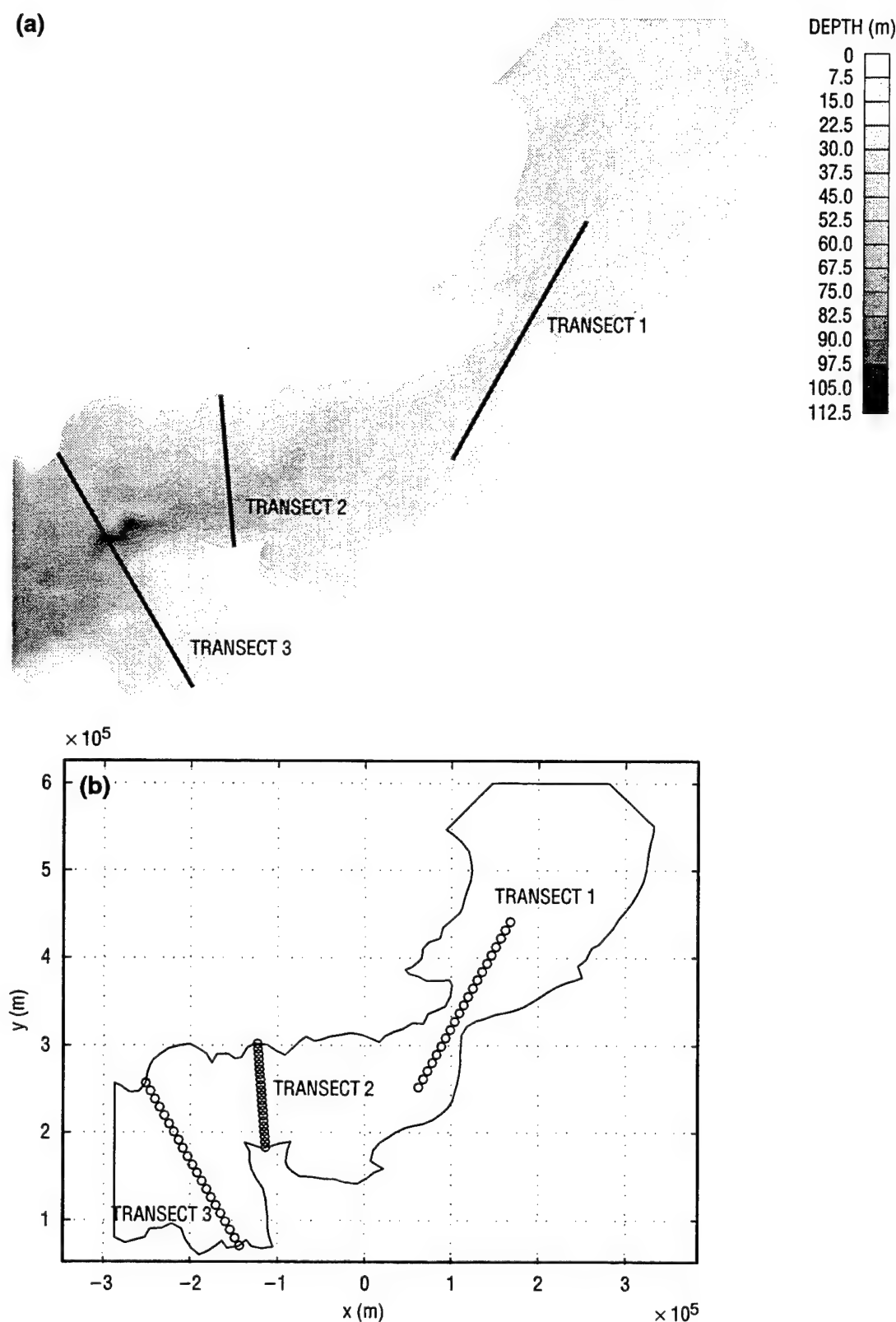


Fig. 4 — Grid transects, (a) depths and (b) Cartesian coordinates

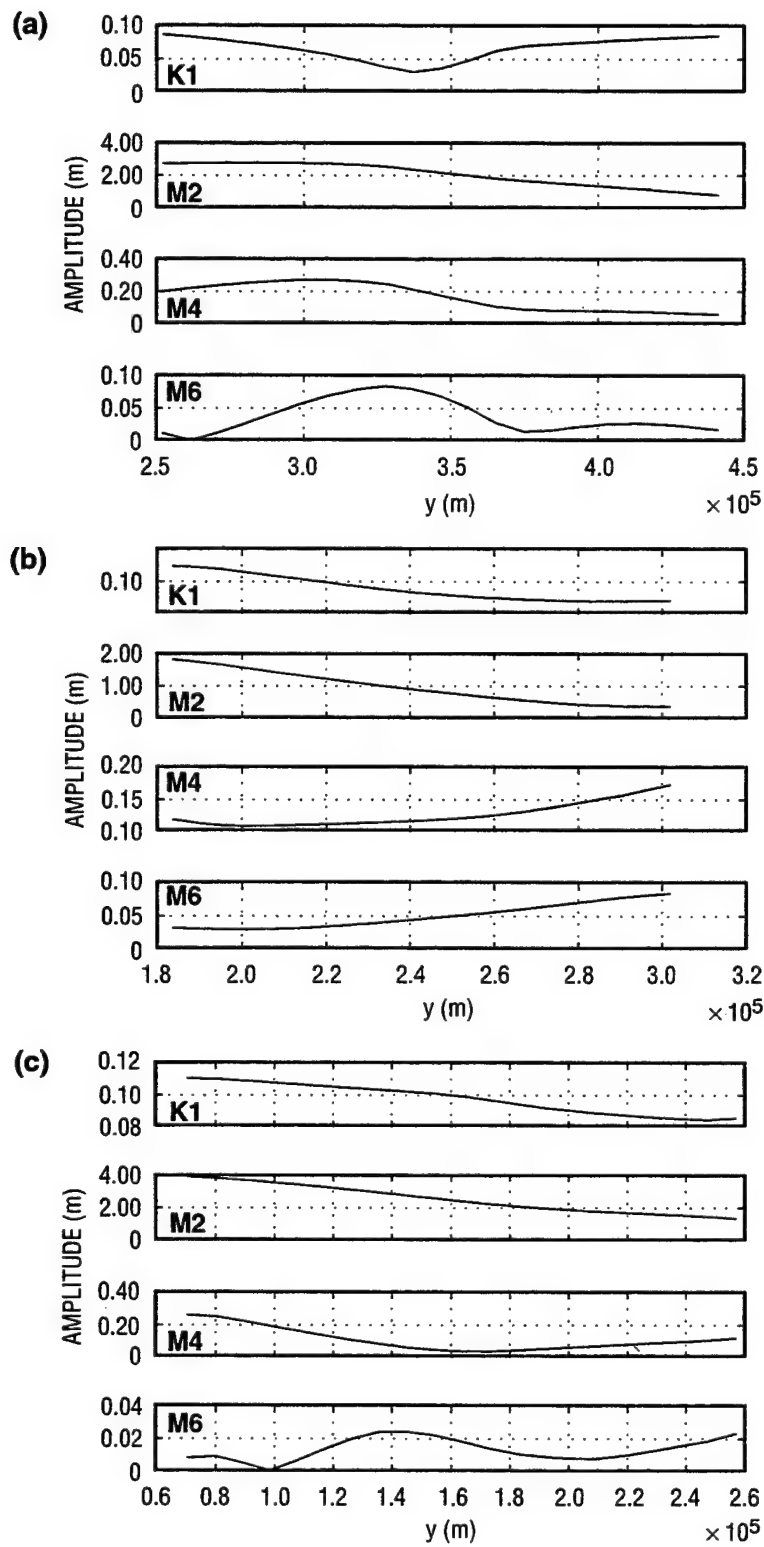


Fig. 5 — Constituent amplitude variations across transects (a) 1, (b) 2, and (c) 3

Table 1 — RMS Errors for Raw Elevation Model-Data Comparisons

GAUGE LOCATION	RMS ERROR (cm)	GAUGE LOCATION	RMS ERROR (cm)
St. Malo	39.6	Hoek van Holland	16.6
Cherbourg	22.4	Walton	36.9
Dieppe	55.5	Dover	28.4
Boulogne	40.7	Christchurch	24.9
Calais	49.6	Lowestoft	8.4
Zeebrugge	34.3		
MEAN	32.5		

### 5.1.2 Observations vs. "Filtered" Model Predictions

A fair model-data comparison involves only that portion of the model response due to the same 11 constituents comprising the tidal elevation gauge observations. Long-term simulations harmonically decomposed for 56 tidal constituents are used to reconstruct a time series based on only these 11 TFF constituents. Time series reconstruction follows from Eq. (3.1). The reconstructed time series essentially "filters" all other tidal frequencies from the model-computed response. Use of the filtered model solution results in more valid model-data comparisons. Overall agreement between the filtered model predictions and the data is improved as seen from the RMS errors presented in Table 2. A complete set of filtered tidal elevation model-data comparisons at all 11 stations is found in App. B. For the period 15–18 Mar, an average proportional error,  $\epsilon^2 = 0.010$ , is calculated for 10 of the 11 stations. The remaining station, Christchurch, is excluded from this average because of its obviously deviant proportional error of 0.086. Most likely, the poor agreement at Christchurch can be attributed to the station's location near a semidiurnal "virtual" amphidrome. Near this virtual amphidrome, semidiurnal tidal amplitudes are small and large, spatial gradients of phase are evident (refer to Fig. 3a and b).

The time series for elevation gauges at Calais, Hoek van Holland, and Christchurch are presented in Fig. 6a–c. Improvements in the agreement between model and data suggest that compared to errors previously computed for the raw model solution, constituents excluded from the data are not negligible. An elevation time series of the excluded tidal constituents at each of stations Calais, Hoek van Holland, and Christchurch (shown in Fig. 7a–c) confirms that these constituents are

Table 2 — RMS Errors for Filtered Elevation Model-Data Comparisons

GAUGE LOCATION	RMS ERROR (cm)	GAUGE LOCATION	RMS ERROR (cm)
St. Malo	19.2	Hoek van Holland	12.7
Cherbourg	13.9	Walton	26.4
Dieppe	29.8	Dover	14.0
Boulogne	14.9	Christchurch	14.4
Calais	30.7	Lowestoft	8.8
Zeebrugge	16.2		
MEAN	18.3		

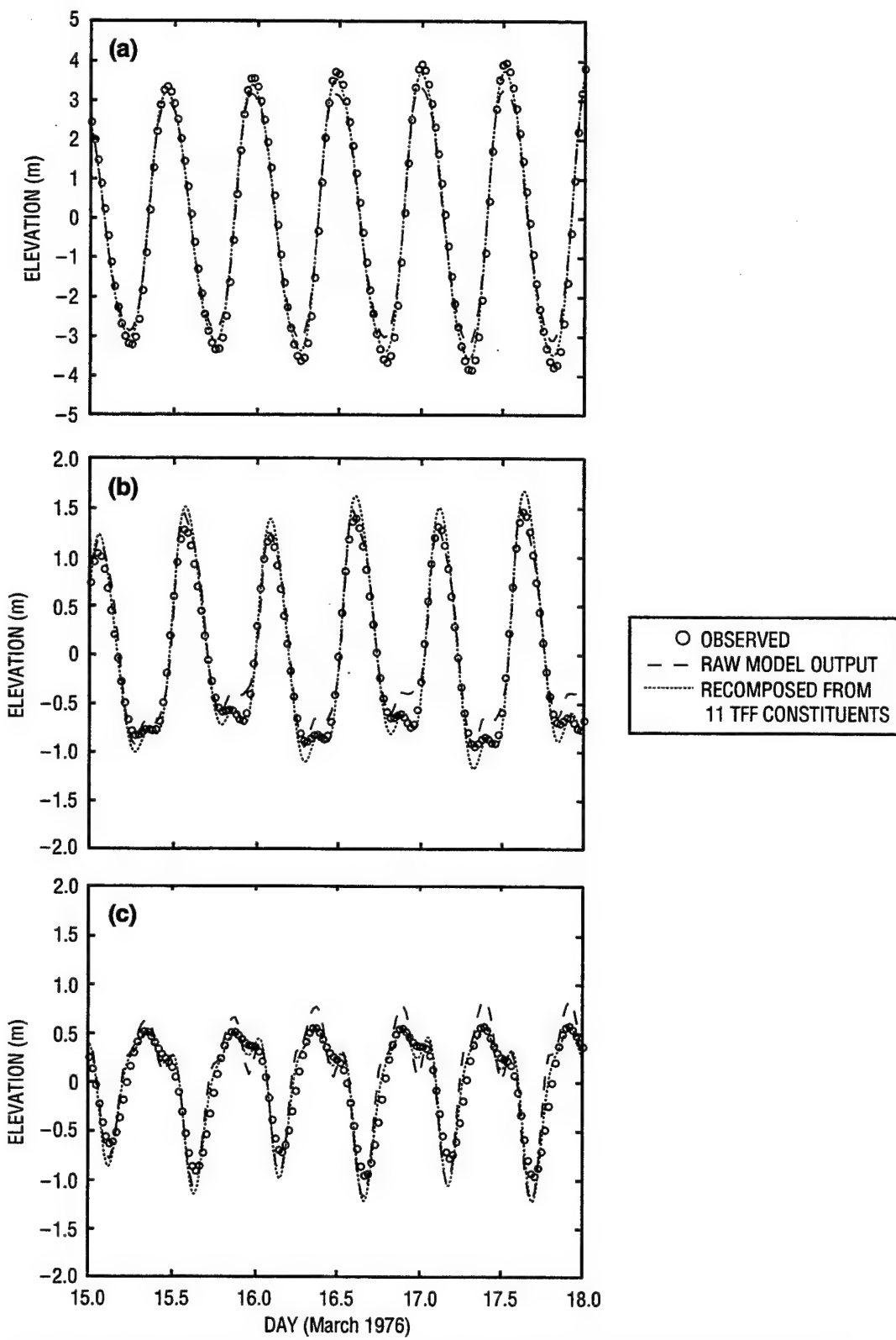


Fig. 6 — Base simulation tidal elevations at tidal gauges (a) Calais, (b) Hoek van Holland, and (c) Christchurch

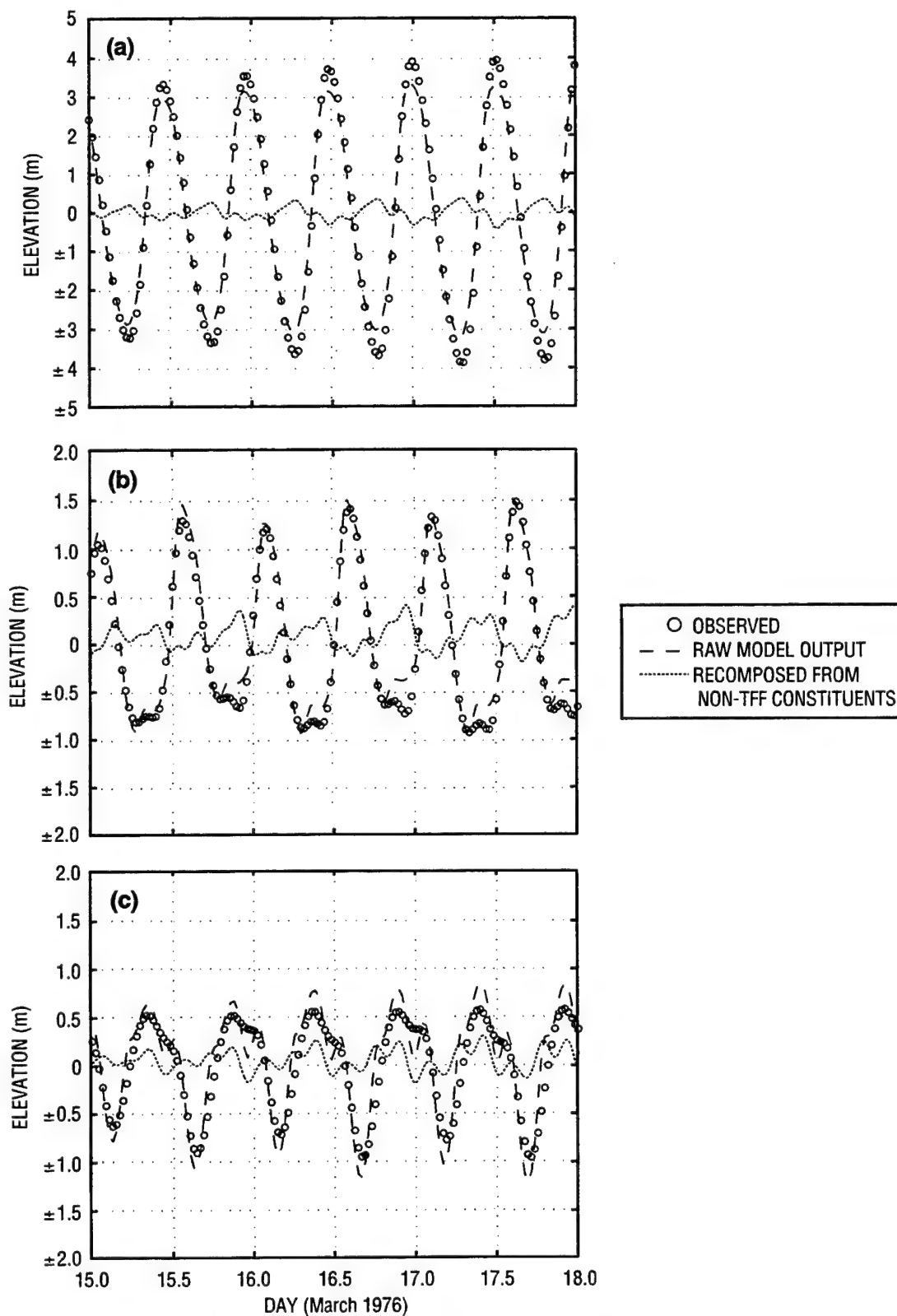


Fig. 7 — Comparison with non-TFF constituents at tidal gauges (a) Calais, (b) Hoek van Holland, and (c) Christchurch

indeed significant. From the harmonic analysis, constituents  $M_2$  and  $\mu_2$  (not included in the TFF data) are typically larger than the smallest signals associated with the 11 TFF constituents. Other investigators have made similar observations based on computations from their models (e.g., Werner and Lynch 1989; Jamart and Ozer 1989). Even though errors with respect to the measured data are smaller for filtered model results, one should keep in mind that in all likelihood, the raw model time series predictions are closer to reality. True sea surface elevations are unfiltered and contain contributions from a wide band of frequencies. For this reason, raw model solutions are used for the sensitivity analyses that follow in Sec. 6.0.

Apart from the elevation time series comparisons, the 11 TFF constituents are compared individually to the observations. Appendix C contains figures that depict, for each station and tidal constituent, the amplitude and phase errors and a calculated value for the error in the complex plane  $D$ . Constituent phase errors, on average, are larger than error associated with amplitude. However, the largest errors in phase are most often associated with tidal constituents that have small amplitudes. Thus, it is thought that these constituents have only a minor impact on the overall accuracy of computed elevations. In some instances, particularly with high-frequency, nonlinear constituents, large phase errors do lead to increased values of  $D$ . The large phase errors exhibited by nonlinear tidal components are not surprising, since high-frequency (and, therefore, shorter wavelength) tides exhibit larger spatial gradients in phase. Except at Christchurch and Lowestoft, the greatest source of error as measured by  $D$  is in amplitude of the semidiurnal tidal constituents. These constituents, as noted in Sec. 5.0, have several amphidromic points in the domain and it is well known that positioning of amphidromes has a pronounced effect on computed phases.

Consistently, agreement between model-computed elevations and the data is far better at those gauges located closest to the open boundaries. This outcome is not surprising, since specified elevations comprise the forcing at these boundaries. As mentioned previously, the quality of model predictions at Christchurch may be strongly influenced by its proximity to an amphidrome and perhaps by omission of the Isle of Wight. No correlation between error and gauge location are observed with respect to depths at the gauge location, offshore slope at the gauge, the geographic location (Continental or British waters), or strength of the tidal nonlinearities at the gauge.

## 5.2 Velocity Time Series Comparisons

RMS errors from comparisons between the velocity time series computed by ADCIRC-2DDI and measured velocity time series at each of the eight velocity stations is presented in Table 3. (The directional errors are not extremely meaningful as the largest error tends to occur when the speed is small and direction is changing 180°, i.e., between the tidal flood and ebb.) Appendix D contains the complete set of time series plots showing these comparisons. From the plotted comparisons shown in App. D and from velocity comparisons made by other investigators using depth-integrated models, it seems that speed observations at several locations are of marginal value. For two of the gauges, poor correspondence to modeled velocity is explained by the unfortunate vertical placement of the gauges. Gauges 4 and 8 are located near the bottom at a depth approximately 4/5 of the total water depth as noted by Walters (1987). In this situation, the measured speeds are expected to be much lower than a depth-averaged speed (e.g., Fig. 8a and b). At gauges 1, 3, and 6, comparisons to ADCIRC-2DDI computed velocities are good (e.g., Fig. 8c–e), indicating that perhaps at these locations, the measured velocities are well represented by depth-averaged velocities. It is possible that comparisons to current measurements of this type could be improved by using velocities computed by a 3D tidal model; Lynch and Werner (1984) conducted such a study with the JONSDAP'76 data used here, but no improvement was observed.

Table 3 — RMS Errors for Raw Velocity  
Model-Data Comparisons

GAUGE NUMBER	SPEED RMS ERROR (m/s)	DIRECTION RMS ERROR (deg)
1	.16	12.7
2	.31	19.9
3	.20	39.9
4	.27	51.9
5	.20	26.8
6	.10	40.2
7	.20	37.7
8	.22	31.4
MEAN	.21	

Encouragingly, those simulations that were most accurate with regard to elevation also compared best with respect to velocity. It should be noted that because velocity observations are, indeed, the raw data, as opposed to a filtered form (i.e., the elevation observations), there is no reason to filter raw model velocity computations for comparison.

### 5.3 Performance Comparison to Other Models

As part of and subsequent to the Tidal Flow Forums, a sizable number of researchers have used the TFF benchmark case to assess their own models' performance (e.g., Ozer and Jamart 1988; Jamart and Ozer 1989; Yu et al. 1989; Praagman et al. 1989a, b; Werner and Lynch 1987; Gray et al. 1987; Walters 1987; Lynch and Werner 1988; Werner and Lynch 1989; Gray 1989; Baptista et al. 1989; Walters and Werner 1989; Werner 1995). RMS errors computed for the last 25 h of the ADCIRC-2DDI simulations performed here are compared to RMS error measures published for other models. In general, ADCIRC-2DDI performed well, equaling or exceeding the accuracy of other models for both raw model computations and filtered prediction comparisons based on the 11 TFF constituents. Table 4 contains the RMS values for seven models including the ADCIRC-2DDI model results described herein.

These inter-model comparisons should be approached with caution. A 25-h time period is considerably short for meaningful comparisons. Comparisons using longer time series may lead to an entirely different ranking of model "skill level" (Jamart and Ozer 1989). Also, variations exist with respect to the computational mesh used by various TFF investigators. Many of the earlier modelers used the original FE grid discussed previously. Others used finite difference grids and curvilinear grids that offer slightly different discretizations of the domain. Furthermore, not all modelers compare observations to the model solution at actual gauge locations; rather, several simply compare the model response at a node in the mesh nearest to the observation location. A minority of TFF investigators present model results that include only the 11 TFF constituents; most present raw model time series (or a full spectrum solution in the case of frequency domain models).

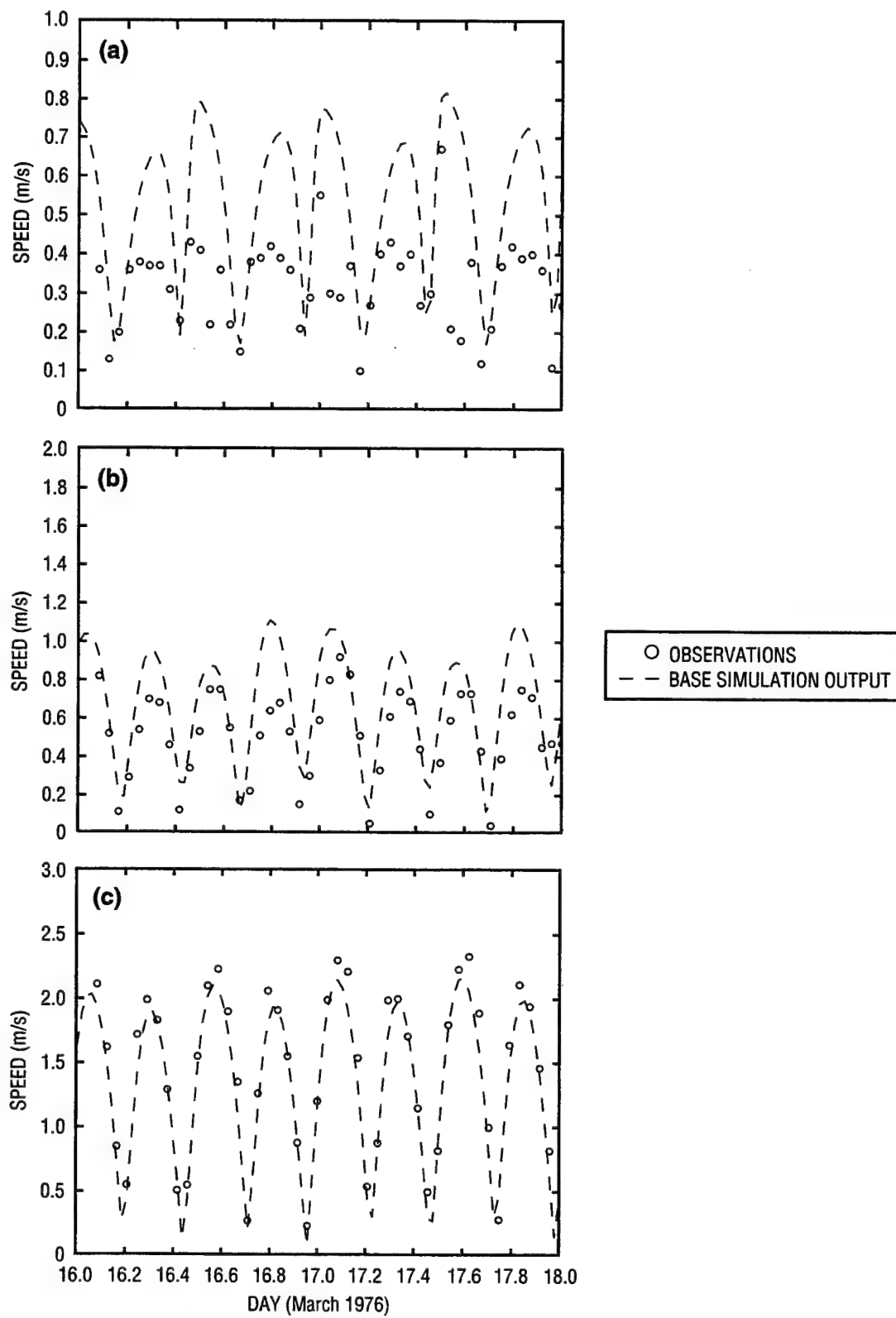


Fig. 8 — Base simulation speeds; velocities at gauges (a) 4, (b) 8, and (c) 1

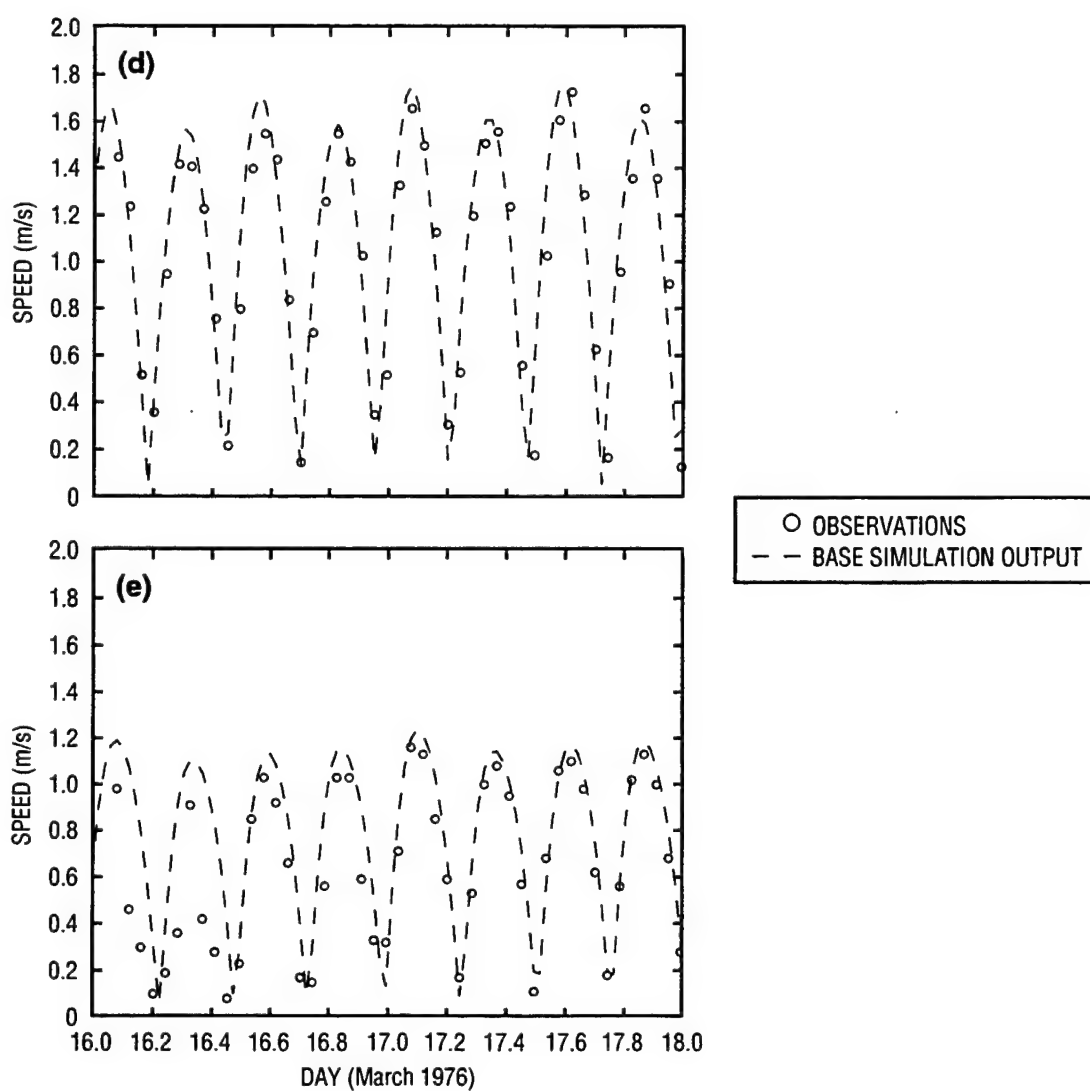


Fig. 8 — (cont.) (d) 3 and (e) 6

Table 4 — Model-Model Comparisons for the TFF Benchmark Case

MODELS	RMS ERROR (cm) (FILTERED)	RMS ERROR (cm) (UNFILTERED)	INVESTIGATORS
ADCIRC-2DDI	18.0	32.5	Blain and Rogers 1998
WEQN	22.0	36.0	Werner and Lynch 1989
FADI		42.0	Yu et al. 1989
WAQUA		38.0	Praagman et al. 1989a
MU-model		35.0	Ozer and Jamart 1988
MU-model	27.0 (96 constituents)		Jamart and Ozer 1989
Walters	28.0		Walters 1987

## 6.0 SENSITIVITY ANALYSES

### 6.1 Description

Sensitivity analyses are conducted to investigate tidal dynamics in the coastal environment in the context of evaluating the implementation and performance of the ADCIRC-2DDI model in simulating these flows. Modularity of ADCIRC-2DDI is a tremendous asset in such a study by allowing terms in the model equations, such as nonlinearities and various forcing mechanisms to be systematically rendered active or inactive.

Four sources of nonlinearity are contained in the model equations; they are associated with the (1) quadratic bottom stress formulation, which is dependent on  $V^2$ , (2) finite amplitude terms, those terms involving gradients of the sea surface elevation,  $\nabla \zeta$ , (3) spatial derivatives of the convective acceleration terms, e.g.,  $v \cdot \nabla v$ , and (4) temporal derivatives of the convective acceleration terms, e.g.,  $\partial V / \partial t$ . "Switches" contained in the model input specifications control the inclusion or exclusion of these four types of nonlinearity. The independent effect of each of these nonlinearities is investigated with respect to their influence on the computed tidal dynamics and model stability.

Though several forms of forcing at the open-ocean boundary can be implemented in ADCIRC, only the elevation specified condition is investigated since this is the form of the data available in the TFF benchmark. Influence of the frequency content of this boundary elevation forcing on the model-computed response is examined. Other forcing mechanisms within the ADCIRC model include the tidal potential forcing that serves as a body force on the mass of the water body and a Coriolis effect accounting for latitude of the modeled region. Additionally, the ADCIRC model invokes physical and numerical parameters such as the bottom friction coefficient, horizontal mixing coefficient, model timestep, minimum bathymetric depth, and a value that characterizes the form of the continuity equation invoked  $\tau_o$ . All forcing and parameters just mentioned are the subject of this sensitivity study of the ADCIRC-2DDI model.

### 6.2 Nonlinearities

#### 6.2.1 Nonlinear Bottom Friction Parameterization

The tidal response of a basin is strongly influenced by topography. Consequently, the bottom friction parameterization plays a significant role in the computed tidal response. Bottom friction within ADCIRC-2DDI can be represented using either a linear relation or the standard quadratic parameterization identified in the presentation of Eqs. (2.7)–(2.9). For the nonlinear bottom friction formulation, the model friction factor  $C_f$  can be equated to physical frictional coefficients such as the Manning or Chezy forms. In contrast, the linear bottom friction parameterization has a friction factor that is selected based on considerations of mass conservation, model stability, and/or model agreement with data (i.e., calibration) and has no physical basis.

In the North Sea/English Channel, both linear and nonlinear representations of the bottom stress clearly capture a majority of the tidal signal as seen at four stations in Fig. 9a–d. No calibration of the nonlinear bottom friction factor is undertaken for these simulations so that consistency with the TFF benchmark is maintained. A nonlinear bottom friction representation is favored because of its physical basis for selection of  $C_f$ . Furthermore, model computations compare slightly better with observations when using the nonlinear bottom friction representation as compared to a calibrated linear bottom friction formulation.

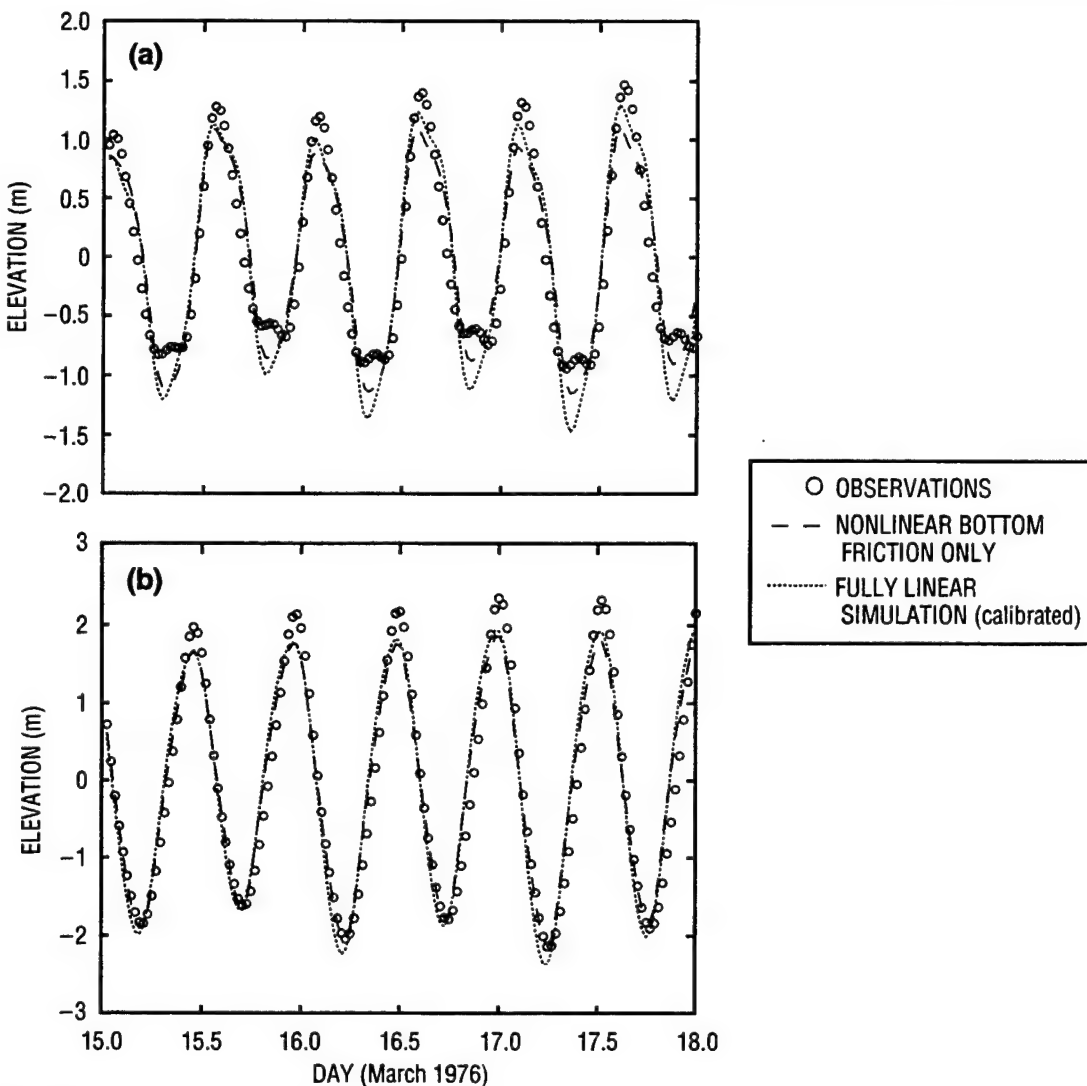


Fig. 9 — Effect of bottom friction parameterization; tidal gauges (a) Hoek van Holland and (b) Walton

A linear frictional coefficient of 6.0E-5 is found to give the best agreement with observations over the English Channel/North Sea. The use of much larger values for  $C_f$  leads to significant damping of the tidal signal. Simulations applying the larger linear frictional coefficients are, however, less problematic from a standpoint of mass conservation (to be discussed further in Sec. 6.4.1).

The role of the nonlinear bottom stress on different tidal frequencies is also examined. Nonlinearities associated with frictional forcing at the seabed influence to a greater extent the semidiurnal ( $H_2$ ) and sextidiurnal ( $H_6$ ) constituents. These effects are illustrated in plots of global amplitude differences for the  $M_2$  and  $M_6$  constituents that contrast simulations employing nonlinear and linear bottom friction formulations (Fig. 10a and b).

#### 6.2.2 Nonlinear Convective Acceleration Terms (Temporal Derivatives)

Westerink et al. (1992b) suggest that for the sake consistency between the continuity and momentum equations and for better mass conservation properties, nonlinear convective acceleration

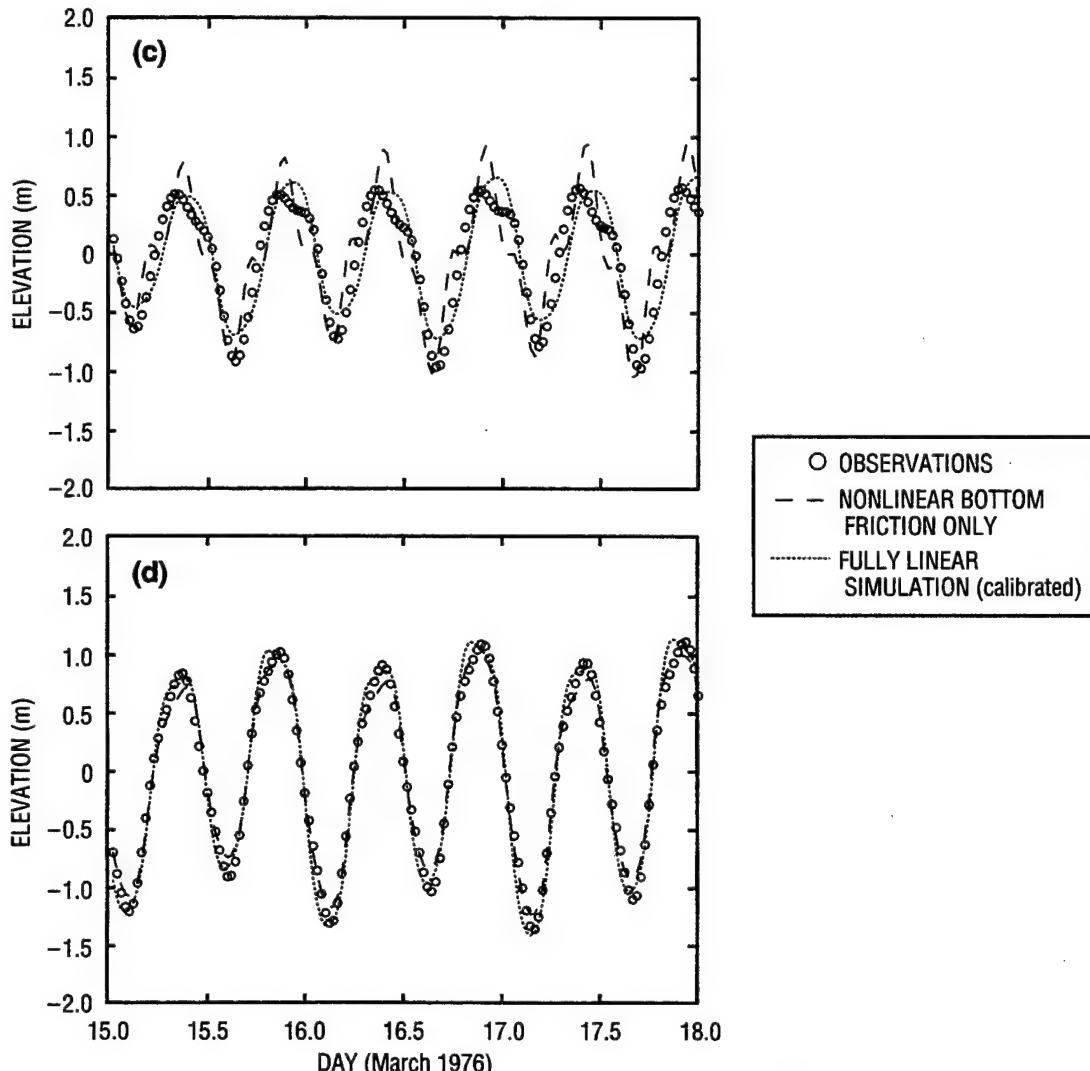


Fig. 9 — (cont.) (c) Christchurch and (d) Lowestoft

terms containing time derivatives be included if either nonlinear finite amplitude terms or spatial derivatives of the nonlinear convective acceleration terms are included in the model equations. Therefore, a sensitivity analyses for the time derivative terms is not performed independently and no conclusions are drawn regarding their individual effect on model performance.

#### 6.2.3 Nonlinear Finite Amplitude Terms

The total water depth is approximated either as the mean water depth,  $H = h$ , or as  $H = h + \zeta$ , where  $\zeta$  is the deviation from the mean water depth due to tidal effects (in this case). The latter representation for  $H$  introduces additional nonlinearity into the model momentum equations through terms that multiply water surface gradients by the total water depth, i.e.,  $H\nabla\zeta$ , the finite amplitude terms. Model simulations that include finite amplitude effects in addition to nonlinear bottom stress lead to slight increases in predicted sea surface height, which is most notable at the crests and troughs of the tidal cycle (Fig. 11a-c).

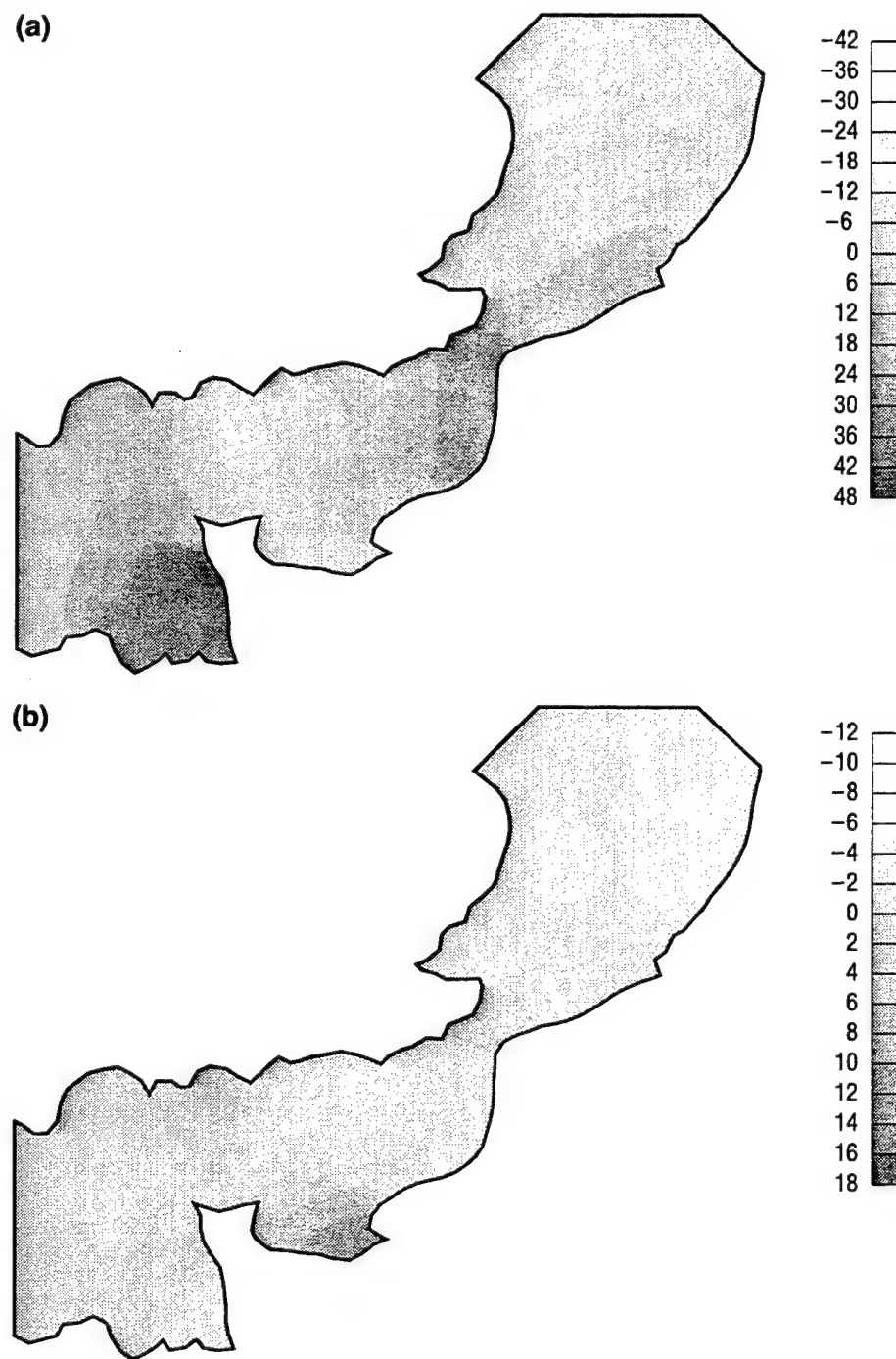


Fig. 10—Global amplitude differences (cm); amplitude with nonlinear bottom friction – amplitude with linear bottom friction, (a) M2 and (b) M6

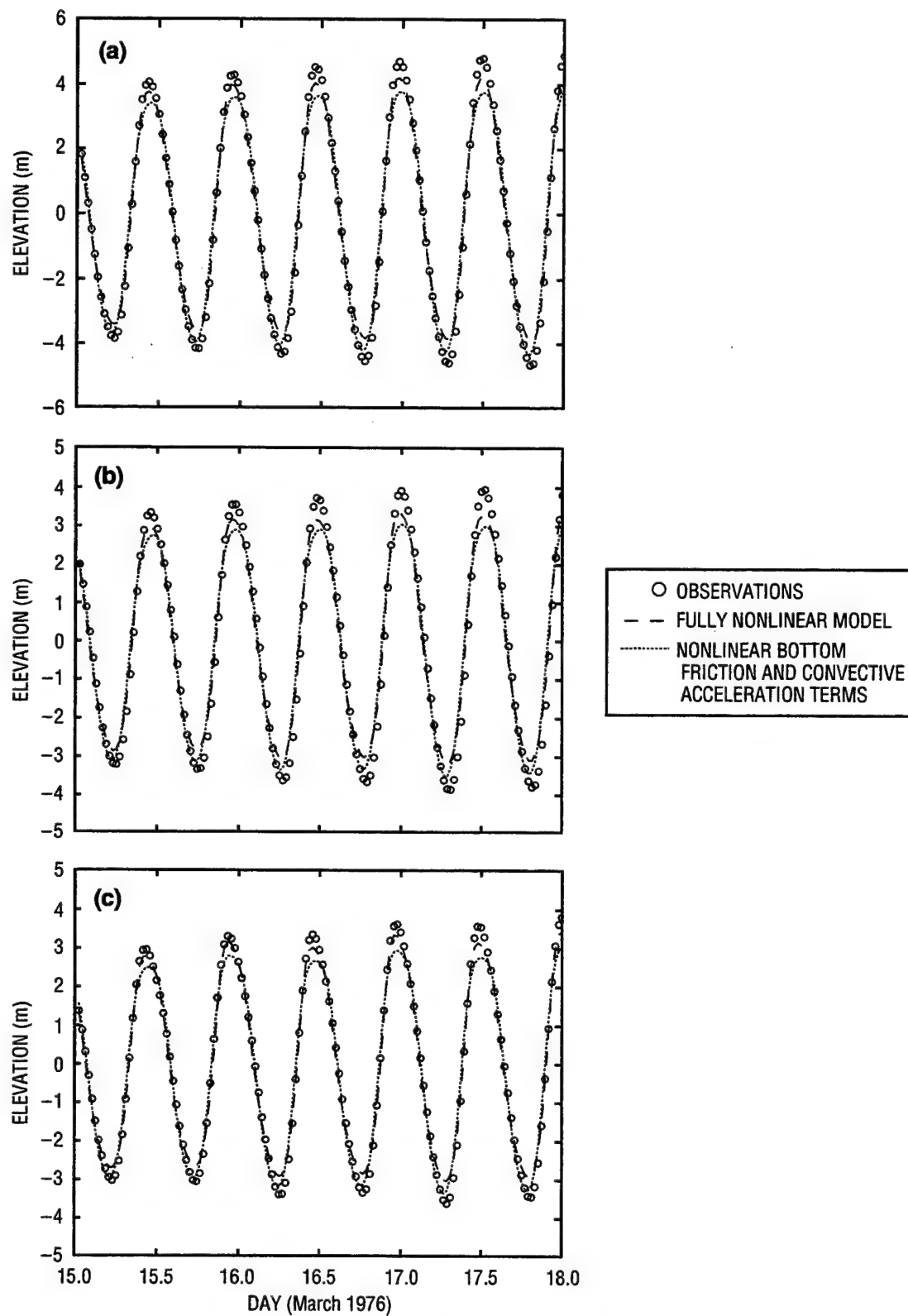


Fig. 11 — Effect of nonlinear finite amplitude terms; tidal gauges at (a) Dover, (b) Boulogne, and (c) Calais

While the bottom stress parametrization strongly effects the semidiurnal ( $H_2$ ) and sextidiurnal ( $H_6$ ) tidal frequencies, nonlinear finite amplitude terms primarily influence the quarter-diurnal ( $H_4$ ) and octodiurnal ( $H_8$ ) constituents. Global amplitude differences computed between the  $M_4$  and  $M_8$  tides are shown in Fig. 12a and b, respectively, which contrast simulations with and without the finite amplitude effects.

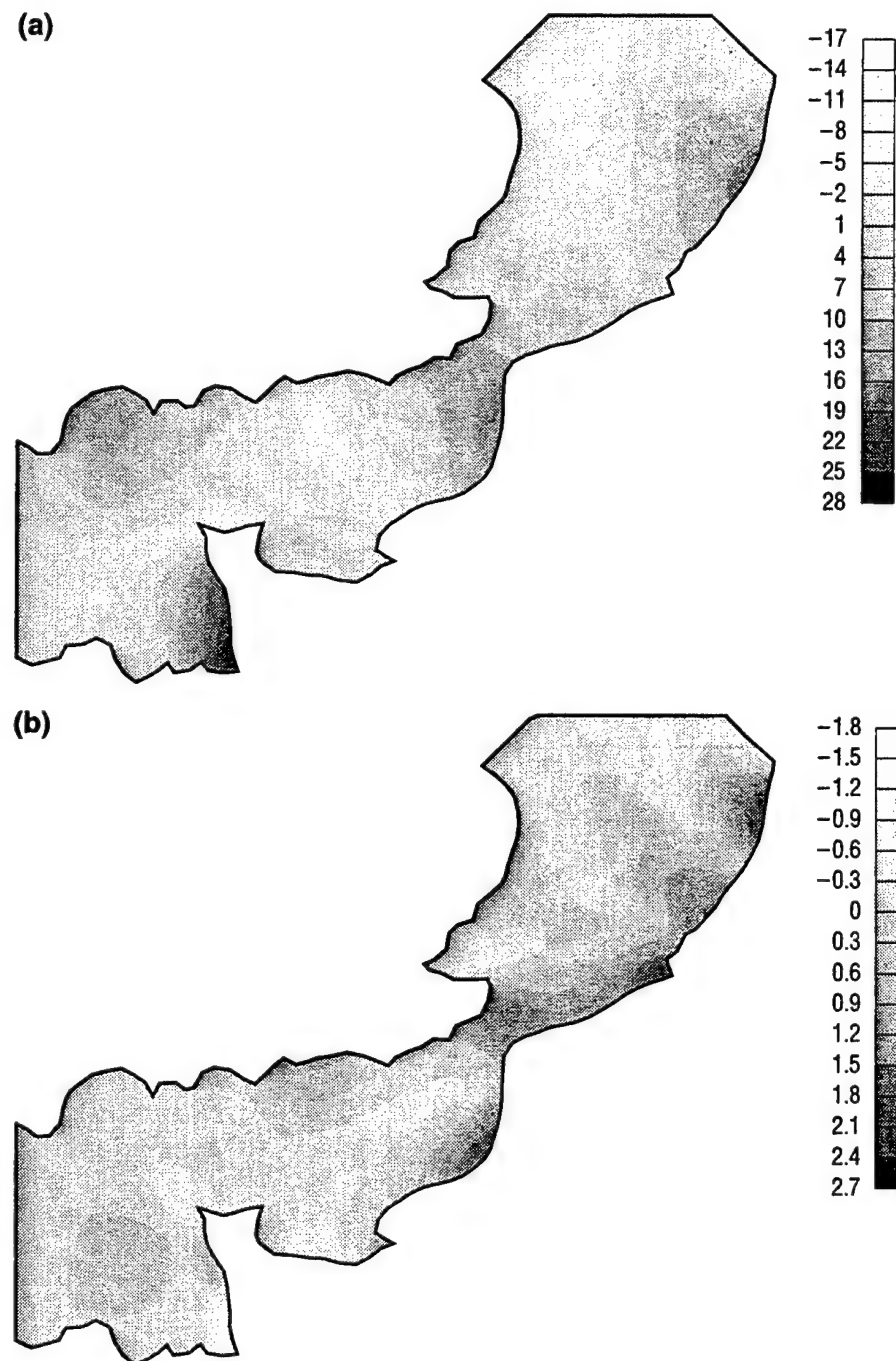


Fig. 12 — Global amplitude differences (cm); amplitude with finite amplitude terms – amplitude without finite amplitude terms, (a)  $M_4$  and (b)  $M_8$

Differences in the  $M_4$  tidal constituent between the two simulations are considerable west of the Cherbourg peninsula and near the Dutch coastline. A time series comparing the quarter-diurnal constituents from the two simulations to observations at a gauge location on the Dutch coast is shown in Fig. 13.

#### 6.2.4 Nonlinear Convective Acceleration Terms (Spatial Derivatives)

Inclusion of the spatial derivatives of the convective acceleration terms in the model equations together with nonlinear bottom stress terms results causes a slight reduction in the surface water elevation at the crests and troughs of the tidal cycles in Fig. 14a and b. A notable difference in the computed tides is observed when both the finite amplitude and convective acceleration terms are either included or excluded from the model equations (see Fig. 15a-d comparing the full nonlinear solution to a solution that has bottom stress as the only nonlinearity).

The influence of the nonlinear mechanisms associated with the finite amplitude and convective terms is clearly evident in the contributions of five nonlinear TFF constituents to the total tidal elevation as shown in Fig. 16a-c. These five constituents are largest when all nonlinear terms are included in the model computations. Furthermore, the strength of these nonlinear tidal constituents indicates that nonlinear interactions within the domain (facilitated through the nonlinear terms in the model equations) as opposed to nonlinear forcing at the boundary are largely responsible for generation of the nonlinear tidal response. This is most evident at Boulogne, which is far from open boundaries where the five nonlinear constituents are forced. The North Sea/English Channel is an excellent example of nonlinear tidal generation in shallow waters and demonstrates the necessity of a nonlinear hydrodynamic model for the prediction of shallow-water tidal dynamics.

Not surprisingly, tidal circulation is also altered by the inclusion or omission of the finite amplitude and convective acceleration terms. The speed of the flow is particularly affected with

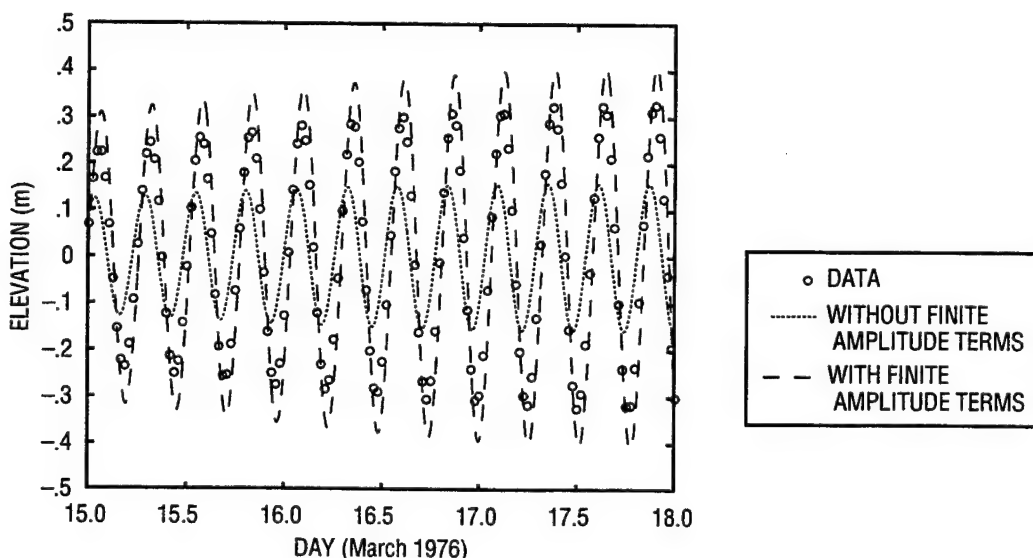


Fig. 13 — Effect of finite amplitude terms on three quarter-diurnal TFF constituents; tidal gauge at Hoek van Holland

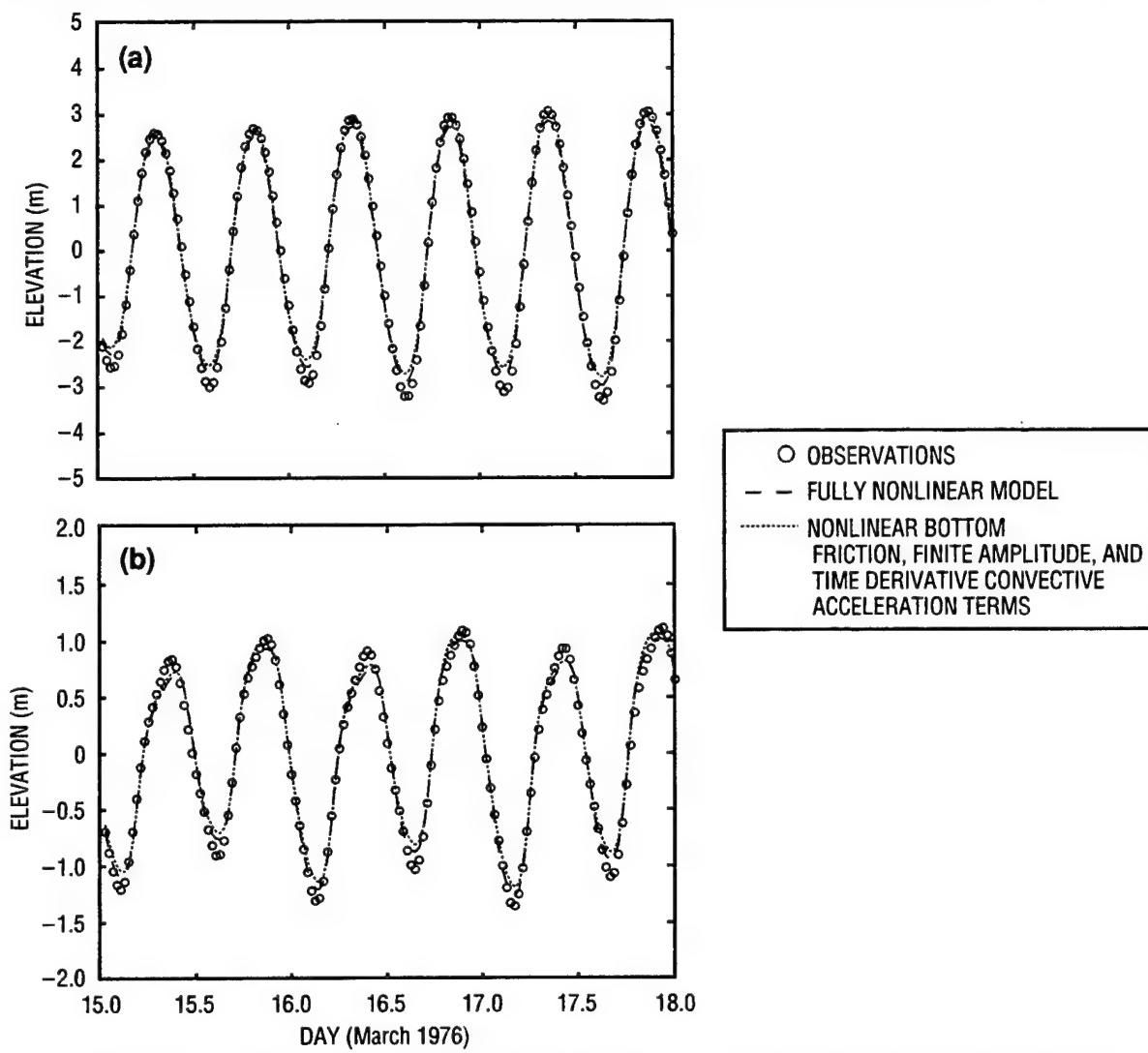


Fig. 14—Effect of convective acceleration terms, tidal gauges at (a) Cherbourg and (b) Lowestoft

directions altered to a much lesser degree. Global differences computed with respect to speed emphasize this point and are shown in Fig. 17 for simulations with and without the finite amplitude and convective acceleration terms collectively.

#### 6.2.5 Effect of Nonlinearities on Accuracy of Filtered Model Solutions

Here, the inclusion of model nonlinearities on filtered model-to-data comparisons is examined. The model predictions used for comparison contain only those 11 TFF constituents included in the observations. Table 5 contains proportional errors computed from comparisons between elevation time series for a 3-d time period (0000 15–18 Mar). Predictions from 10 of the 11 tidal elevation gauges are included in computations of the average error in each time series; Christchurch is excluded for reasons previously discussed. Clearly, when nonlinear terms are active in the model equations, model-to-data comparisons significantly improve as reflected by smaller proportional

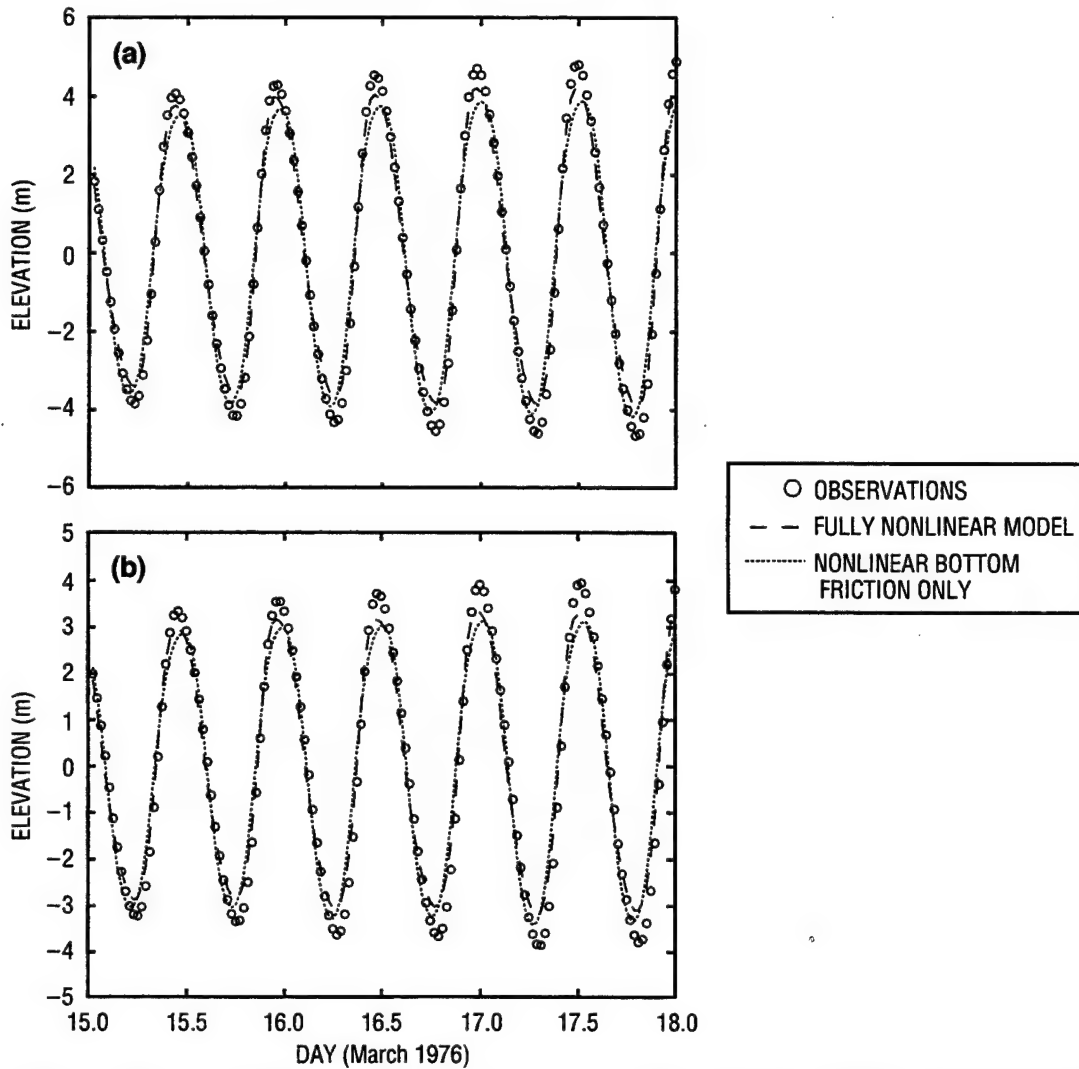


Fig. 15 — Effect of finite amplitude and convective acceleration terms, tidal gauges at (a) Lowestoft and (b) Calais

errors. Figure 18a-d further illustrates the effect of full nonlinearity on the computed tidal response as compared to the measured sea surface heights at four gauges. Recall that Fig. 9a-d compared the model response from the nonlinear bottom friction alone to the field observations.

### 6.3 Forcing

#### 6.3.1 Inclusion of Tidal Constituents

For this study case, six linear and five nonlinear tidal constituents are provided at the open boundaries. Often, tidal dynamics on the continental shelf are difficult to characterize. In particular, nonlinear tidal constituents are generally not known a priori so that most often, only deep-water, primary tidal constituents are applied as boundary forcing. For the North Sea, two forms of the boundary forcing are examined: the first contains only six primary TFF constituents and the second

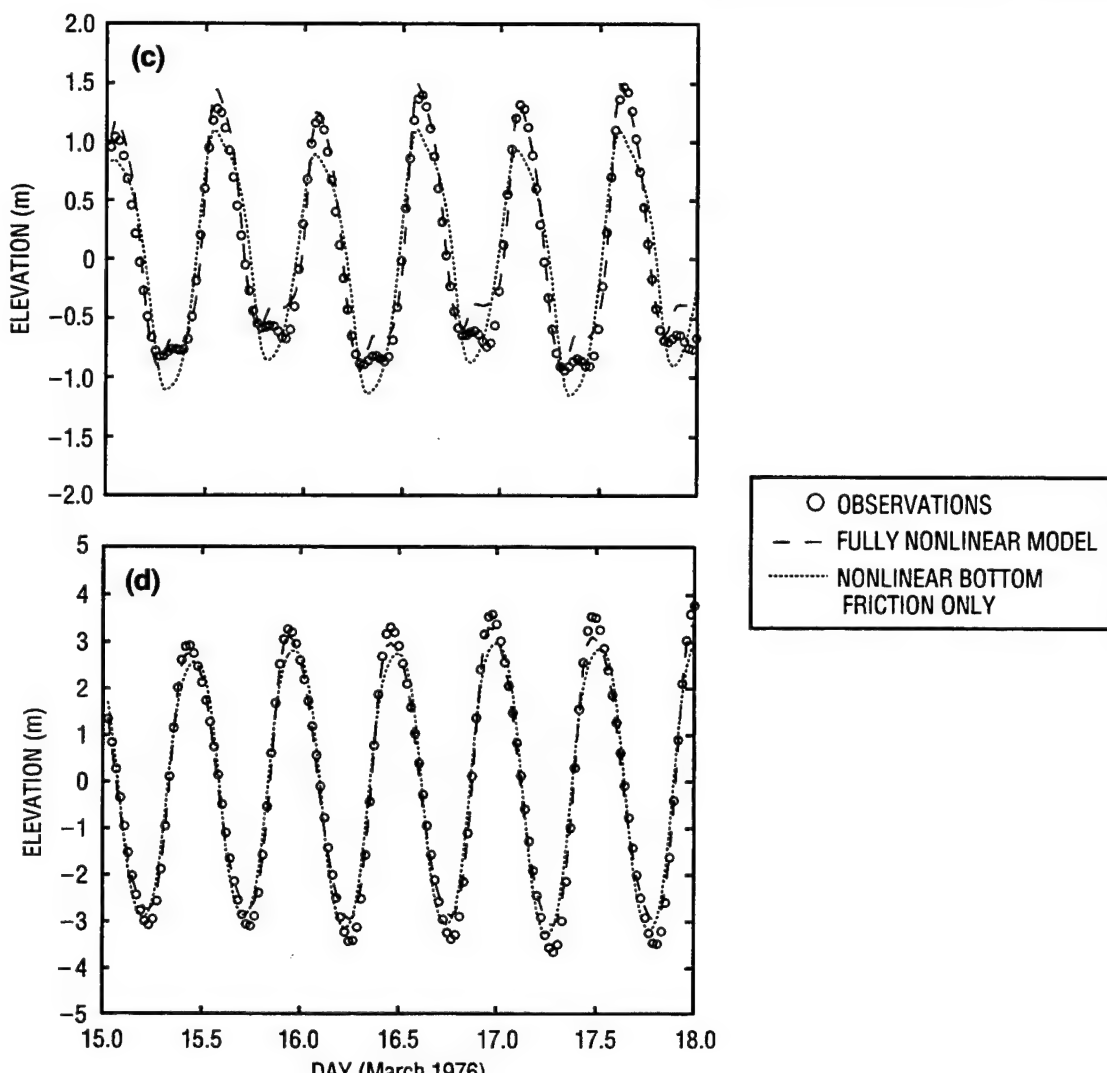


Fig. 15 — (cont.) (c) Hoek van Holland and (d) Dover

uses all 11 TFF constituents. Inclusion of the nonlinear tidal constituents does have a slight effect on model results as seen in Fig. 19a and b. The differences between tidal predictions forced with and without nonlinear tides is at least partially a result of the open-ocean boundary location in relatively shallow water (<120 m) where nonlinear tides are significant. One would expect errors for all tidal constituents if any other than the 11 TFF constituents are significant at the open boundaries, due to nonlinear interactions with improperly forced non-TFF tidal constituents (Werner and Lynch 1989).

Tables 6a and b list the calculated values for the error in the complex plane  $D$  (averaged for 11 gauges) for each of the 11 TFF constituents computed by the model. Comparison of the simulations, which include all constituents in the boundary forcing (Table 6a) and those using only six primary tidal constituents for forcing (Table 6b), clearly demonstrates the benefit of including nonlinear constituents in the boundary forcing.

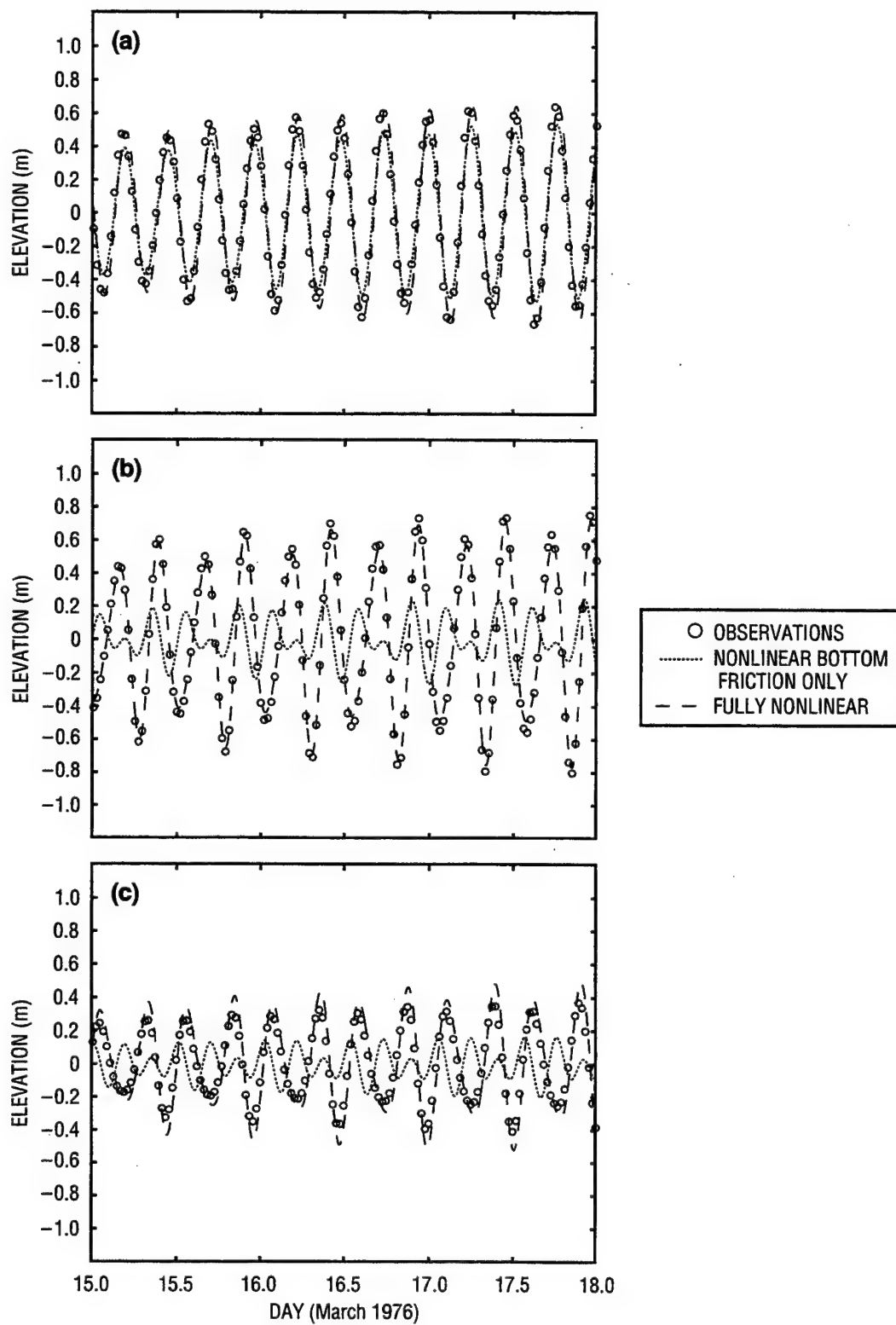


Fig. 16—Effect of finite amplitude and convective acceleration terms on five nonlinear TFF constituents, tidal gauges at (a) St. Malo, (b) Boulogne, and (c) Hoek van Holland

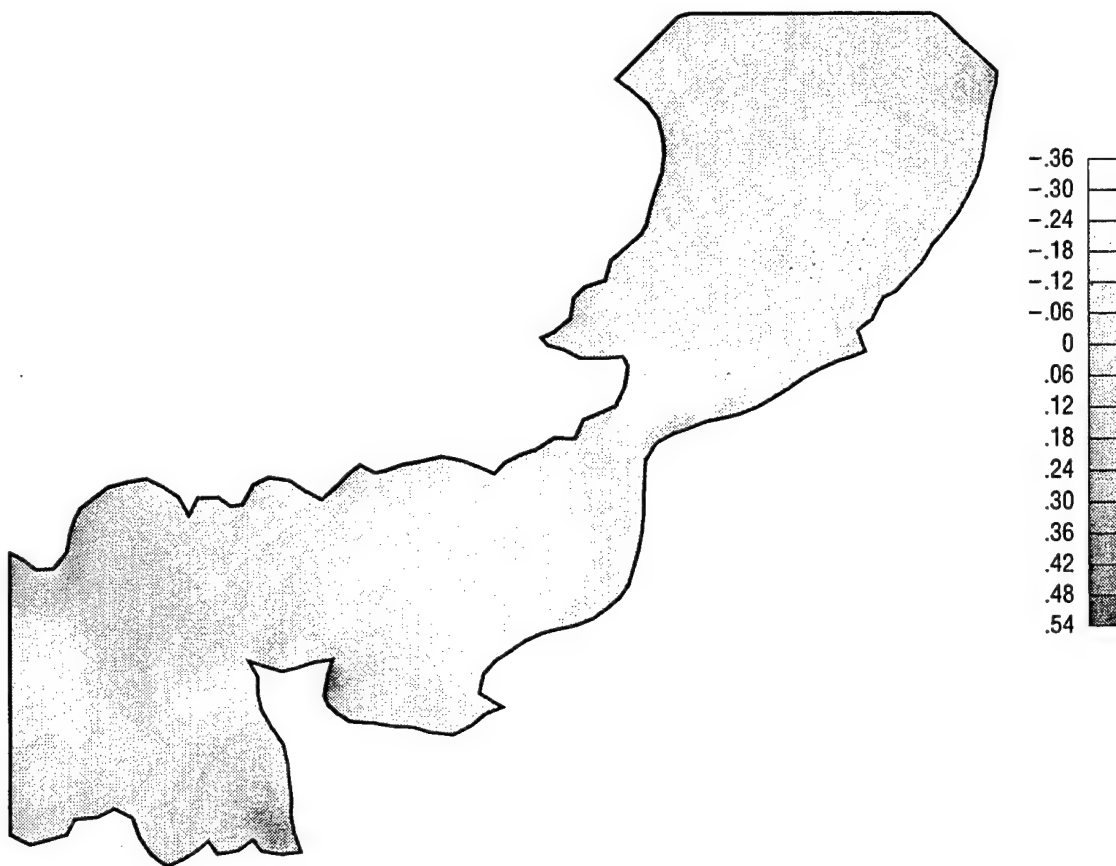


Fig. 17—Global speed differences (m/s); speed with finite amplitude and convective acceleration terms – speed without finite amplitude and convective acceleration terms

Table 5—The Role of Nonlinearity on Model-Data Comparisons

NONLINEAR BOTTOM STRESS	NONLINEAR FINITE AMPLITUDE TERMS	NONLINEAR CONVECTIVE ACCELERATION (Spatial Derivatives)	NONLINEAR CONVECTIVE ACCELERATION (Temporal Derivatives)	DIMENSIONLESS PROPORTIONAL ERROR, $\epsilon^2 \times 100$
yes	yes	yes	yes	1.07
yes	yes	no	yes	1.16
yes	no	yes	yes	1.82
yes	no	no	no	2.93
no	no	no	no	3.99 (with calibration)

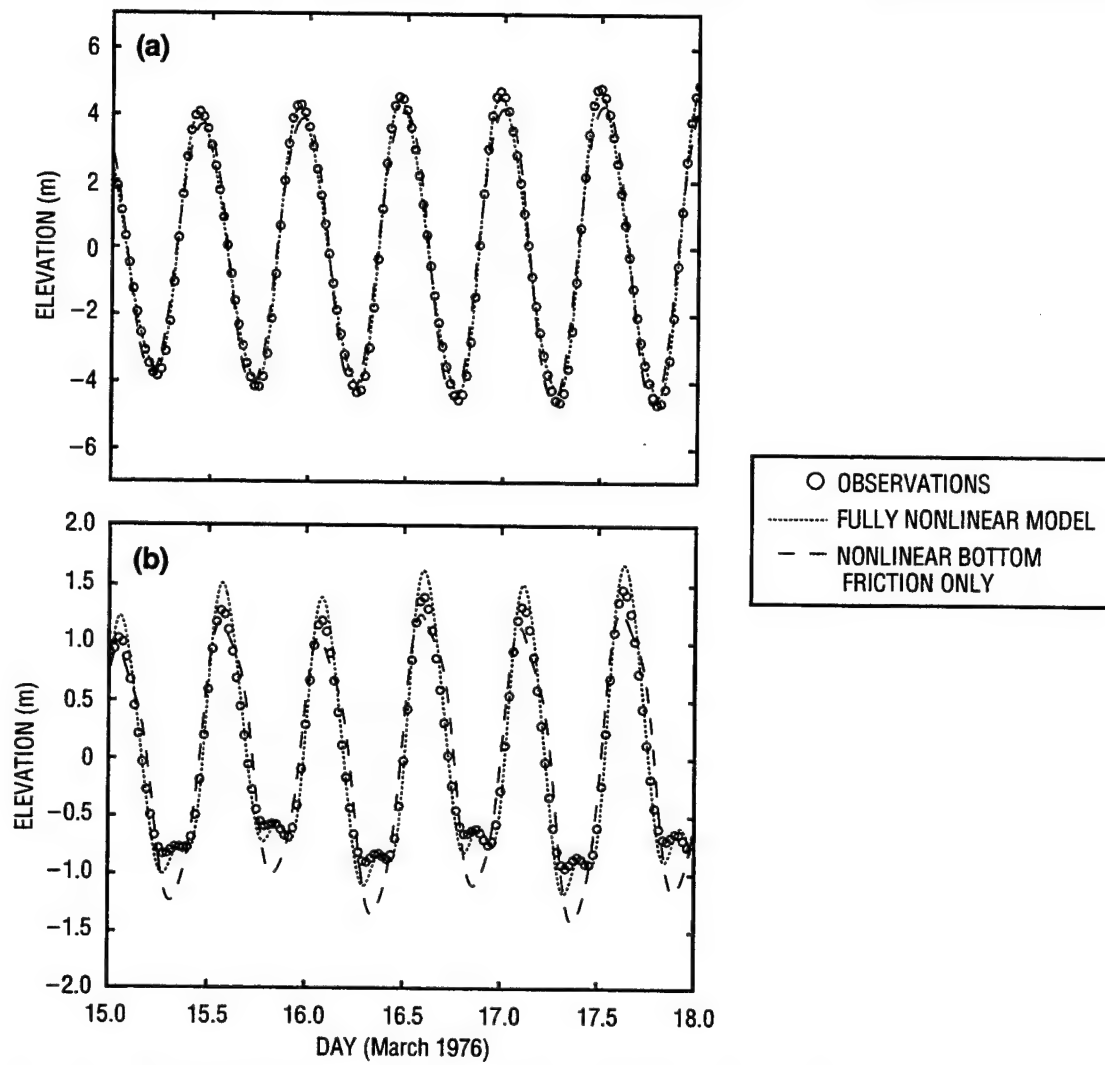


Fig. 18 — Effect of finite amplitude and convective acceleration terms on filtered model output, tidal gauges at (a) Bougues and (b) Hoek van Holland

### 6.3.2 Tidal Potential and Variable Coriolis Forcing

To include tidal potential forcing (a body force on the water mass due to the gravitational forces of the sun and the moon) and variable Coriolis forcing, a transformation of the model domain is made from Cartesian coordinates (supplied by the TFF organizers) to spherical coordinates:

$$\lambda = \lambda_o + \frac{x}{\cos \phi_o} \quad (6.1)$$

$$\phi = \phi_o \frac{y}{r}. \quad (6.2)$$

Here,  $x$  and  $y$  are Cartesian coordinates referenced to a longitude and latitude origin near the center of the grid  $(\lambda_o, \phi_o)$  and  $r$  is the radius of the Earth. For purposes of computing a variable Coriolis

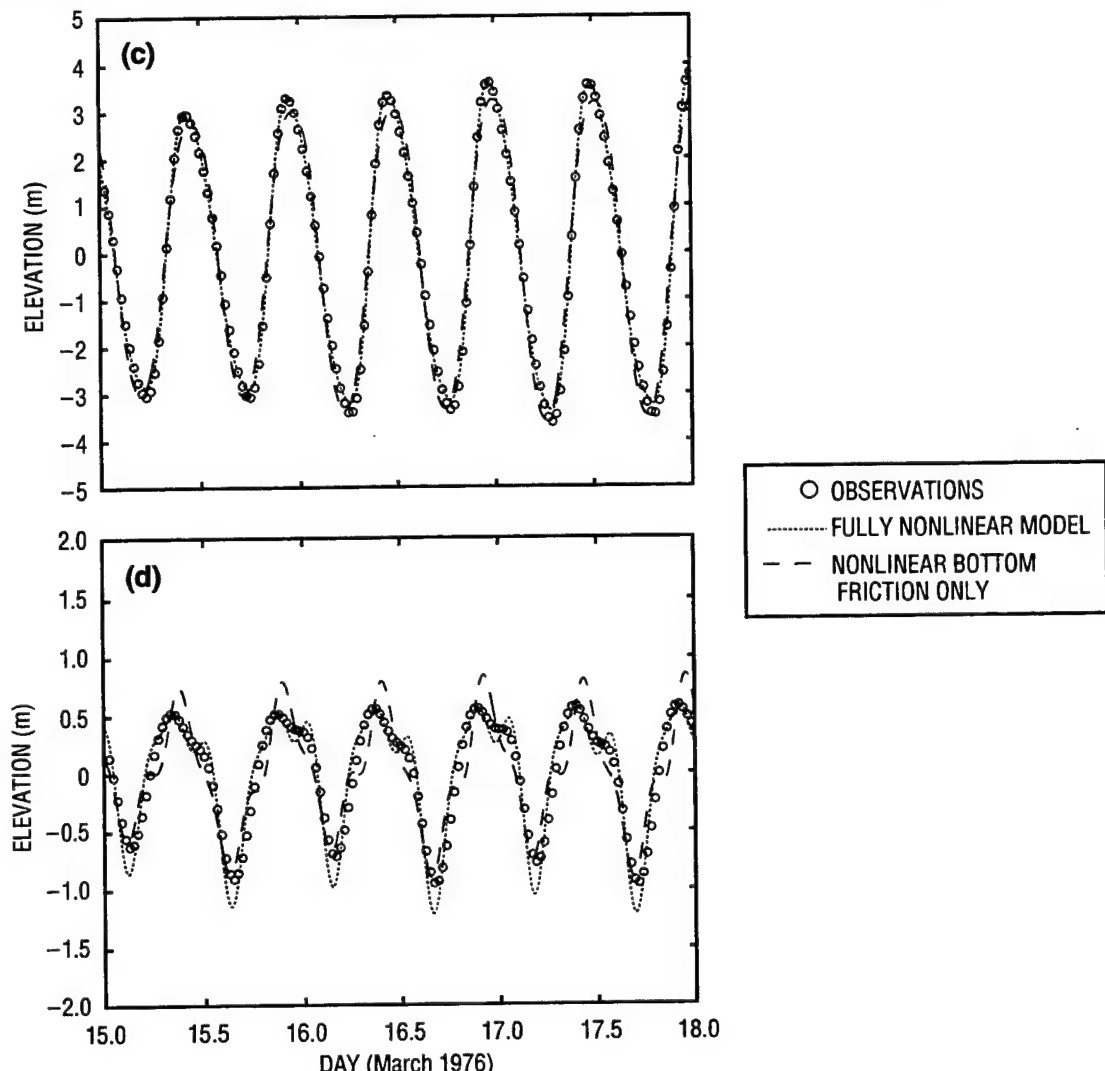


Fig. 18 — (cont.) (c) Dover and (d) Christchurch

forcing, the centroid of the domain is selected at  $0.3^\circ$  latitude and  $50.75^\circ$  longitude. In simulations including either the tidal potential or the variable Coriolis forcing, the added complexity does not result in any significant change in model tidal response. At some locations, velocity directions are slightly varied with the inclusion of tidal potential forcing and variable Coriolis forcing (e.g., Fig. 20a-c), but the effects are inconclusive. Though tidal potential forcing and the variability of Coriolis forcing seem to be insignificant for this relatively small study area, a larger domain covering a wider range of latitude will necessitate the inclusion of these two forcing mechanisms.

#### 6.4 Parameters

##### 6.4.1 Weighting Factor

The GWCE weighting factor,  $\tau_o$ , found in Eqs. (2.19) and (2.20), allows flexibility in the formulation of the equations implemented by ADCIRC-2DDI. For  $\tau_o = 0$ , the GWCE becomes a

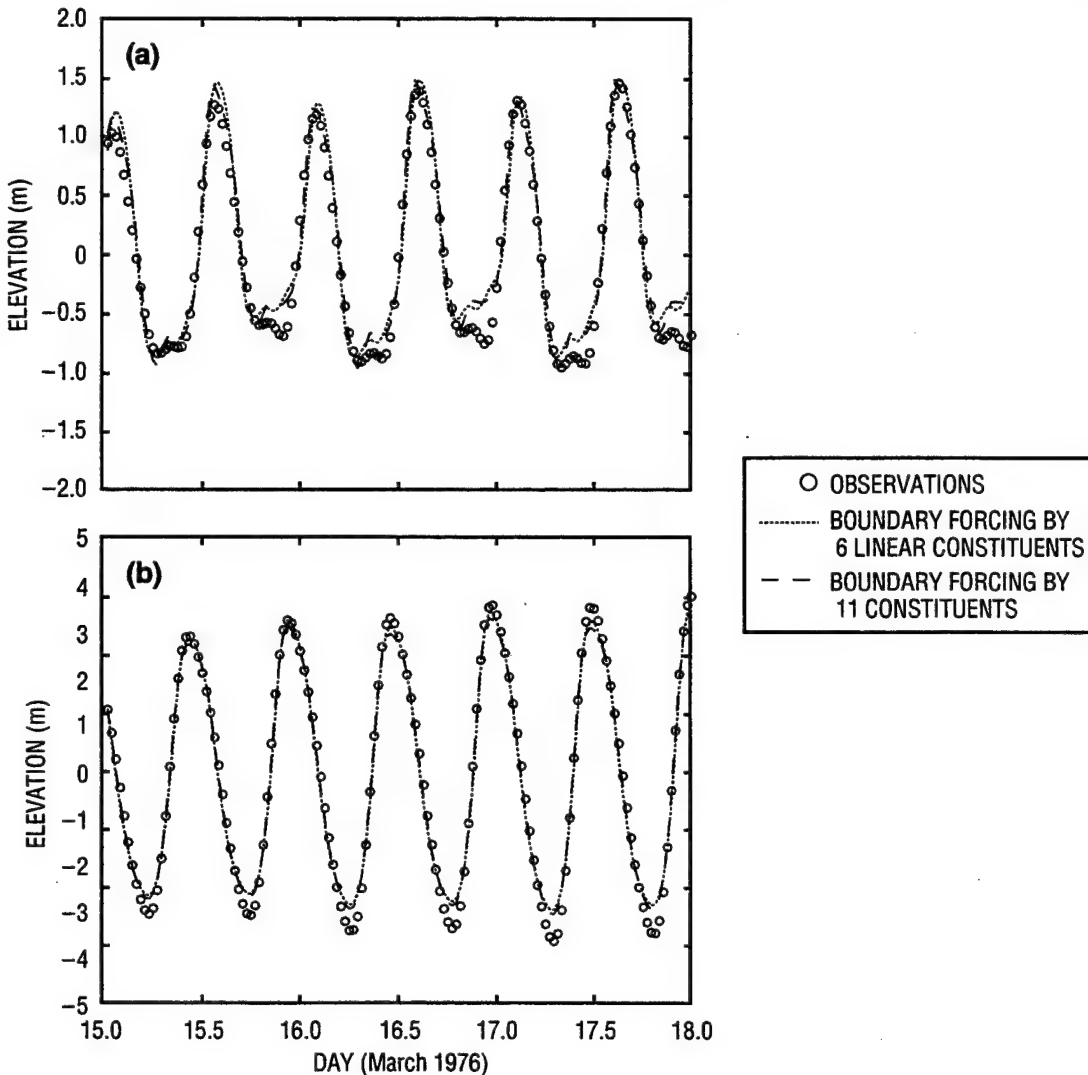


Fig. 19 — Effect of constituents in boundary forcing, tidal gauges at (a) Hoek van Holland and (b) Dover

pure wave equation, whereas large values of  $\tau_o$  shift the GWCE toward a primitive form of the continuity equation. Westerink et al. (1992b) state that  $\tau_o$  must be carefully chosen, as overly small values lead to mass conservation problems and too-large values result in instabilities caused by  $2 \cdot \Delta x$  waves. It is well known that FE approximations of the primitive equations suffer from spurious oscillations; this was a common problem for early generation FE models.

For cases in which nonlinear bottom stress is included, Westerink et al. (1992b) suggest setting the weighting factor equal to the maximum  $\tau_*$  for the simulation (e.g.,  $\tau_* = C_f(u^2 + v^2)_{max}/h_{min}$ ) and the model friction factor equal to the bottom friction coefficient  $C_f$ . Our experience indicates that  $\tau_* = [C_f(u^2 + v^2)/h]_{max}$  is less conservative, but nonetheless acceptable. When a linear bottom stress formulation is applied, it is suggested that  $\tau_o$  and the model friction factor be assigned identical values. Typically,  $\tau_o$  is determined by calibration or is based on the user's judgment and experience for a given application. Mass conservation is intimately tied to the specification of the

Table 6a — Elevation Errors for Boundary Forcing with 11 TFF Constituents

GAUGE LOCATION	O1	K1	M2	S2	N2	K2	M4	MS4	MN4	M6	2MS6	MEAN
St. Malo	.017	.018	.180	.075	.072	.033	.086	.069	.044	.018	.018	.057
Cherbourg	.015	.016	.107	.051	.023	.026	.055	.017	.014	.008	.012	.031
Dieppe	.015	.027	.170	.118	.074	.048	.035	.037	.025	.013	.021	.053
Boulogne	.014	.026	.100	.072	.040	.026	.032	.031	.020	.014	.014	.035
Calais	.015	.015	.242	.118	.068	.025	.054	.059	.020	.035	.024	.061
Zeebrugge	.011	.040	.120	.092	.138	.025	.041	.016	.024	.020	.039	.052
Hoek van Holland	.025	.006	.109	.014	.006	.011	.078	.018	.026	.019	.022	.030
Walton	.025	.035	.223	.105	.103	.027	.020	.029	.023	.017	.012	.056
Dover	.003	.016	.092	.034	.031	.017	.073	.034	.058	.017	.019	.036
Christchurch	.013	.004	.045	.033	.036	.008	.078	.041	.023	.071	.060	.037
Lowestoft	.016	.043	.040	.018	.025	.010	.023	.015	.002	.025	.061	.025
MEAN	.015	.022	.013	.066	.056	.023	.052	.033	.025	.023	.027	.043

Table 6b — Elevation Errors for Boundary Forcing with Six TFF Constituents

GAUGE LOCATION	O1	K1	M2	S2	N2	K2	M4	MS4	MN4	M6	2MS6	MEAN
St. Malo	.017	.018	.200	.066	.069	.035	.238	.151	.097	.038	.045	.088
Cherbourg	.015	.016	.103	.049	.022	.026	.101	.058	.033	.024	.032	.044
Dieppe	.016	.027	.163	.114	.073	.048	.064	.047	.033	.008	.012	.055
Boulogne	.015	.027	.097	.068	.038	.026	.090	.072	.041	.012	.029	.047
Calais	.016	.015	.242	.118	.066	.024	.065	.049	.029	.027	.004	.060
Zeebrugge	.012	.041	.120	.093	.136	.025	.046	.007	.021	.011	.037	.050
Hoek van Holland	.026	.007	.106	.012	.004	.011	.115	.057	.028	.052	.050	.043
Walton	.026	.035	.225	.107	.102	.027	.030	.008	.018	.010	.013	.055
Dover	.003	.016	.095	.033	.029	.017	.122	.080	.069	.016	.031	.046
Christchurch	.013	.004	.042	.034	.036	.008	.085	.040	.031	.073	.063	.039
Lowestoft	.017	.044	.040	.017	.024	.010	.031	.028	.016	.019	.016	.024
MEAN	.016	.023	.013	.065	.054	.023	.090	.054	.038	.026	.030	.050

parameter  $\tau_o$ . Mass balance properties are known to be suspect as the form of the GWCE continuity equation shifts towards a pure wave equation; for this situation, the largest errors have been shown to be located at the open boundaries.

Mass balance properties of model simulations are investigated here to gain better insight into the selection of  $\tau_o$  and determine the influence of other factors on mass conservation. The mass accumulation over time is shown in Fig. 21a and b for simulations using a linear bottom friction parameterization. Since the volume change in mass and mass flux into the domain should be equal, mass balance errors are represented as the difference between these two curves. It is uncertain whether the smaller discrepancy in mass for the uncalibrated linear friction simulation is a result

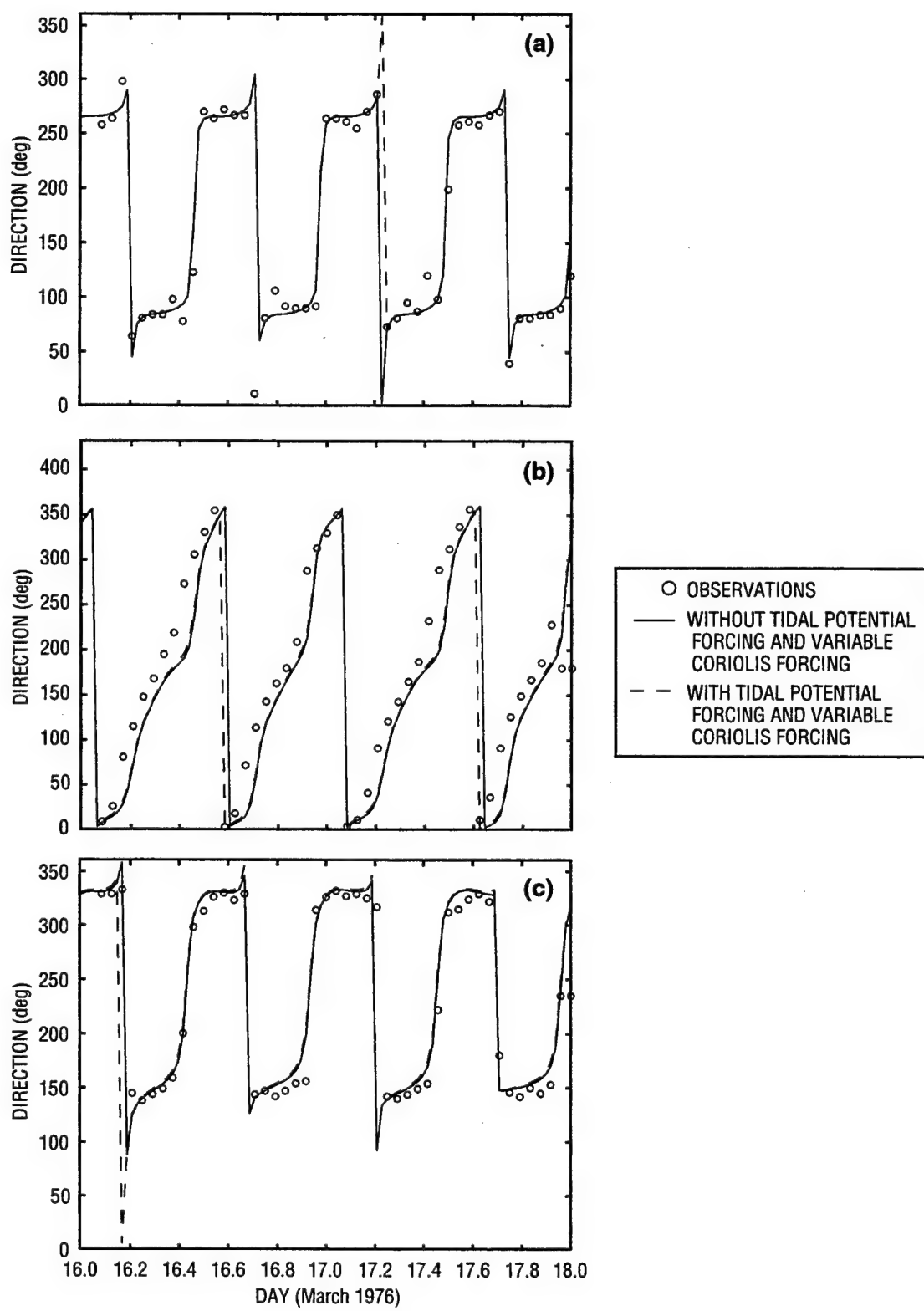


Fig. 20 — Effect of variable Coriolis forcing, velocity gauges (a) 2, (b) 7, and (c) 8

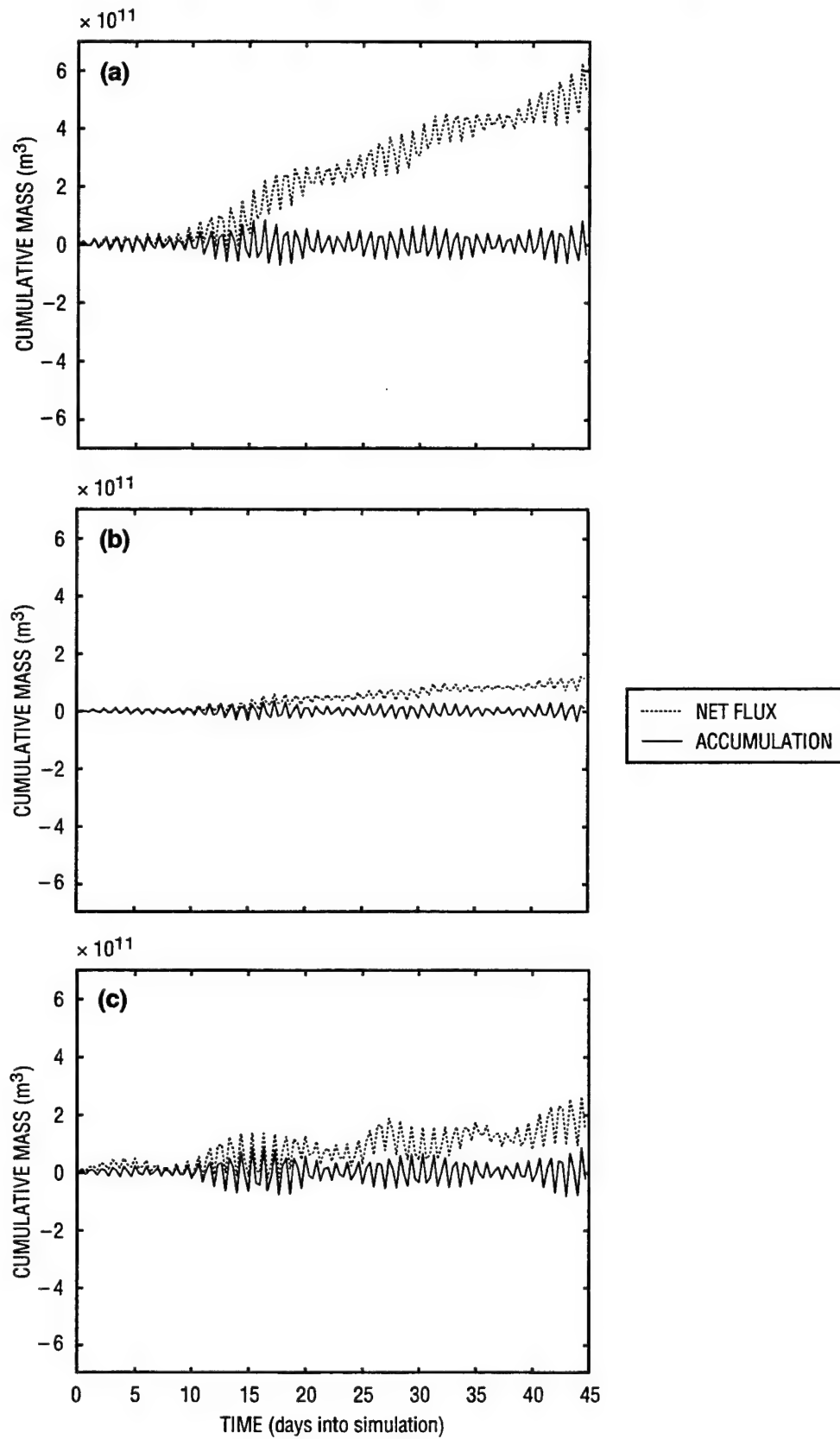


Fig. 21 — Mass balance analysis, linear models, (a) calibrated ( $\tau_0 = \text{ffactor} = 6E - 5$ ), (b) uncalibrated ( $\tau_0 = 6E - 5$ ;  $\text{ffactor} = C_f = 6E - 4$ ), and (c) fully nonlinear model

of the small difference between the model parameters  $\tau_o$  and FFACTOR, the linear friction coefficient, or whether it is merely due to the weaker tidal response caused by the higher frictional coefficient. Mass balance is significantly improved when using a nonlinear bottom stress representation (Fig. 21c) as compared to the model simulations with calibrated linear bottom friction (Fig. 21a). For all the simulations, water volume changes are found to be reasonable while the mass flux is consistently in error.

Checks of mass conservation are also conducted for three subsections of the grid: the English Channel constriction, a region along the French coast, and the western open boundary (see Fig. 22a–c). For the French coastal section and the English Channel constriction, mass conservation computations mimic those produced for the entire grid. The mass flux into the domain remains high, skewing mass balance for the computed solution. As expected, Fig. 22c shows large mass balance errors occur at the open boundary. Contrary to the interior locations in the domain, the mass flux out of this region is greater than the volume of mass lost.

The mass conservation properties of the GWCE equation continue to be the subject of current research, e.g., Lynch and Holboke (1997), Westerink et al. (1994b).

#### 6.4.2 Time-Step Size

Time-step size selection is based only on considerations of stability through the computation of an acceptable Courant number (Lapidus and Pinder 1982). For example, a timestep appropriate to the original TFF coarse grid is determined as:

$$\Delta t < 300s = \frac{1.5 \Delta x_{min}}{\sqrt{gh_{max}}} = \frac{1.5 (9 \text{ km})}{\sqrt{9.81 (\text{m/s}^2) (110 \text{ m})}}. \quad (6.3)$$

A Courant number of 1.5 is suggested by Westerink et al. (1992b), though experience suggests that values less than 1.0 are optimal. Experiments using a variety of timesteps demonstrate that as long as the stability criterion is met, time-step size has no observed influence on model computations.

#### 6.4.3 Lateral Eddy Viscosity

A sensitivity analysis on the lateral mixing term is performed by selecting eddy viscosity coefficient values in the range from 0 to 100 m<sup>2</sup>/s, three orders of magnitude. No significant effect of the lateral eddy viscosity on model-computed tides is observed. The horizontal mixing terms can be expected to play a more important role when the environment is advection dominated or small-scale, nearshore flows are considered.

#### 6.4.4 Minimum Depth

All model simulations to this point have not included a mechanism for shoreline inundation. For these simulations, it is determined that a minimum depth of approximately 8 m is required when nonlinear finite amplitude terms are included in the model formulation. The use of smaller minimum depths (e.g., 6.0 m) results in negative depths indicative of drying of the grid elements. Because no “standard” minimum depth is suggested by the TFF organizers, a value of  $H_o = 10$  m is specified in all non-wetting/drying simulations, including those simulations that do not involve nonlinear finite amplitude terms for the sake of consistency.

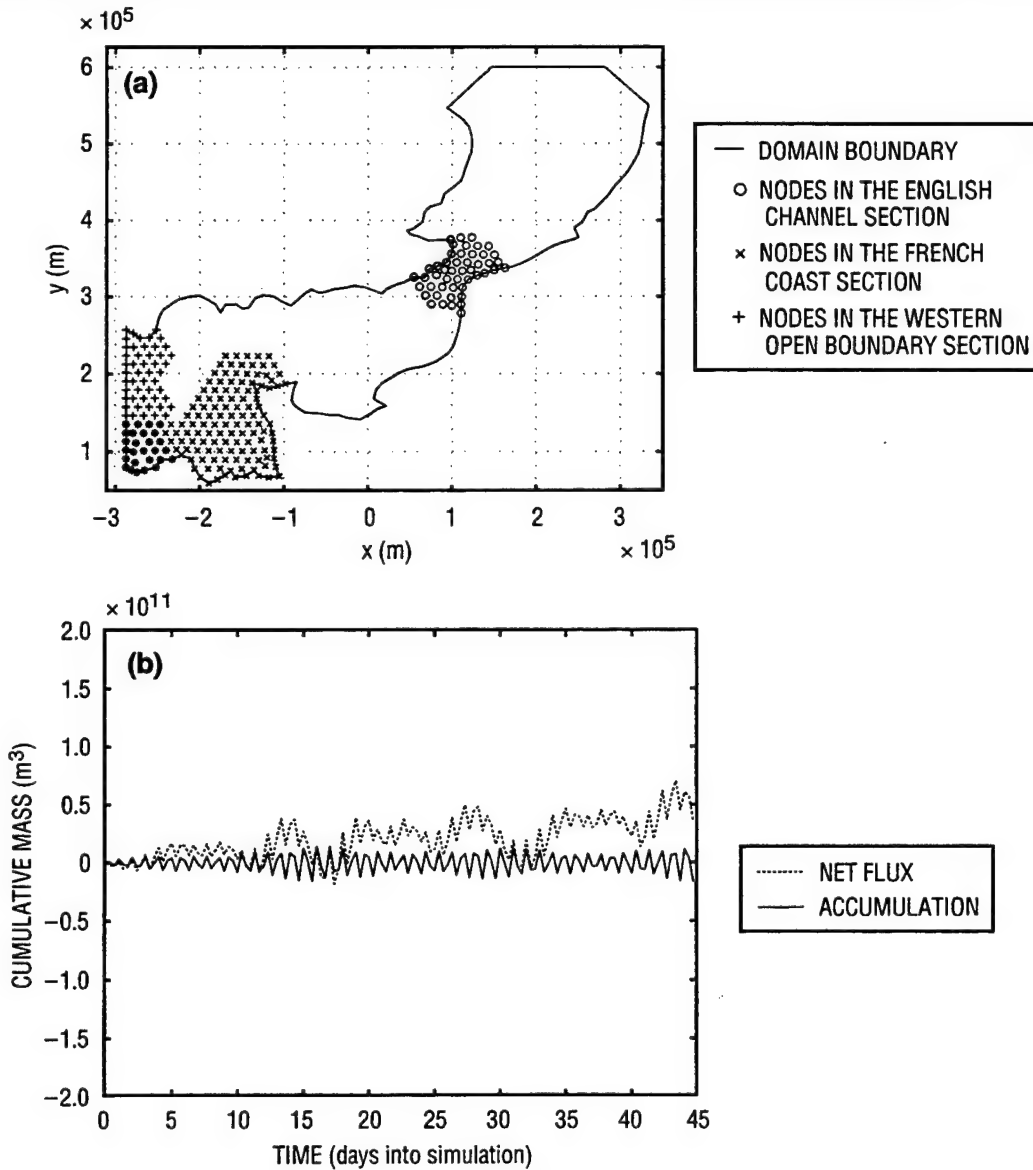


Fig. 22 — (a) Subgrid sections used in mass balance analysis; mass balance analysis fully nonlinear models and (b) English Channel constriction

For those model simulations that employ a shoreline inundation mechanism, the specification of a minimum depth is not necessary.

## 6.5 Implementation of Wetting and Drying

Within ADCIRC-2DDI, shoreline inundation is handled through a numerical wetting and drying procedure in which mesh elements can become active or inactive throughout the duration of the simulation. This wetting and drying feature in ADCIRC-2DDI is implemented successfully for the North Sea/English Channel study case. Allowing the wetting and drying of elements makes possible the inclusion of nonlinear finite amplitude terms without imposing a large minimum depth.

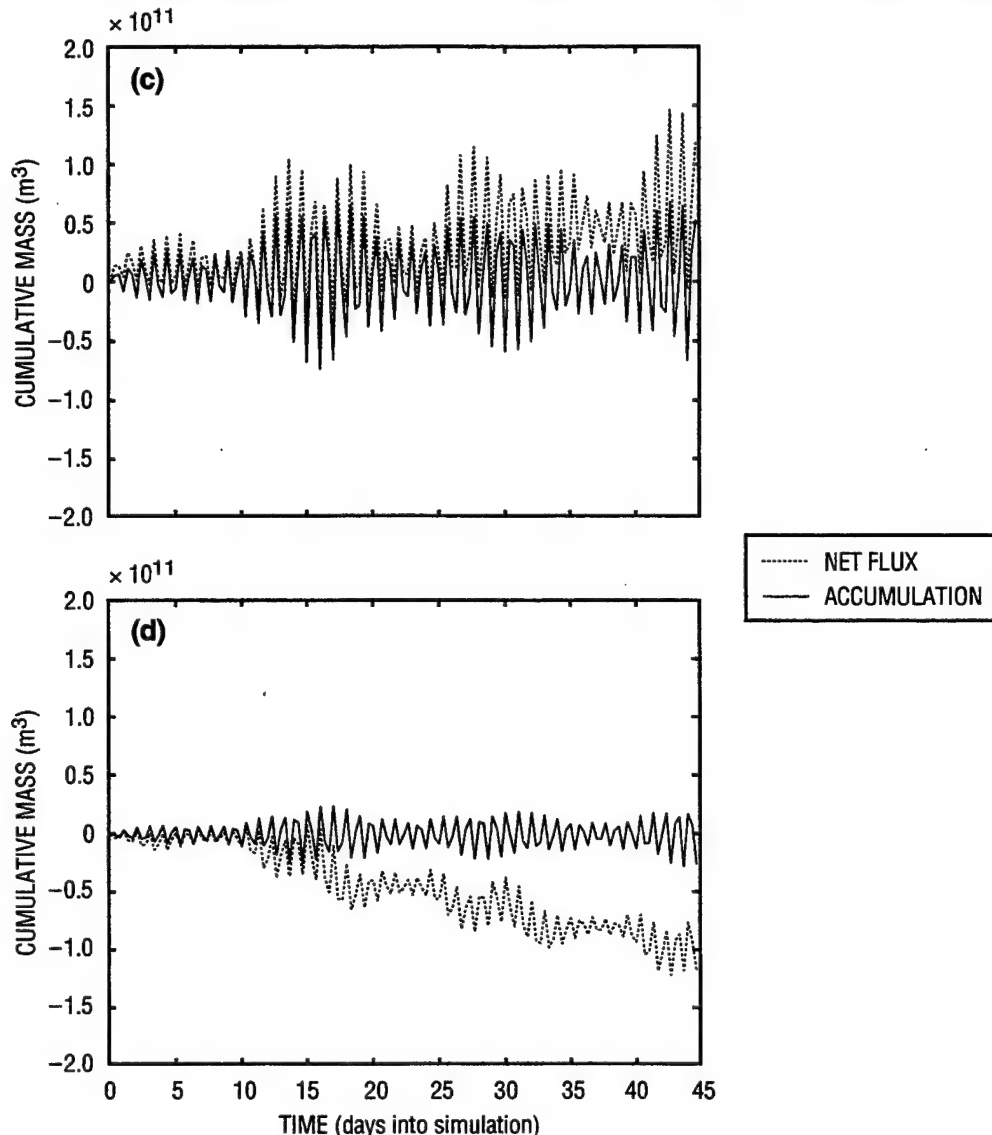


Fig. 22 — (cont.) (c) French coast and (d) western open boundary

During model simulations of the North Sea/English Channel when the wetting and drying feature is implemented, drying occurs at many of the 11 coastal elevation gauge locations preventing any model-data comparisons based on elevation. A notable observation is that drying occurs at coastal nodes with relatively large bathymetric depths (e.g., 8 m below mean sea level) with an indication that this drying is due to land-locking. Based on the location of such a node in Fig. 23, land-locking seems unrealistic.

Mass conservation improves when wetting and drying is active as indicated by the global mass flux and mass accumulation curves shown in Fig. 24a and b. The reason for this improvement is related to the elimination of a minimum depth constraint that serves as a source of mass to the system. Furthermore, when using the wetting/drying feature, alterations made to the numerical solution procedure may contribute toward improved mass conservation.

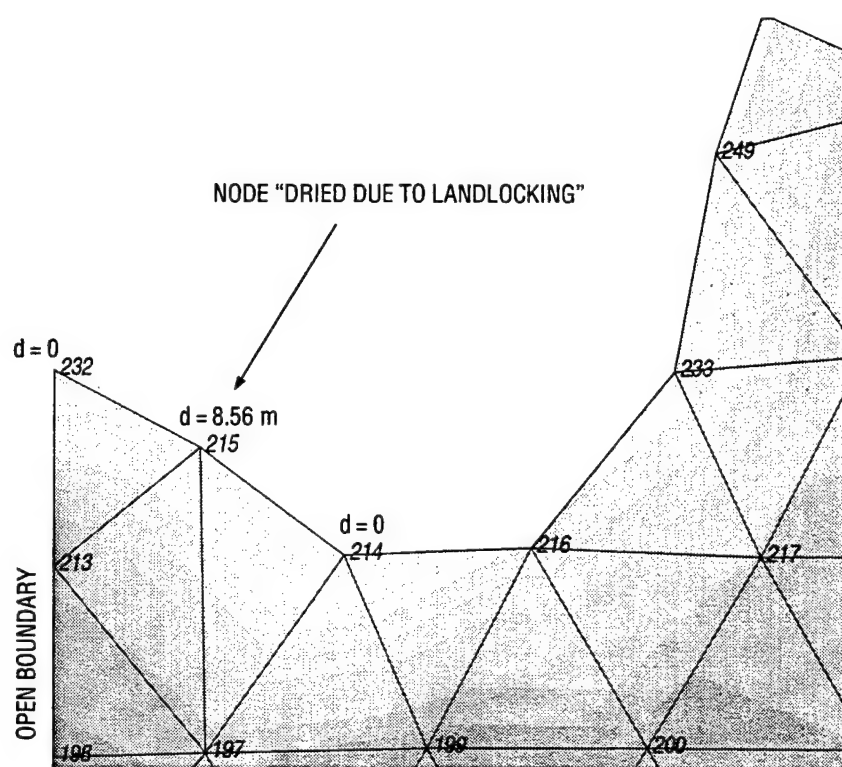


Fig. 23 — A suspect example of ADCIRC's wetting and drying routine

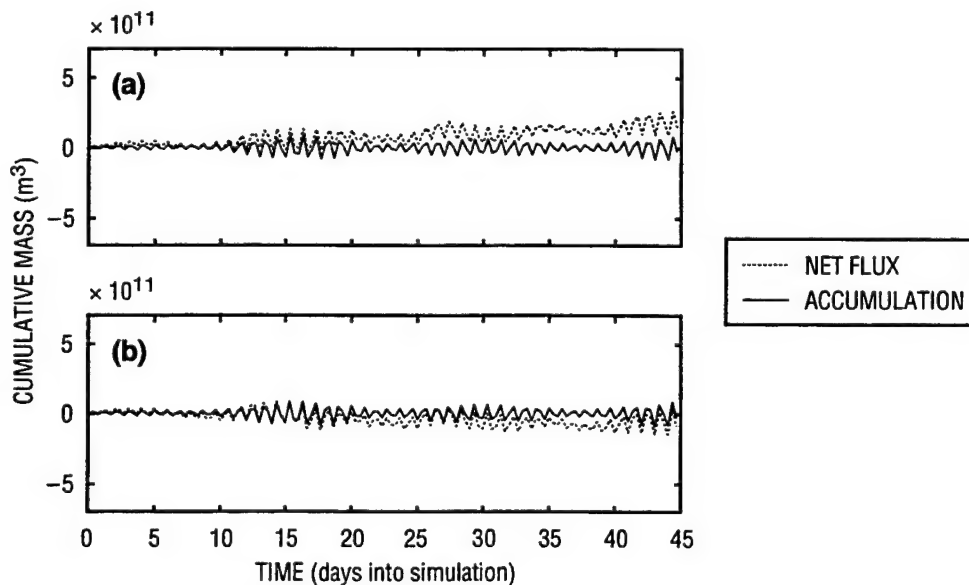


Fig. 24 — Mass balance analysis, fully nonlinear model, wetting and drying, (a) without and (b) with

Wetting and drying is a very recent feature of ADCIRC-2DDI, and by the admission of its developers, is largely untested with needed improvements acknowledged. The option of element wetting and drying does offer possibilities for additional realism and further model stability, which in turn permits the inclusion of all model nonlinearities in simulations using ADCIRC-2DDI.

It should be noted that implementation of the wetting and drying feature does not require specification of a special land boundary type, such as a weir boundary. Specification of this type of land boundary is only necessary when representing structures such as alongshore dikes or seawalls.

## 7.0 MESH RESOLUTION ISSUES

Mesh resolution resulting from the placement of discrete nodes throughout the domain cannot be entirely separated from the model-computed response. Valuable insight into an appropriate grid resolution for a given problem is gained by considering the scale of the physical processes being modeled; in this case, the physical scales are associated with tidal-induced circulation. Generally and specifically in the English Channel/North Sea, tidal forcing produces very long waves (e.g., semidiurnal tides are  $O(1000 \text{ km})$ ) that are readily resolved by a relatively coarse mesh having nodal spacing of  $\sim 10 \text{ km}$ . However, irregular land boundaries whose variability occurs at smaller spatial scales,  $O(\text{less than } 10 \text{ km})$ , induce large velocity gradients. Proper computation of the tidal circulation in these circumstances requires significantly more mesh refinement than is needed to predict sea surface height.

Mesh resolution also directly influences truncation errors associated with the discrete equations that can lead to degradation of the computed solution (i.e., Westerink et al. 1994c; Hagen and Westerink 1995, 1996; Westerink and Roache 1996). The effects of resolution on both the computed physics and the numerical approximation is determined through a grid convergence study (e.g., Dietrich et al. 1990; Lardner and Song 1992; Blain et al. 1998). As a minimum, grid convergence studies compare solutions computed over two meshes of different resolution. If the modeled physics are not adequately resolved over a coarse grid, the computed coarse grid solution will differ significantly from the fine grid result. An infinite degree of resolution will remove inadequacies due to mesh refinement, but this approach is clearly not practical. A practical objective is to select a resolution that captures the physics adequately and is computationally efficient. Figure 25 illustrates this motivation for a grid convergence study.

### 7.1 Computation of Grid Errors

Model simulations over the North Sea/English Channel are conducted for three discrete meshes with varying levels of nodal point resolution. The three grids are referred to as: G9 with nodal spacing ranging from 9–15 km, G4 with nodal spacing ranging from 4–8 km, and G2 with nodal spacing ranging from 2–4 km. Properties of these grids are described further in Table 7. Also included is an indication of the typical computation time for a 45-d simulation on a Sun UltraSparc workstation.

Figure 26a and b contains times series plots at two locations near the coast of the Cherbourg peninsula shown in Fig. 27 for simulations using the grids G4 and G9; note that grid G4 is simply a double refinement of grid G9. At two locations, node 192 and node 1605, elevation differences are typically large when checked against other locations in the domain. Overprediction at one node together with the corresponding underprediction at a nearby node is thought to be due to increased velocity gradients in that area. Figure 28 depicts notable changes in the velocity magnitude computed

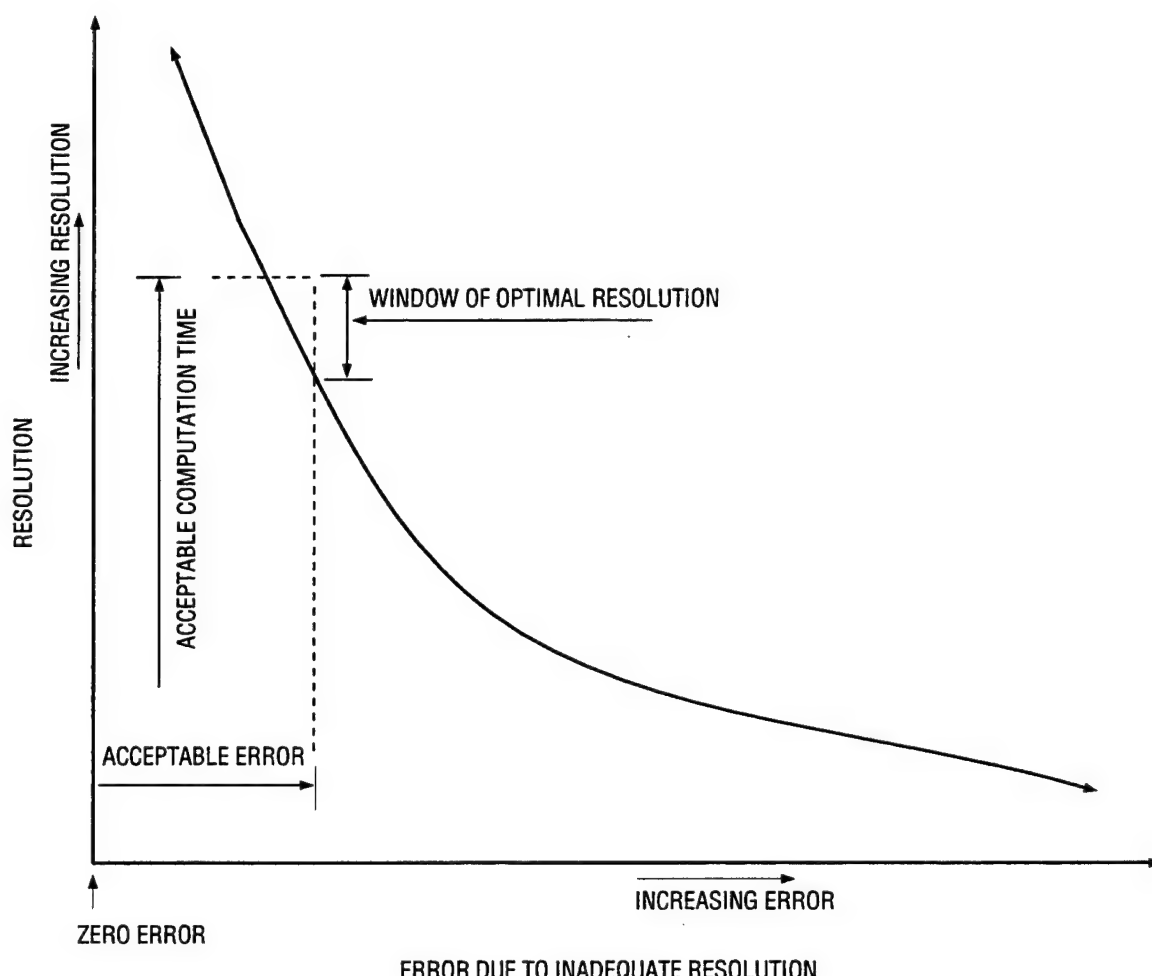


Fig. 25 — Optimization of grid resolution

Table 7 — Properties of Computational Grids for the North Sea/English Channel

GRID	NODAL SPACING (km)	NUMBER OF NODES	NUMBER OF ELEMENTS	CPU FOR 45-d SIMULATION (h)
G9	9-15	911	1613	0.7
G4	4-8	3434	6452	3.5
G2	2-4	13319	25808	35.3

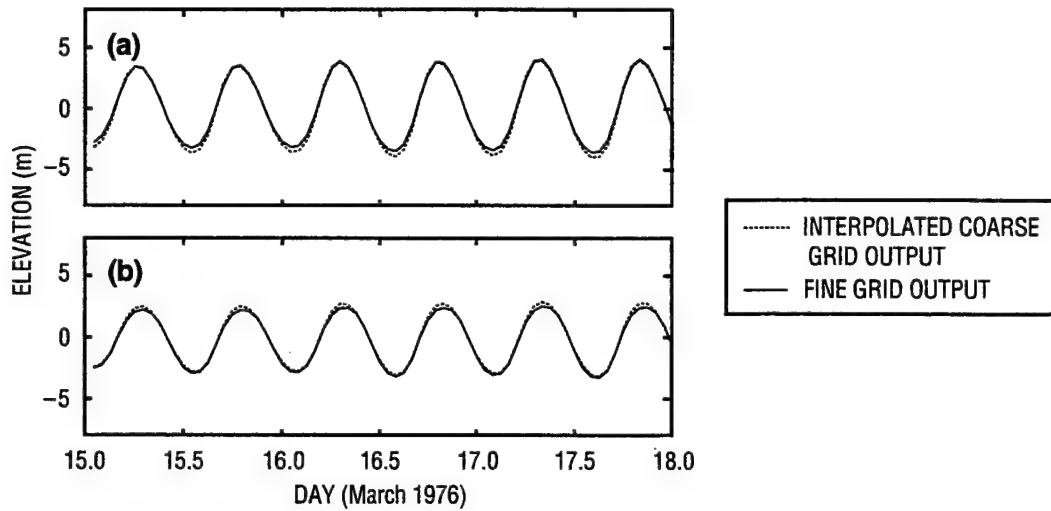


Fig. 26 — Elevation time series near Cherbourg, (a) node 192 and (b) node 1605

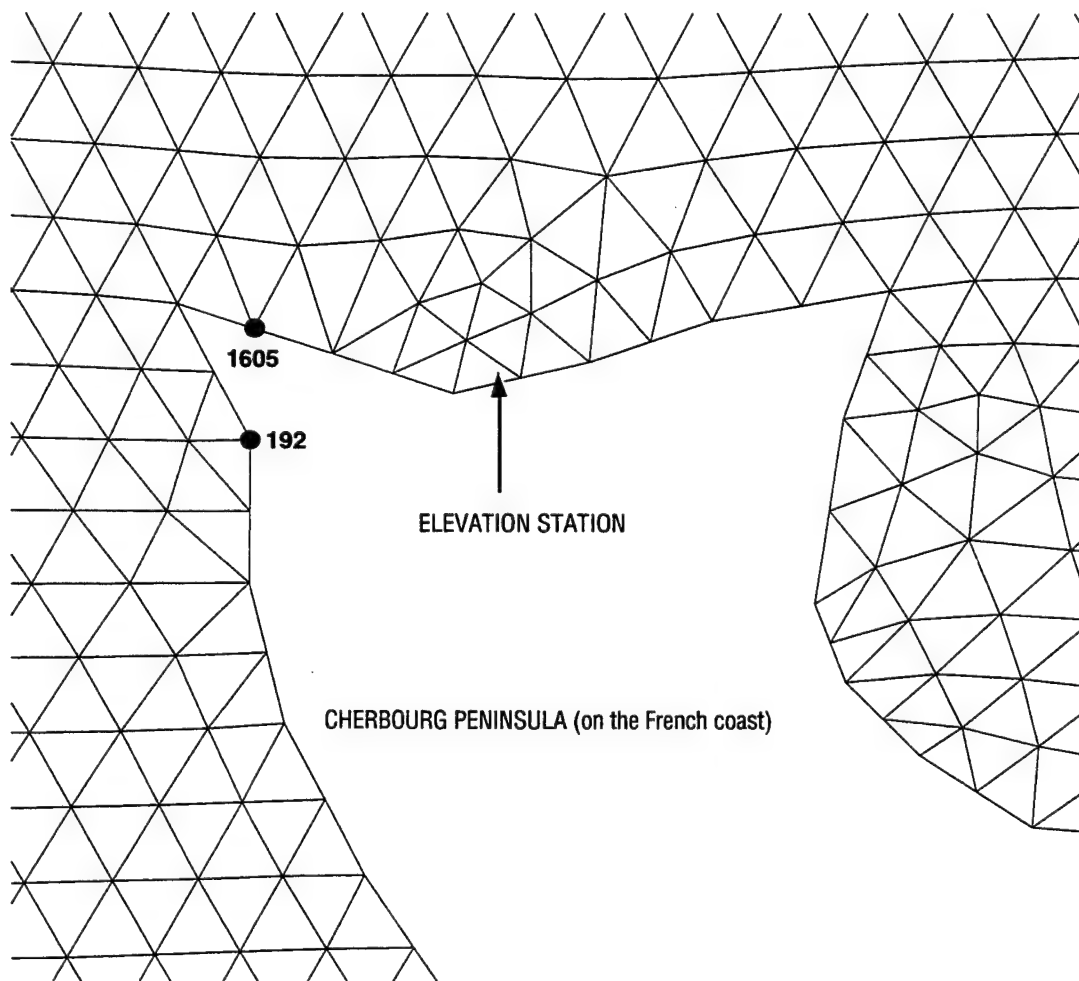


Fig. 27 — Cherbourg Peninsula, shown with FE grid

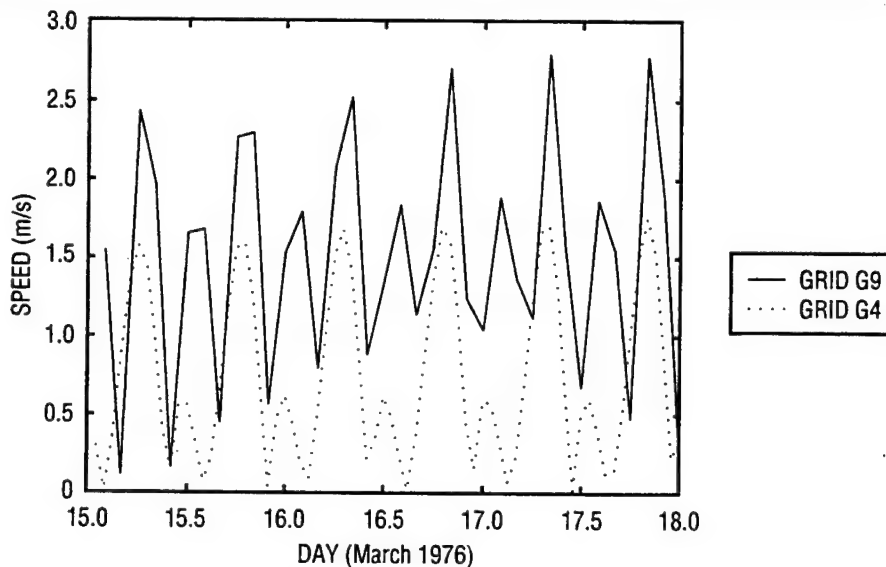


Fig. 28—Speed comparisons at node 192

over grids G9 and G4 at node 192. Differences in the computed circulation patterns are likely due to changes in spatial bathymetry gradients that are a direct consequence of the differing mesh resolutions.

Elevation time series at node 192 are reconstructed using several combinations of tidal constituents as computed over grids G9 and G4. Comparisons of these time series are shown in Fig. 29a-e for fully nonlinear simulations. Note that the coarse grid results have been interpolated onto the fine grid to facilitate difference computations. Tidal amplitudes based on either all 11 TFF constituents (Fig. 29a) or the six astronomical TFF constituents (Fig. 29b) are larger when computed over the coarser mesh. Figure 27c shows notable differences in computation of the five TFF nonlinear tides over the two meshes. The inclusion of 56 tidal constituents (which approximates the raw model solution) in the time series reconstruction (Fig. 29d) results in deeper troughs of the tidal signal over the coarse grid. Dynamics at the trough of a tidal wave are such that current speeds increase due to a reduced water depth at the trough. Higher velocity magnitudes and sharp velocity gradients near the trough may not be well represented over the coarse mesh and could, in fact, lead to degradation of the velocity solution. For the tidal signal reconstruction based on the 45 non-TFF constituents (Fig. 29e), elevations are consistently less, using the coarse grid solution as compared to the fine grid solution. Differences between model solutions over each grid are thought to be primarily caused by alterations in the circulation pattern due to bathymetry deviations at different resolutions.

Domain-wide tidal elevations computed over the coarse grid, G9, are now compared to domain-wide elevations computed over the fine mesh grid, G4, producing difference errors between the two mesh solutions. Figure 30a and b present histograms of elevation differences between each pair of grid simulations, i.e., G4 and G9, G2 and G4, and represent a composite for the entire domain. The average difference between the grid G9 and G4 solutions is relatively small, approximately 1.4 cm, and errors are spread in a Gaussian-like distribution over errors ranging to  $\pm 0.05$  m. In contrast, elevations computed using grids G4 and G2 exhibit much more similarity than comparisons between solutions over grids G9 to G4. In Fig. 30b, the average magnitude of elevation differences between solutions computed over grids G4 and G2 is 0.4 cm, a considerable reduction

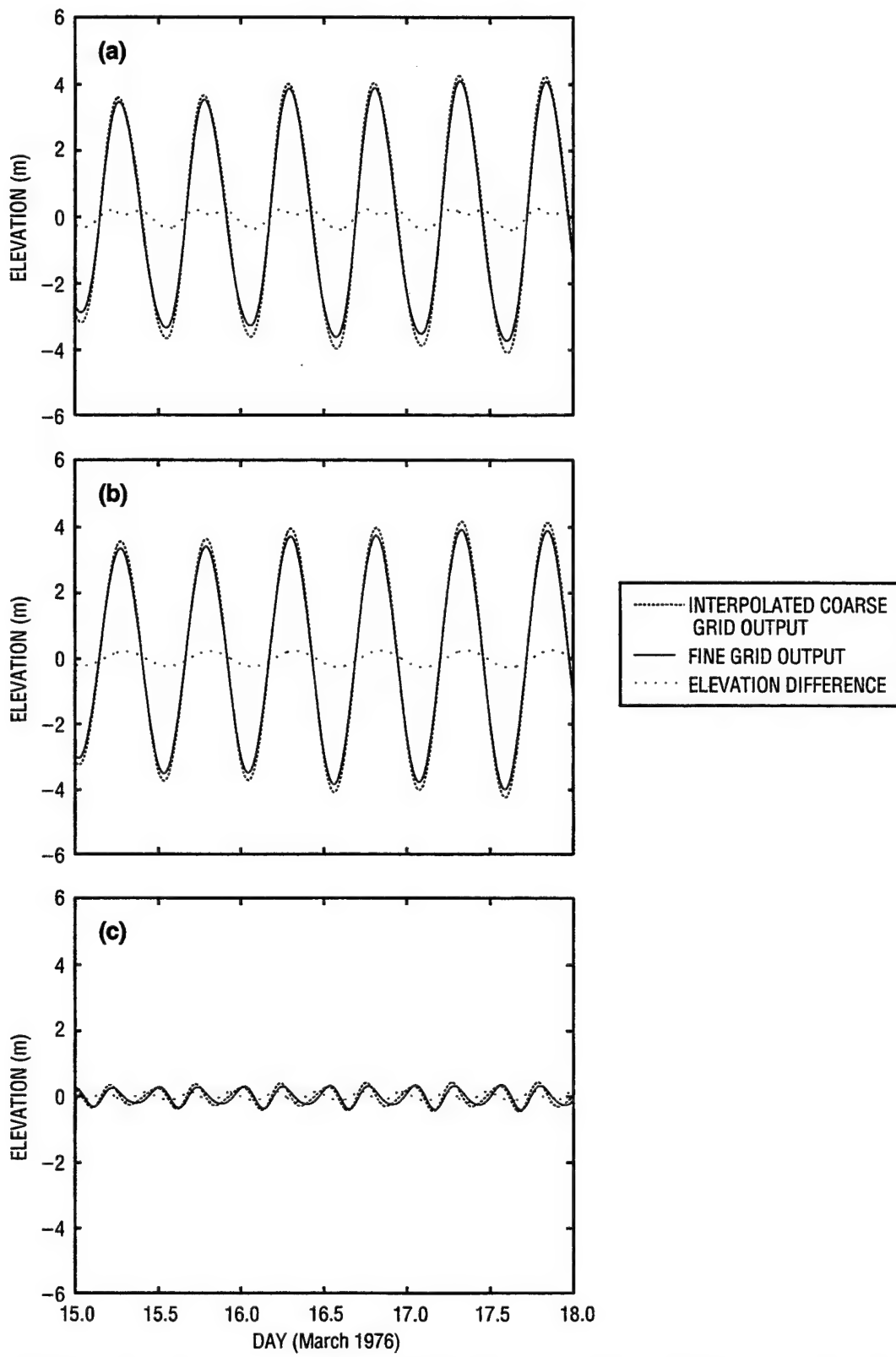


Fig. 29 — Tidal elevations at node 192, (a) 11 TFF constituents only, (b) six astronomical TFF constituents only, and (c) five nonlinear TFF constituents only

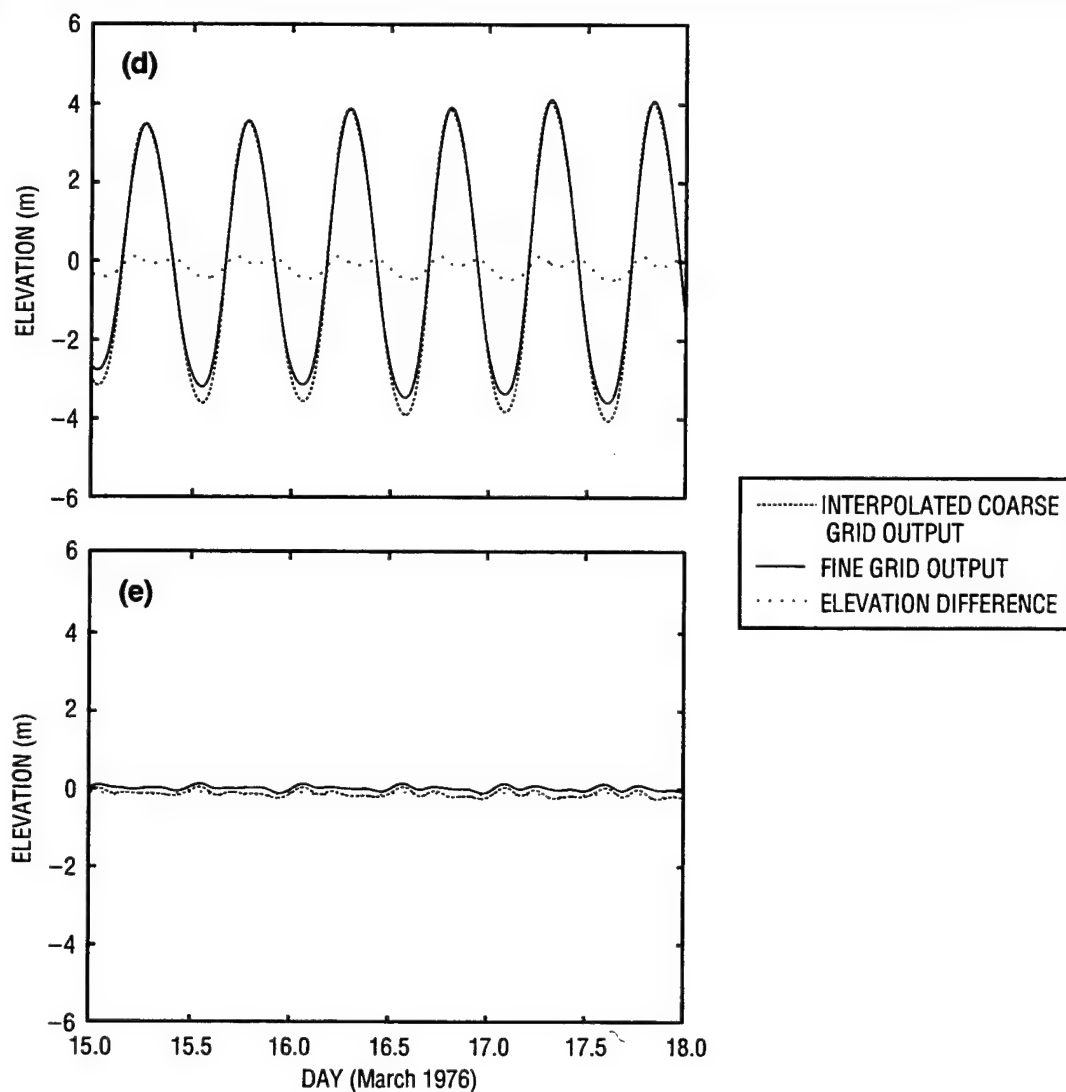


Fig. 29 — (cont.) (d) 56 constituents and (e) 45 non-TFF constituents only

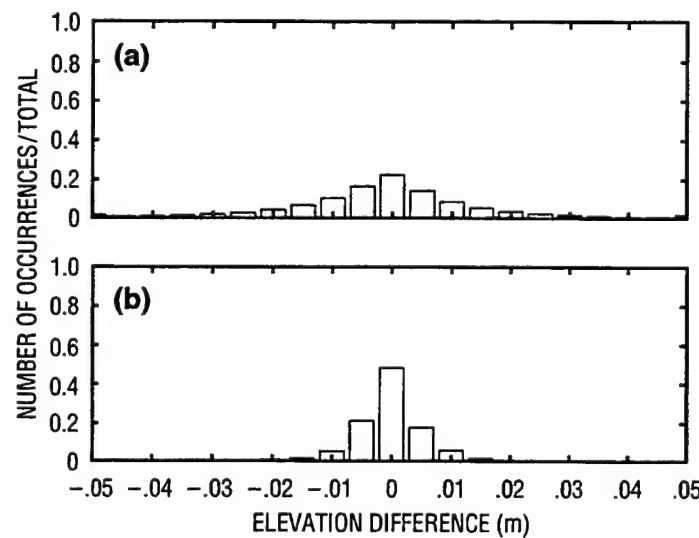


Fig. 30 — Grid error histograms, simulations with nonlinear bottom friction and nonlinear finite amplitude terms, (a) G4 and G9 and (b) G2 and G4

over the 1.4 cm average for the G9 to G4 comparison. Furthermore, nearly the entire distribution of error is within  $\pm 0.01$  m. Resolution effects are quickly reduced as refinement increases, indicating that the computed model solution is rapidly converging toward the asymptotic solution, which would result for infinite grid resolution. Westerink and Roache (1996) suggest a test to determine whether a grid falls within the asymptotic range using a Richardson-based error estimator for the fine and coarse grid solutions.

A Richardson-based error measure derives an error estimate for model solutions computed over both a coarse and fine mesh (see Blain et al. 1998 for implementation). For the coarse mesh, the Richardson-based error estimate is cast as  $E^C$  and for the fine mesh, the error is represented as  $E^F$ . Expressions for these errors are derived by Roache (1994) and presented below for this application in which the fine grid is obtained by doubling the mesh refinement of the coarse grid and the spatial discretization of the discrete model equations is second order:

$$E^C = \frac{4}{3} \epsilon_{max} \quad (6.4)$$

$$E^F = \frac{1}{3} \epsilon_{max}. \quad (6.5)$$

Note that  $\epsilon_{max}$  is the maximum elevation difference between the coarse and fine grid solutions at a specified instant in time. Normalized error estimates  $E^{C/n}$ ,  $E^{F/n}$  are obtained by dividing the error estimates of Eqs. (6.4) and (6.5) by the maximum elevation over the domain during the time interval of interest.

To determine if a grid lies in the asymptotic range, a simple comparison between fine and coarse grid error estimates,  $E^C$ ,  $E^F$  for that grid is made. If  $E^C$  and  $E^F$  for that grid yield similar magnitudes, then the grid is assumed to lie in the asymptotic range. Figure 31a and b shows results from these comparisons for two simulations, both using a nonlinear bottom friction parameterization and one including the finite amplitude terms. Slight differences between  $E^C$  and  $E^F$  indicate that G4 does not lie in the asymptotic range. However, these differences are not great, suggesting that G4 is near the asymptotic range. Based upon this observation, it is entirely possible that the grid G2 does lie within the asymptotic range indicating formal convergence of the tidal solution. Note that the addition of finite amplitude nonlinearities results in a periodic semidiurnal spike in the overprediction error.

## 7.2 Sensitivity of Nonlinearities to Mesh Resolution

Richardson error estimates are also used to examine the relation between mesh resolution, the inclusion of various nonlinear terms, and the model-computed tidal solution. In comparing tidal elevation predictions derived from simulations that include or exclude the finite amplitude terms, Fig. 32a and b respectively, finite amplitude terms appear to increase the overprediction of elevation as noted previously, suggesting that finer resolution is required to adequately capture the added complexity and nonlinearity associated with these terms. This is not a surprising result, since the finite amplitude contribution is based on sea surface gradients that inherently require two points for computation. The increased overprediction may also be due to a greater sensitivity of the nonlinear dynamics to bathymetry. Resolving changes in the bathymetry gradient requires higher nodal densities, increasing mesh resolution.

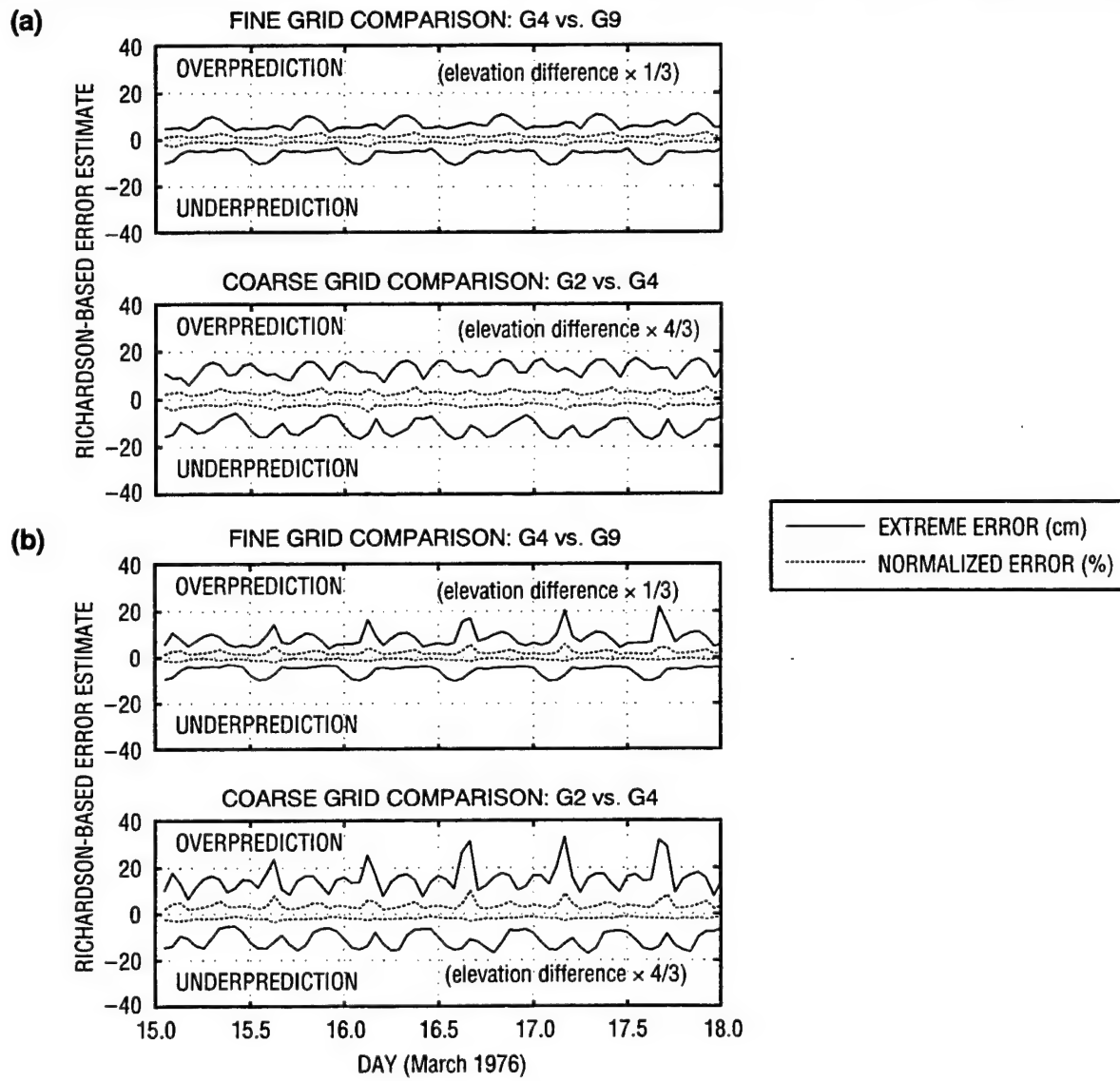


Fig. 31 — Grid comparison simulations, (a) nonlinear bottom only and (b) nonlinear bottom friction and nonlinear finite amplitude terms

In a further comparison, Richardson-based error estimates for grid G9 for tidal solutions that have either the convective acceleration terms (space derivatives) active or inactive are displayed in Fig. 32a and b. Inclusion of the convective terms not only leads to additional peaks in the overprediction error curve in time, but the underprediction of elevation is also enhanced. Again, finer grid resolution is necessary to adequately capture contributions from nonlinear advective interactions of the tide, though the specific cause of the underprediction is uncertain. Using the finest grid, G2, the inclusion of convective acceleration terms (space derivatives) leads to model instability. One shortcoming of the ADCIRC-2DDI model in its current state is the spatial discretization of the convective terms, coupled with an explicit treatment in time of nonlinearities associated with these terms. This aspect of the model is currently under investigation with improvements expected in subsequent versions of the code (greater than v31\_06). Note that normalized errors for all cases are relatively small and uniform throughout the simulation period. Though errors are not completely eliminated, the goal of minimizing errors associated with the mesh resolution is achieved.

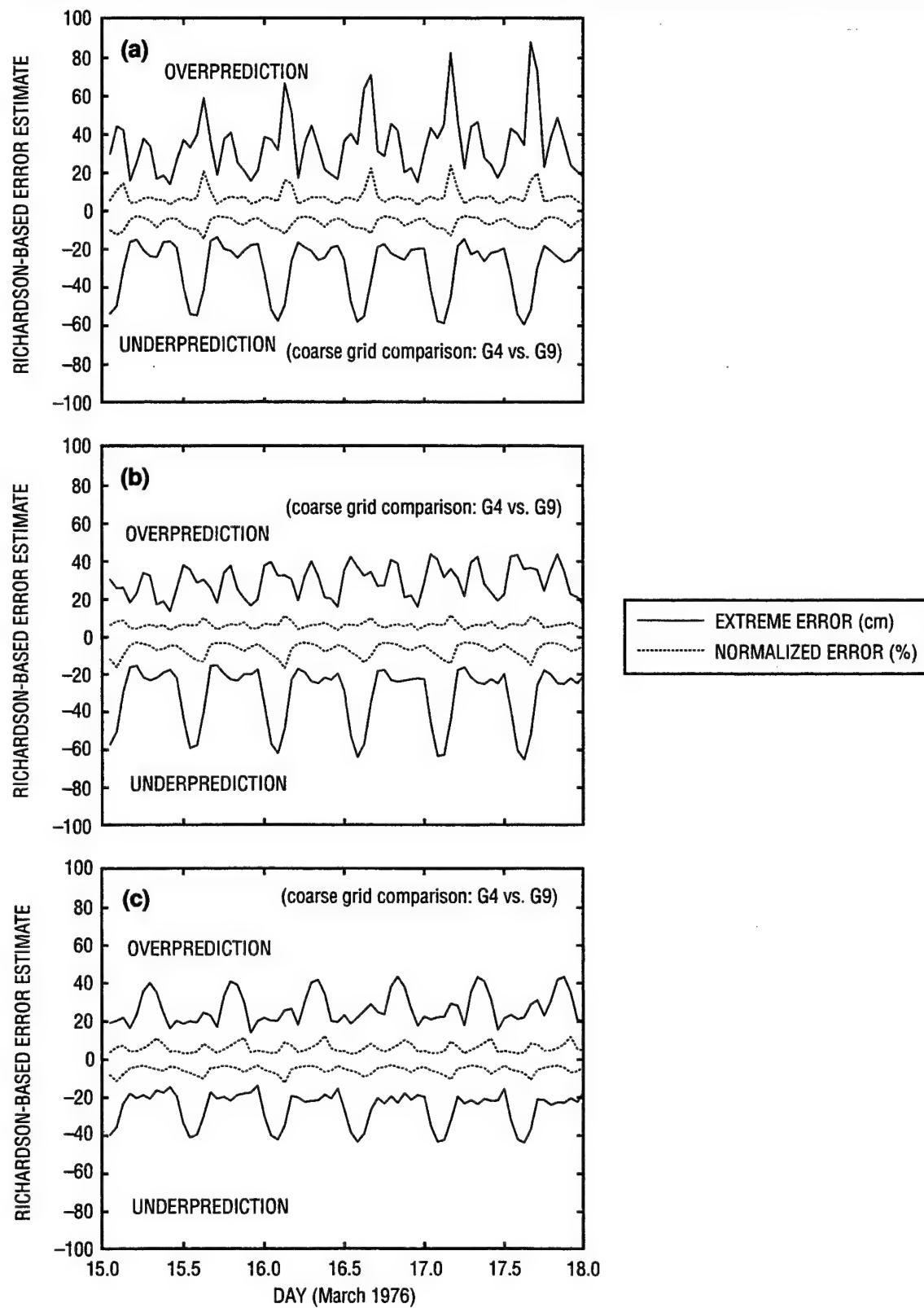


Fig. 32 — Richardson-based error simulations, (a) fully nonlinear, (b) nonlinear bottom friction/nonlinear convective acceleration terms, and (c) nonlinear bottom friction only

The resolution requirements for tidal elevations in the North Sea/English Channel as determined from this grid convergence study indicate that nonlinear dynamics in the shallow water is important and requires significantly more spatial resolution. Tidal computations are highly sensitive to bathymetric changes and coastline geometry that occur at small spatial scales. For the meshes implemented, even though grid G4 (whose resolution ranges from 4–8 km) is not within the asymptotic range, it does seem to adequately capture smaller scale tidal phenomena. Concurrently, the mesh does not require excessive computer resources. For any study of tidal dynamics, it is extremely important to conduct a grid convergence check to minimize influences of the spatial discretization on the computed solution.

## 8.0 CONCLUSIONS

There is a movement in recent times toward the application of coastal ocean models that employ FE modeling techniques. Significant advantages are associated with the FE discrete form of the governing equations. The most obvious of these advantages is the tremendous grid flexibility afforded by FEs. Variable mesh resolution permits mesh refinement in specified regions to resolve sharp gradients in flow or bathymetric features and to capture the tortuous detail of the shoreline. At the same time, coarse mesh spacing remains in deeper waters where changes in the ocean dynamics are known to occur more slowly or on larger scales.

An in-depth examination of the ADCIRC-2DDI FE, hydrodynamic model and its application to tidal prediction in coastal regions is the focus of this report. An overview of the basic premise of FE approximations and the mathematical development of the FE equations implemented within the ADCIRC model are presented. Utilization of the ADCIRC-2DDI model in no way requires a complete understanding of the mathematical foundation of the FE equation development. Rather, the user is required to understand the relationship between the model assumptions, mesh resolution, domain, boundary forcing, and the model-computed fields to adequately assess the computed tidal predictions.

Using the TFF benchmark case, the ADCIRC-2DDI model is validated in the simulation of both tidal elevations and currents. Agreement of the “base simulation” elevation time series with observations is excellent at 10 of the 11 coastal elevation gauge locations. ADCIRC-2DDI has demonstrated accurate prediction of the tidal elevations at these 11 coastal stations (during a particular 25-h time period) that is superior to several other tidal models. However, due to the limitations of model-model comparisons using previously published results, a conclusion that ADCIRC is a better model is not warranted. As a side note, a true model-data comparison only occurs when the modeled and observed time series are composed of identical tidal frequencies. Considerable discussion in the text is devoted to this concept within the context of the North Sea/English Channel validation.

Considering the quality of data, the agreement of the velocity hindcasts is also quite good, particularly with respect to current directions. For speed comparisons, agreement is best at velocity gauges placed in a vertical location where actual speeds are expected to be similar to depth-averaged speeds.

Through harmonic analysis and recombination of model results, the 11 tidal constituents included in the TFF data are found to be inadequate for a complete representation of the actual tidal signal. From model solutions, it is clear that several additional nonlinear tides make significant contributions to the elevation in near-coastal areas where the gauges are located.

The sensitivity analyses undertaken here illuminates the influence of nonlinearities, forcing, and several model parameters on the model-computed response. Modular construction of the ADCIRC-2DDI model makes such analyses possible without requiring user modification of the code. Several conclusions and recommendations based on these analyses are made regarding the use of ADCIRC-2DDI. First, due to its physical basis and mass conservation properties, the nonlinear parameterization of bottom stress offers measurable advantages over use of a linear bottom friction formulation. Secondly, the inclusion of other nonlinear terms in the GWCE (such as the finite amplitude or convective terms) results in noticeable, though not dominant, differences in the computed model solution. Bottom friction remains the single most important mechanism affecting tidal elevations and circulation in the coastal environment. A fully nonlinear simulation in which all nonlinear terms contribute to the model dynamics offers a more complete representation of tidal physics, especially with respect to internal nonlinear tide generation.

For the North Sea/English Channel simulations, a fully nonlinear model response produces more accurate model-to-data comparisons with respect to tidal elevation. Care must be taken when exercising the model in a fully nonlinear mode to maintain an appropriately fine mesh resolution and avoid the drying of elements through a minimum depth specification if wetting/drying is inactive.

This sensitivity study confirms that nonlinear tides on the shelf can be important and should be included in tidal boundary forcing when open boundaries are located on the continental shelf. Alternatively, utilizing a larger domain locates the open boundaries in deeper water where the nonlinearities are of little consequence. For domains larger than the North Sea/English Channel region studied,  $O(1000 \text{ km} \times 1000 \text{ km})$ , tidal potential forcing and a variable Coriolis forcing will likely have a greater significance. The range of latitudes spanned by the domain strongly influence the importance of these mechanisms. In the context of the southern North Sea/English Channel case, inclusion of horizontal mixing in the form of lateral eddy viscosity is of little consequence. If the environment is advection dominated or small-scale nearshore flows are of interest, the horizontal mixing is expected to increase in importance.

Finally, a brief examination of mesh resolution effects on the computed tidal solution are undertaken in the context of a grid convergence analysis. Though grids having 9 km (G9) and 4 km (G4) as minimum nodal spacings do not fall in the asymptotic range, small differences between the Richardson-based error estimate for grid G4 suggests that a grid having a minimum resolution of 2 km (G2) is at or very near the asymptotic range. Most of the significant errors resulting from insufficient grid resolution are thought to be due to the misrepresentation of large velocity gradients induced by the irregular coastline. Model nonlinearities further magnify such errors.

The primary purpose for this study has been to assess the capability of the ADCIRC-2DDI barotropic, 2D, FE hydrodynamic model to predict tidal dynamics in coastal waters. A comprehensive series of experiments testing sensitivity of the model have provided considerable insight, not only to the application of the model itself, but also to the behavior of tides in a coastal environment. The hope is that experiences gained from this work will be carried over into future tidal applications leading to an improved predictive capability.

## 9.0 ACKNOWLEDGMENTS

We would like to thank Rick Luettich at the Institute of Marine Sciences, University of North Carolina, for use of the ADCIRC-2DDI model and for helpful discussions regarding model

implementation and performance. This work was funded by the Office of Naval Research through the NRL 6.2 Coastal Simulation project (Program Element number 0602435N).

## 10.0 REFERENCES

Al-Rabeh, A. H., N. Eunay, and H. M. Cekirge, "A Hydrodynamic Model for Wind Driven and Tidal Circulation in the Arabian Gulf," *Applied Mathematical Modelling* **14**, 410–419 (1990).

Baptista, A. M., J. J. Westerink, and P. J. Turner, "Tides in the English Channel and Southern North Sea – A Frequency Domain Analysis Using Model TEA-NL," *Adv. in Water Resources* **12**, 166–183 (1989).

Becker, E. B., G. F. Carey, and J. T. Oden, *Finite Elements, An Introduction* (Prentice Hall, NJ, 1981), Vol. 1.

Blain, C. A., J. J. Westerink, and R. A. Luettich, "Grid Convergence Studies on the Prediction of Hurricane Storm Surge," *Int. J. Num. Methods Fluids* **26**, 369–401 (1998).

Blain, C. A., J. J. Westerink, and R. A. Luettich, "The Influence of Domain Size on the Response Characteristics of a Hurricane Storm Surge Model," *J. Geophys. Res.* **99**(C9), 18,467–18,479 (1994).

Blain, C. A. and A. P. McManus, "Insights into Unstructured Mesh Generation for Coastal Ocean Applications," NRL/FR/7322--97-9671, Naval Research Laboratory, Stennis Space Center, MS, 1998.

Blain, C. A. and W. E. Rogers, "Coastal Tide Prediction Using the ADCIRC-2DDI Hydrodynamic Finite Element Model: Model Validation and Sensitivity Analyses in the Southern North Sea/English Channel," NRL/FR/7322--98-9682, Naval Research Laboratory, Stennis Space Center, MS, 1998.

Blumberg, A. F. and G. L. Mellor, "A Description of a Three-Dimensional Coastal Ocean Circulation Model," in *Three-Dimensional Coastal Ocean Models*, N. S. Heaps (ed.), AGU Press, 1987, 1–16.

Celia, M. A. and W. G. Gray, *Numerical Methods for Differential Equations, Fundamental Concepts for Scientific and Engineering Applications* (Prentice Hall, NJ, 1992).

d'Hieres, C. and C. LeProvost, "Atlas des Composants Harmoniques de la Maree dans la Manche," *Ann. Hydrogr.* **6**, 5–36 (1979).

Dietrich, D. E., P. J. Roache, and M. G. Marietta, "Convergence Studies with the Sandia Ocean Modeling System," *Int. J. Num. Meth. Fluids* **11**, 127–150 (1990).

Flather, R. A., "A Numerical Model Investigation of Tides and Diurnal-Period Continental Shelf Waves Along Vancouver Island," *J. Phys. Ocean.* **18**, 115–139 (1988).

Foreman, M. G. G., "Manual for Tidal Heights Analysis and Prediction," Institute of Ocean Sciences, Pacific Marine Science Report 77-10, Patricia Bay, Sidney, B.C., 1977.

Foreman, M. G. G., "An Analysis of the Wave Equation Model for Finite Element Tidal Comparisons," *J. Comput. Phys.* **52**, 290–312 (1983).

Foreman, M. G. G., "A Comparison of Tidal Models for the Southwest Coast of Vancouver Island," Proceedings of the VII International Conference on Computational Methods in Water Resources, Cambridge, MA, Elsevier, 1988.

Foreman, M. G. G. and R. F. Henry, "A Finite Element Model for Tides and Resonance Along the North Coast of British Columbia," *J. Geophys. Res.* **98**(C2), 2509–2531 (1993).

Godin, G. *The Analysis of Tides* (Liverpool University Press, 1972).

Gray, W. G., "Some Inadequacies of Finite Element Models as Simulators of Two-Dimensional Circulation," *Adv. in Water Resources* **5**, 171–177 (1982).

Gray, W. G., J. Drolet, and I. P. E. Kinnmark, "A Simulation of Tidal Flow in the Southern Part of the North Sea and the English Channel," *Adv. Water Resources* **10**, 131–137 (1987).

Gray, W. G., "A Finite Element Study of Tidal Flow Data for the North Sea and English Channel," *Adv. in Water Resources* **12**, 143–154 (1989).

Gray, W. G. and I. P. E. Kinnmark, "QUIET: A Reduced Noise Finite Element Model for Tidal Circulation," *Adv. Engineering Software* **5**(3), 130–136 (1983).

Gray, W. G., T. Leijnse, R. L. Kolar, and C. A. Blain, *Mathematical Tools for Changing Scales in the Analysis of Physical Systems* (CRC Press, Ann Arbor, MI, 1993).

Hagen, S. C. and J. J. Westerink, "Finite Element Grid Resolution Based on Second- and Fourth-Order Truncation Error Analysis," Second International Conference on Computer Modelling of Seas and Coastal Regions, Computational Mechanics, The UK, 283–290, 1995.

Hagen, S. C. and J. J. Westerink, "Utilizing an Imposed Multiple of Change in Finite Element Grid Generation," Proc. of the Third Asian-Pacific Conference on Computational Mechanics, Chang-Koon Choi (ed.), 1817–1822, 1996.

Heath, R. E., B. H. Johnson, and K. W. Kim, "Grid-Induced Errors in Depth Averaged Flow Fields," Proc. of the ASCE Hydraulics Division Specialty Conf., San Diego, CA, ASCE, 1990.

Hendershott, M. C., "Long Waves and Ocean Tides," *Evolution of Physical Oceanography*, B. A. Warren and C. Wunsch (eds.), (MIT Press, Cambridge, MA, 1981), pp. 292–341.

Jamart, B. M. and J. Ozer, "Some Results and Comments on the Tidal Flow Forum Exercise," *Adv. Water Resources* **12**, 211–220 (1989).

Kincaid, B. and W. Cheney, *Numerical Analysis, Mathematics of Scientific Computing* (Brooks/Cole Pub. Co., CA, 1991).

Kinnmark, I. P. E., "The Shallow Water Wave Equations: Formulation, Analysis and Application," Ph.D. dissertation, Department of Civil Engineering, Princeton University, 1984.

Kinnmark, I. P. E. and W. G. Gray, "A Two-Dimensional Analysis of the Wave Equation Model for the Finite Element Tidal Computations," *Int. J. Num. Methods* **20**, 369–383 (1984).

Kinnmark, I. P. E. and W. G. Gray, "Stability and Accuracy of Spatial Approximations for Wave Equation Tidal Models," *J. Comp. Phys.* **60**, 447–466 (1985).

Kolar, R. L., "Environmental Conservation Laws: Formulation, Numerical Solution, and Application," Ph. D. dissertation, Department of Civil Engineering, University of Notre Dame, 1992.

Kolar, R. L., W. G. Gray, J. J. Westerink, and R. A. Luettich, "Shallow Water Modeling in Spherical Coordinates: Equation Formulation, Numerical Implementation, and Application," *J. Hydraul. Res.* **32**, 3–24 (1994a).

Kolar, R. L., J. J. Westerink, M. E. Cantekin, and C. A. Blain, "Aspects of Nonlinear Simulations Using Shallow Water Models Based on the Wave-Continuity Equation," *Computers and Fluids* **23**, 523–538 (1994b).

Lardner, R. W. and Y. Song, "A Comparison of Spatial Grids for Numerical Modelling of Flows in Near-Coastal Seas," *Int. J. Num. Meth. Fluids* **14**, 109–114 (1992).

Lapidus, L. and G. F. Pinder, *Numerical Solution of Partial Differential Equations in Science and Engineering* (John Wiley and Sons, New York, NY, 1982).

Le Mehaute, B., *An Introduction to Hydrodynamics and Water Waves* (Springer-Verlag, New York, NY, 1976).

LeProvost, C. and P. Vincent, "Some Tests of Precision for a Finite Element Model of Ocean Tides," *J. Comput. Phys.* **65**, 273–291 (1986).

Lee, J. K. and D. C. Froehlich, "Review of Literature on the Finite-Element Solution of the Two-Dimensional Surface-Water Flow in the Horizontal Plane," U.S. Geological Circular 1009, U.S. Department of the Interior, 1986.

Leendertse, J. J., "Aspects of SIMSYS2D, A System for Two-Dimensional Flow Computation," Rand Report R-3712-USGS, U.S. Geological Survey, 1987.

Luettich, R. A., J. J. Westerink, and N. W. Scheffner, "ADCIRC: An Advanced Three-Dimensional Circulation Model for Shelves, Coasts and Estuaries, Report 1: Theory and Methodology of ADCIRC-2DDI and ADCIRC-3DL," Technical Report DRP-92-6, U.S. Army Corps of Engineers Waterways Experiment Station, Vicksburg, MS, 137 pp., 1992.

Luettich, R. A. and J. J. Westerink, "Continental Shelf Scale Convergence Studies with a Barotropic Tidal Model," in *Quantitative Skill Assessment for Coastal Ocean Models, Coastal and Estuarine Studies* **47**, 349–372, American Geophysical Union (1995).

Lynch, D. R., "Progress in Hydrodynamic Modeling, Review of U.S. Contributions 1979–1982," *Rev. Geophys. Space Phys.* **21**(3), 741–754 (1983).

Lynch, D. R. and W. G. Gray, "A Wave Equation Model for Finite Element Tidal Computations," *Comp. Fluids* **7**, 207–228 (1979).

Lynch, D. R. and M. J. Holboke, "Normal Flow Boundary Conditions in 3D Circulation Models," *Int. J. Num. Meth. Fluids* **25**, 1185–1205 (1997).

Lynch, D. R. and F. E. Werner, "Three-Dimensional Velocities from a Finite-Element Model of the English Channel/Southern Bight Tides," *Tidal Hydrodynamics* 183–199 (1984).

Lynch, D. R. and F. E. Werner, "Long Term Simulation and Harmonic Analysis of North Sea/English Channel Tides," in *Computational Methods in Water Resources, Volume 1: Modeling Surface and Sub-Surface Flows*, M. A. Celia, L. A. Ferrand, C. A. Brebbia, W. G. Gray, and G. F. Pinder (eds.), (Computational Mechanics Publication, Elsevier Publishing, 1988), 257–266.

Lynch, D. R., F. E. Werner, A. Cantos-Figuerola, and G. Parilla, "Finite Element Modeling of Reduced-Gravity Flow in the Alboran Sea: Sensitivity Studies," *Seminario Sobre Oceanografia Fisica del Estrecho de Gibraltar*, Madrid, 283–295, 1988.

Lynch, D. R. and F. E. Werner, "Three-Dimensional Hydrodynamics in Finite Elements: Part II: Nonlinear Timestepping," *Int. J. Num. Methods Fluids* **12**, 507–533 (1991).

Ozer, J. and B. M. Jamart, "Tidal Motion in the English Channel and Southern North Sea: Comparisons of Various Observations and Model Results," in *Computational Methods in Water Resources, Volume 1: Modeling Surface and Sub-Surface Flows*, M. A. Celia, L. A. Ferrand, C. A. Brebbia, W. G. Gray, and G. F. Pinder (eds.), (Computational Mechanics Publications, Elsevier Publishing, 1988), 267–273.

Pearson, F., *Map Projections: Theory and Applications* (CRC Press, Inc., Boca Raton, FL, 1990).

Platzman, G. W., "Some Response Characteristics of Finite Element Tidal Models," *J. Comput. Phys.* **40**, 36–63 (1981).

Praagman, N., J. Dijkzeul, R. Van Dijk, and R. Pleiger, "A Finite Difference Model for Tidal Flow in the English Channel and Southern North Sea," *Adv. Water Resources* **12**, 155–164 (1989a).

Praagman, N., J. Dijkzeul, R. Van Dijk, and R. Pleiger, "Simulation of the Tidal Flow in the English Channel and Southern North Sea by a Curvilinear Finite Difference Model," *Adv. Water Resources* **12**, 204–210 (1989b).

Press, W. H., B. P. Flannery, S. A. Teukolsky, and W. T. Vetterling (eds.), *Numerical Recipes, The Art of Scientific Computing* (Cambridge University Press, NY, 1986).

Proudman, J., *Dynamical Oceanography* (Wiley and Sons, New York, NY, 1953).

Ramster, J. W., "Development of Cooperative Research in the North Sea, The Origins, Planning and Philosophy of JONDSAP'76," *Marine Policy*, 318–325 (1977).

Reid, R. O., "Waterlevel Changes," *Handbook of Coastal and Ocean Engineering*, J. Herbich (ed.), (Gulf Publishing, Houston, TX, 1990).

Reid, R. O. and R. E. Whitaker, "Numerical Model for Astronomical Tides in the Gulf of Mexico, Volume I: Theory and Application," Coastal Engineering Research Center, U.S. Army Corps of Engineers Waterways Experiment Station, Vicksburg, MS, 1981.

Roache, P. J., "Perspective: A Method for Uniform Reporting of Grid Refinement Studies," *ASME Journal of Fluids Engineering* **116**, 405–413 (1994).

Schureman, P. "Manual of Harmonic Analysis and Prediction of Tides," Coast and Geodetic Survey, Special Pub. 98, U.S. Department of Commerce (U.S. Government Printing Office, 1958), 317 p.

Schwiderski, E. W., "On Charting Global Ocean Tides," *Rev. Geophys. Space Phys.* **18**, 243–268 (1980).

van Ette, A. C. M. and H. J. Schoemaker, "Harmonic Analysis of Tides, Essential Features and Disturbing Influences," *Proceedings of the Symposium on Tides*, Monaco, 28–29 Apr 1967.

Verboom, G. K. and C. LeProvost, "Information Made Available at the Tidal Flow Forum I, Sixth International Conference on Finite Elements in Water Resources," Lisbon, Portugal, 1986.

Vincent, P. and C. LeProvost, "Semidiurnal Tides in the Northeast Atlantic from a Finite Element Numerical Model," *J. Geophys. Res.* **93**(C1), 543–555 (1988).

Wahr, J. M., "Body Tides on an Elliptical, Rotating, Elastic and Oceanless Earth," *Geophys. J. R. Astr. Soc.* **64**, 677–703 (1981).

Walters, R. A., "A Model for Tides and Currents in the English Channel and Southern North Sea," *Adv. Water Resources* **10**, 138–148 (1987).

Walters, R. A., "A Finite Element Model For Tides and Currents with Field Applications," *Comm. Applied Numerical Methods* **4**, 401–411 (1988).

Walters, R. A. and G. F. Carey, "Analysis of Spurious Oscillation Modes for the Shallow Water and Navier Stokes Equation," *Computers and Fluids* **2**, 51–68 (1983).

Walters, R. A. and F. E. Werner, "A Comparison of Two Finite Element Models of Tidal Hydrodynamics Using a North Sea Data Set," *Adv. in Water Resources* **12**(4), 84–193 (1989).

Werner, F. E., "A Field Test Case for Tidally Forced Flows: A Review of the Tidal Flow Forum," *Quantitative Skill Assessment for Coastal Ocean Models, Coastal and Estuarine Studies* **47**, 269–283 (1995).

Werner, F. E. and D. R. Lynch, "Field Verification of Wave Equation Tidal Dynamics in the English Channel and Southern North Sea," *Adv. Water Resources* **10**, 115–130 (1987).

Werner, F. E. and D. R. Lynch, "Tides in the Southern North Sea/English Channel: Data Files and Procedure for Reference Computation," Thayer School of Engineering, Dartmouth College, Hanover, NH, 26 pp. and data files, 1988.

Werner, F. E. and D. R. Lynch, "Harmonic Structure of English Channel/Southern Bight Tides from a Wave Equation Simulation," *Adv. Water Resources* **12**, 121–142 (1989).

Westerink, J. J., K. D. Stolzenbach, and J. J. Connor, "General Spectral Computations of the Nonlinear Shallow Water Tidal Interactions Within the Bight of Abaco," *J. Phys. Oceanogr.* **19**, 1350–1373 (1989).

Westerink, J. J. and W. G. Gray, "Progress in Surface Water Modeling," *Rev. Geophys.* **29**, April Supplement, 210–217 (1991).

Westerink, J. J., R. A. Luettich, A. M. Baptista, N. W. Scheffner, and P. Farrar, "Tide and Storm Surge Predictions Using a Finite Element Model," *J. Hydraul. Eng.* **118**, 1373–1390 (1992a).

Westerink, J. J., R. A. Luettich, C. A. Blain, and N. W. Scheffner, "ADCIRC: An Advanced Three-Dimensional Circulation Model for Shelves, Coast and Estuaries, Report 2: User's Manual for ADCIRC-2DDI," Tech. Report DRP-92, Department of the Army, 1992b.

Westerink, J. J., R. A. Luettich, and J. C. Muccino, "Modeling Tides in the Western North Atlantic Using Unstructured Graded Grids," *Tellus* **46A**, 178–199 (1994a).

Westerink, J. J., R. A. Luettich, J. K. Wu, and R. L. Kolar, "The Influence of Normal Flow Boundary Conditions on Spurious Modes in Finite Element Solutions to the Shallow Water Equations," *Int. J. Num. Meth. Fluids* **18**, 1021–1060 (1994b).

Westerink, J. J., R. A. Luettich, and S. C. Hagen, "Meshing Requirements for Large Scale Coastal Ocean Tidal Models," *Numerical Methods in Water Resources*, A. Peters, G. Wittum, B. Herrling, and U. Meissner (eds.), (Kluwer Academic Publishers, The Netherlands, 1994c).

Westerink, J. J., R. A. Luettich, C. A. Blain, and S. C. Hagen, "The Utility of the Finite Element Method in Computing Surface Elevation and Circulation in Continental Margin Waters," *Finite Element Modeling of Environmental Problems*, G. F. Carey (ed.), (John Wiley and Sons, New York, NY, 1995), pp. 39–59.

Westerink, J. J. and P. Roache, "Issues in Convergence Studies in Geophysical Flow Computations," *Next Generation Environmental Models Computational Methods*, G. Delic and M. Wheeler (eds.), (Society of Industrial and Applied Mathematics, Philadelphia, PA, 1996).

Woodworth, P. L., "Summary of Recommendations to the UK Earth Observation Data Centre (UK-EODC) by the Proudman Oceanographic Laboratory (POL) for Tide Model Corrections on ERS-1 Geophysical Data Records," Proudman Oceanographic Laboratory Communication, 1990.

Yu, C. S., M. Fettweis, I. Hermans, and J. Berlamont, "Tidal Flow Simulation in the English Channel and Southern North Sea," *Adv. Water Resources* **12**, 194–203 (1989).

## Appendix A

### RAW MODEL-DATA ELEVATION COMPARISONS FOR THE BASE SIMULATION

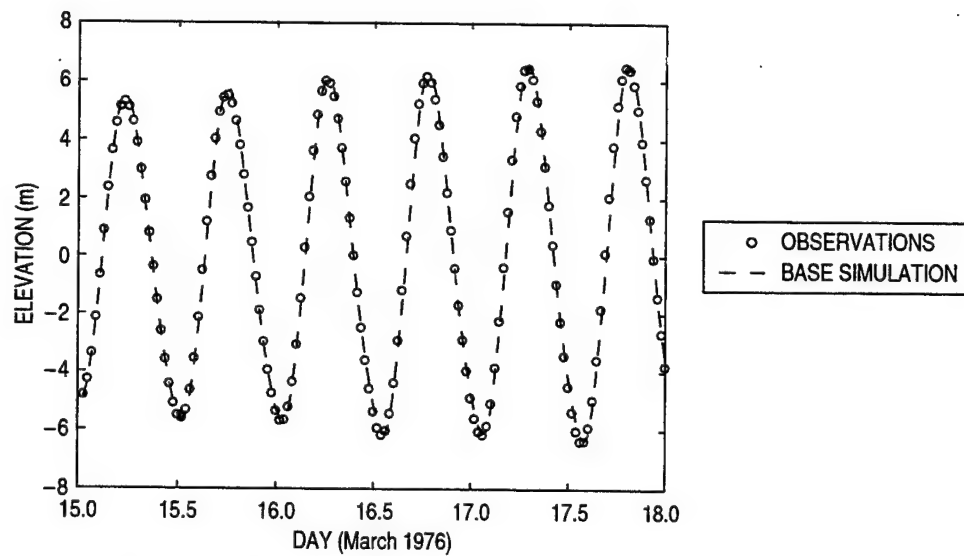


Fig. A1 — Base simulation tidal elevations, tidal gauge at St. Malo

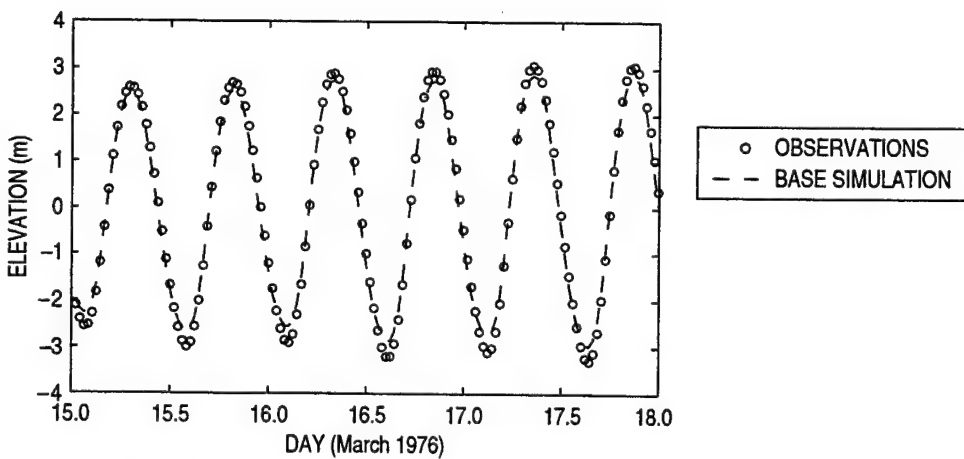


Fig. A2 — Base simulation tidal elevations, tidal gauge at Cherbourg

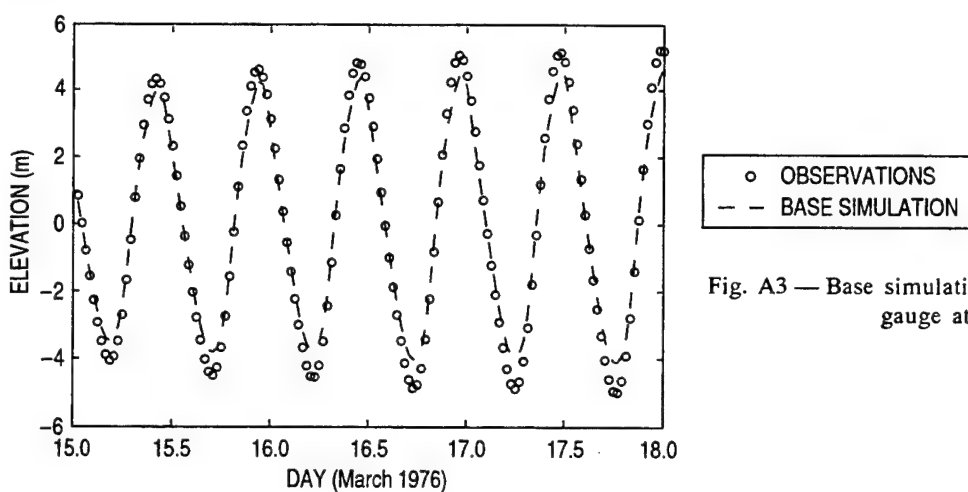


Fig. A3 — Base simulation tidal elevations, tidal gauge at Dieppe

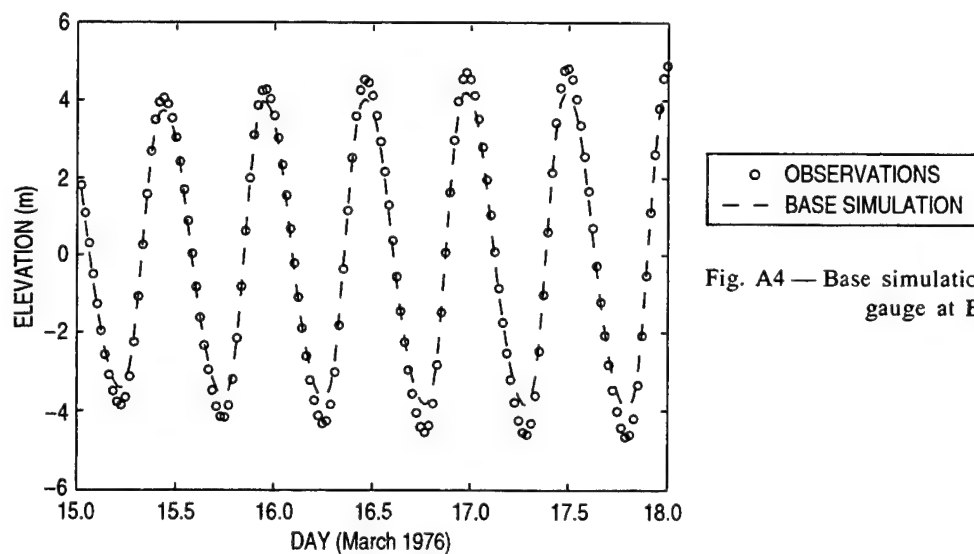


Fig. A4 — Base simulation tidal elevations, tidal gauge at Boulogne

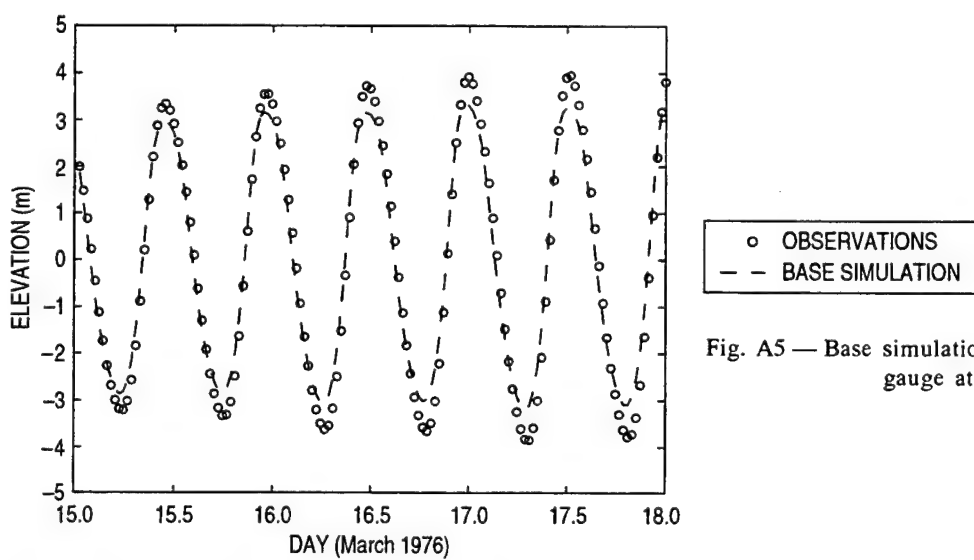


Fig. A5 — Base simulation tidal elevations, tidal gauge at Calais

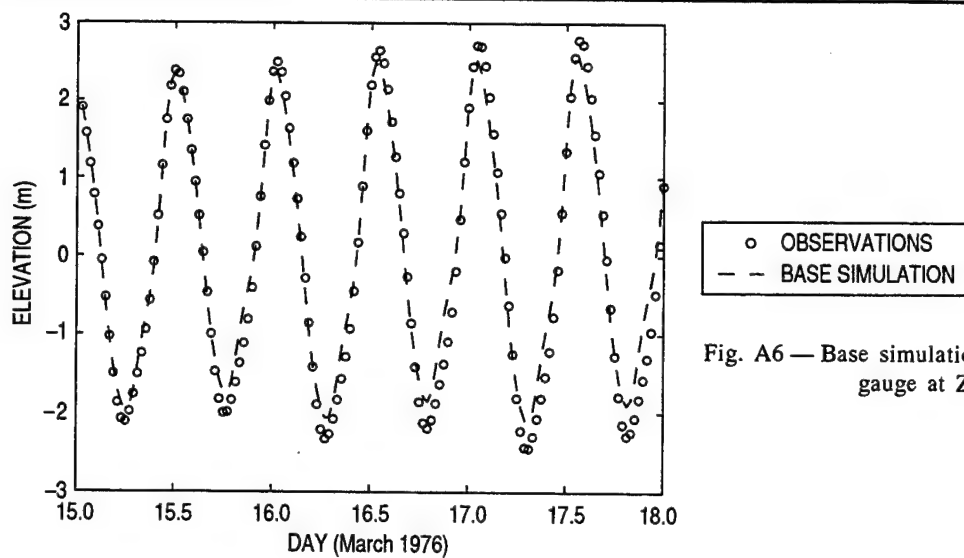


Fig. A6 — Base simulation tidal elevations, tidal gauge at Zeebrugge

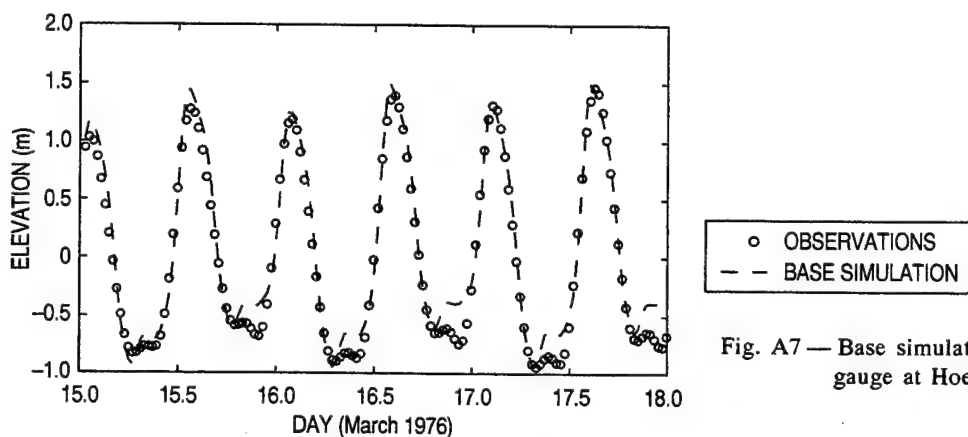


Fig. A7 — Base simulation tidal elevations, tidal gauge at Hoek van Holland

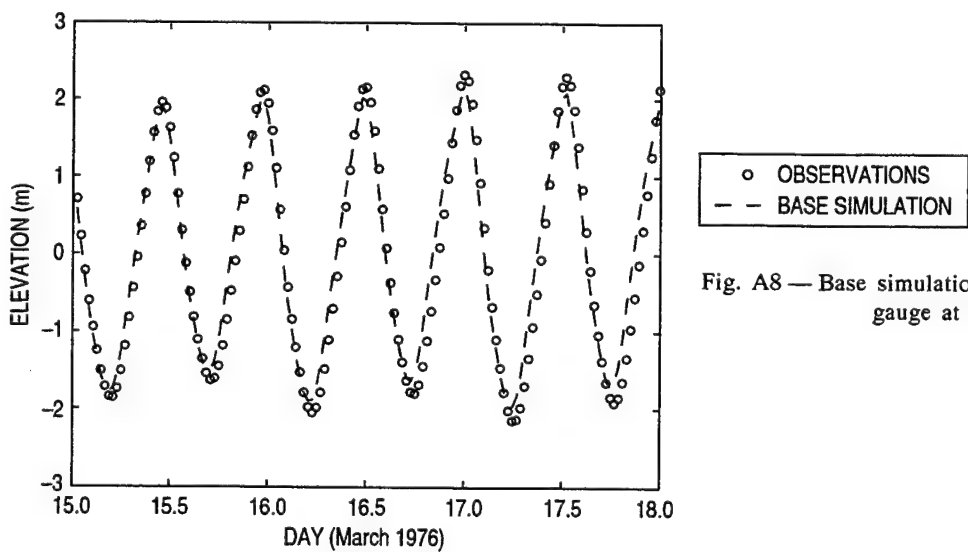


Fig. A8 — Base simulation tidal elevations, tidal gauge at Walton

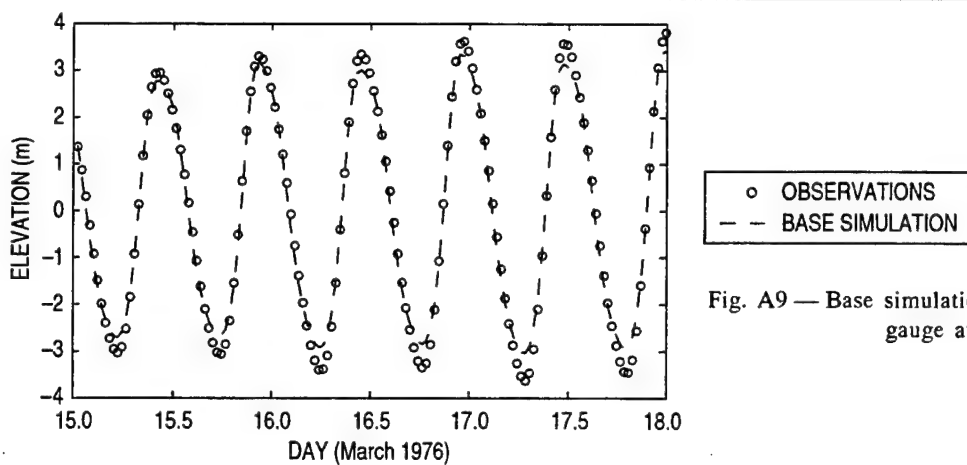


Fig. A9 — Base simulation tidal elevations, tidal gauge at Dover

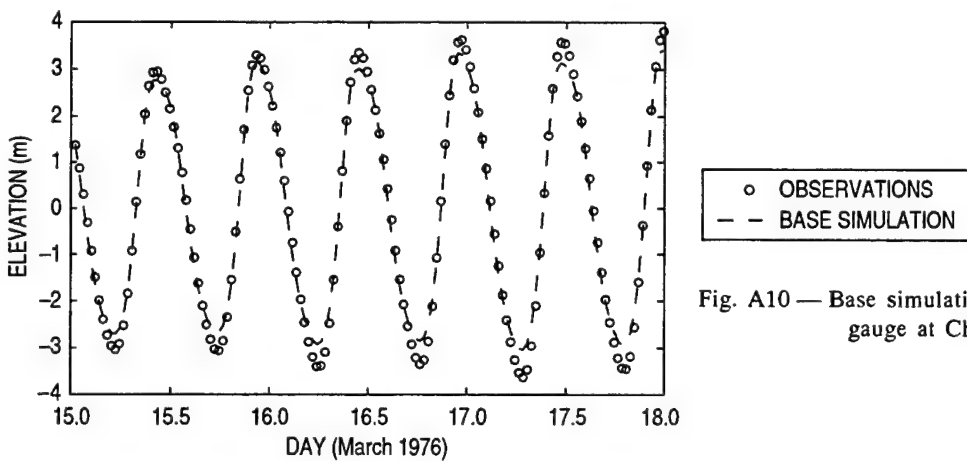


Fig. A10 — Base simulation tidal elevations, tidal gauge at Christchurch

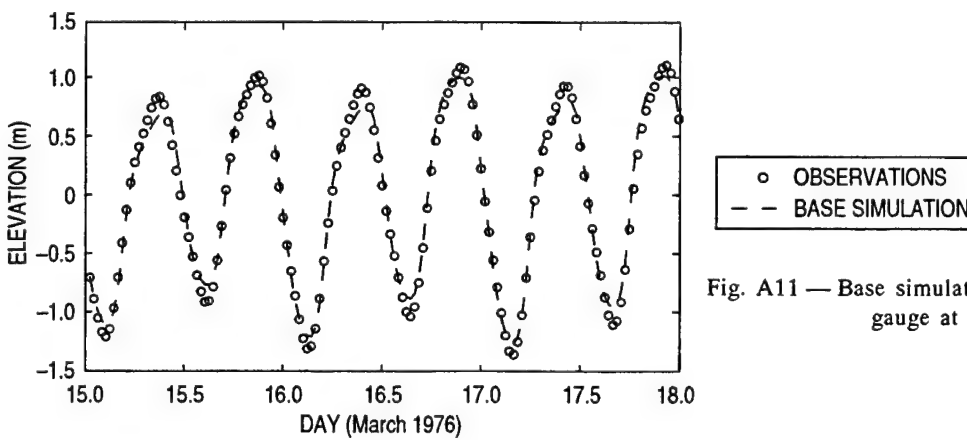


Fig. A11 — Base simulation tidal elevations, tidal gauge at Lowestoft

## Appendix B

### “FILTERED” MODEL-DATA ELEVATION COMPARISONS FOR THE BASE SIMULATION

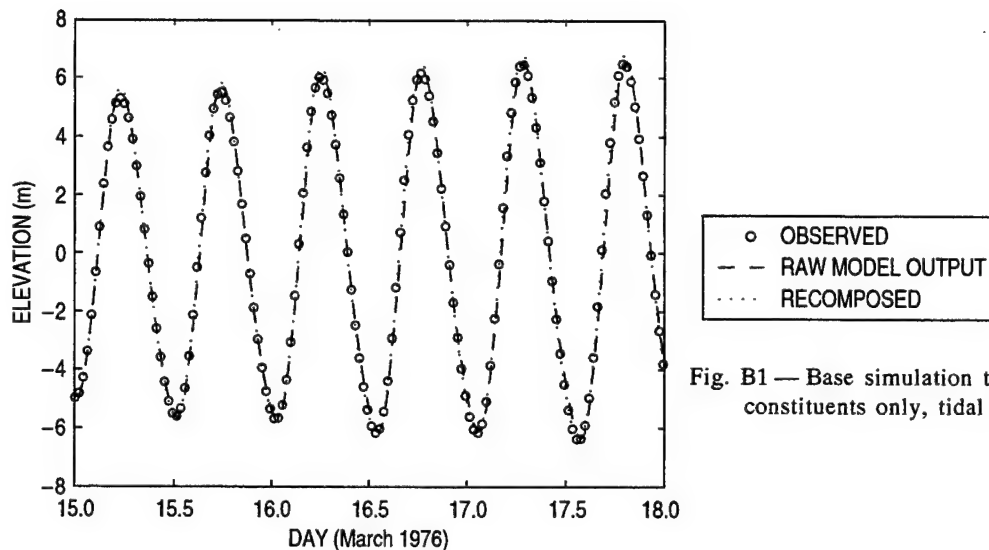


Fig. B1 — Base simulation tidal elevations, 11 TFF constituents only, tidal gauge at St. Malo

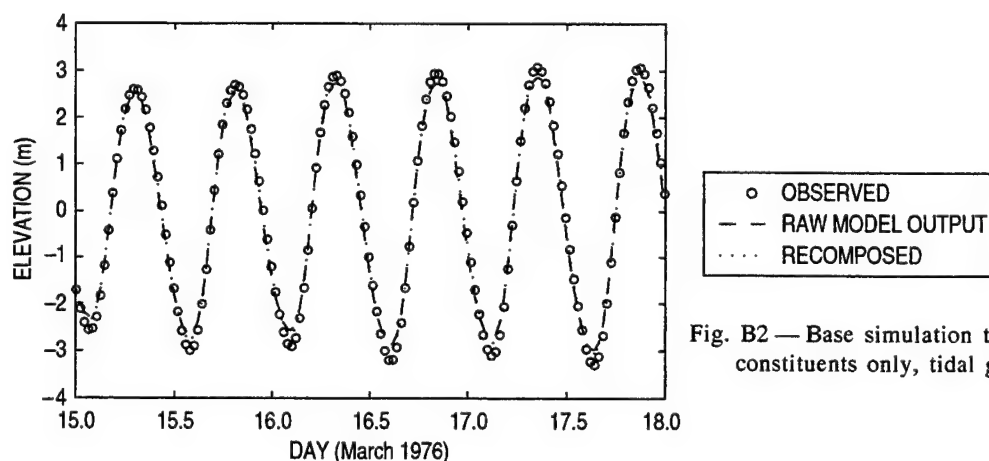


Fig. B2 — Base simulation tidal elevations, 11 TFF constituents only, tidal gauge at Cherbourg

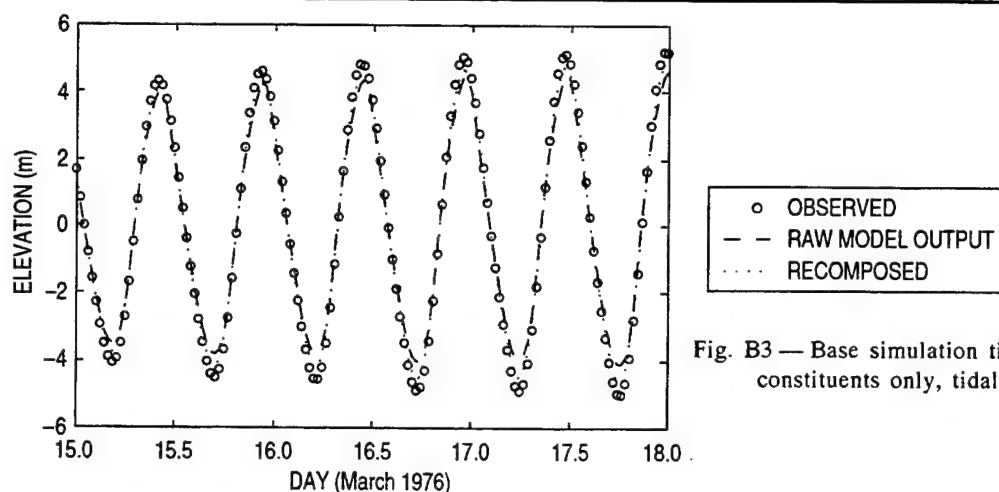


Fig. B3 — Base simulation tidal elevations, 11 TFF constituents only, tidal gauge at Dieppe

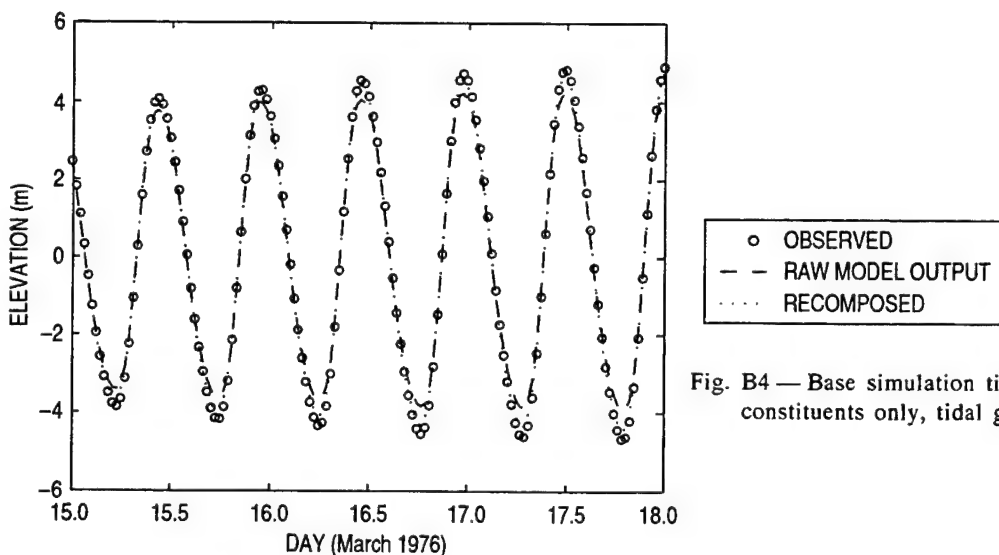


Fig. B4 — Base simulation tidal elevations, 11 TFF constituents only, tidal gauge at Boulogne

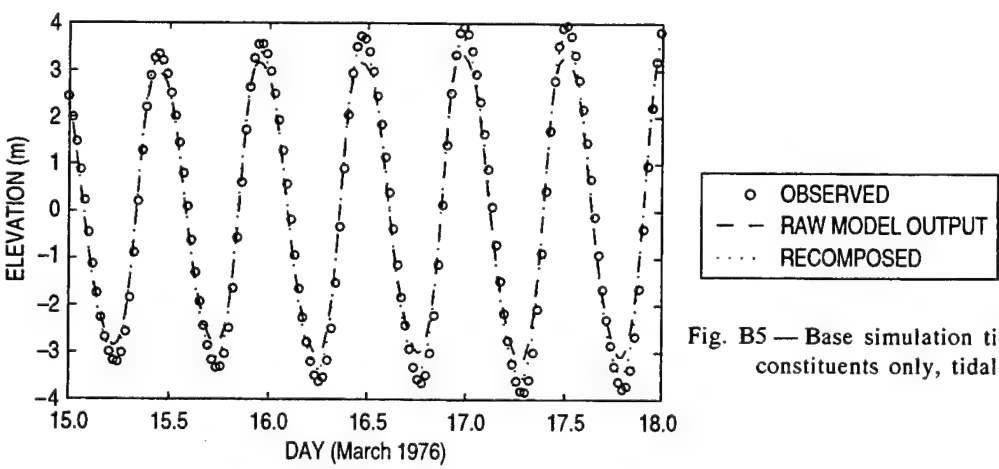


Fig. B5 — Base simulation tidal elevations, 11 TFF constituents only, tidal gauge at Calais

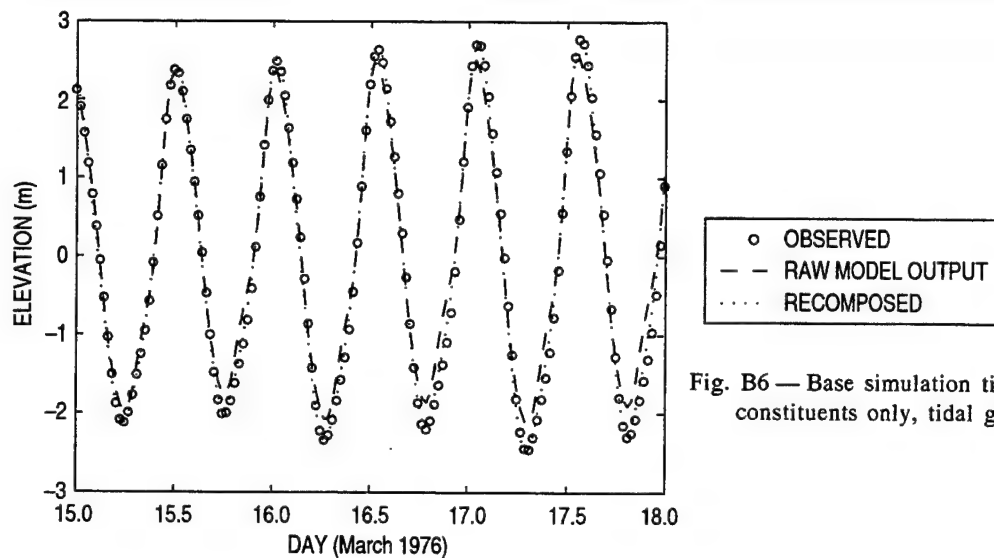


Fig. B6 — Base simulation tidal elevations, 11 TFF constituents only, tidal gauge at Zeebrugge

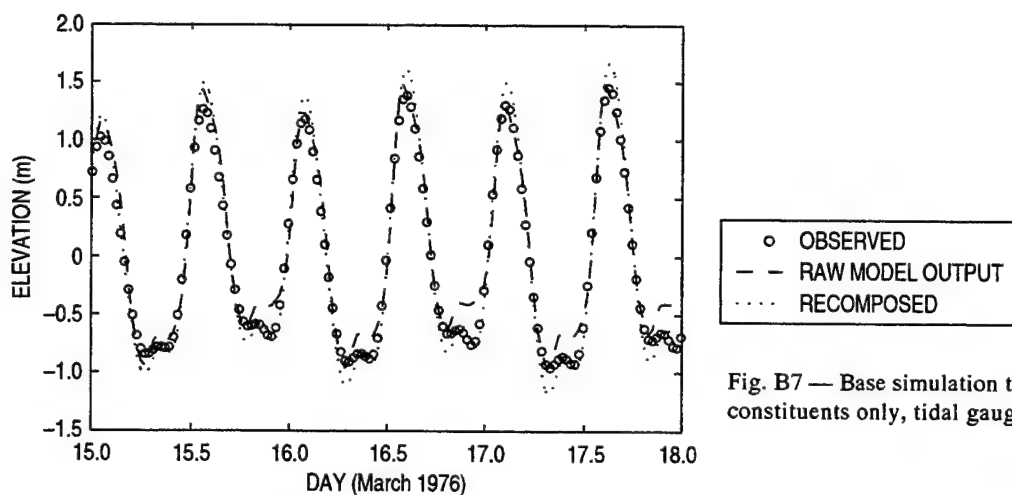


Fig. B7 — Base simulation tidal elevations, 11 TFF constituents only, tidal gauge at Hoek van Holland

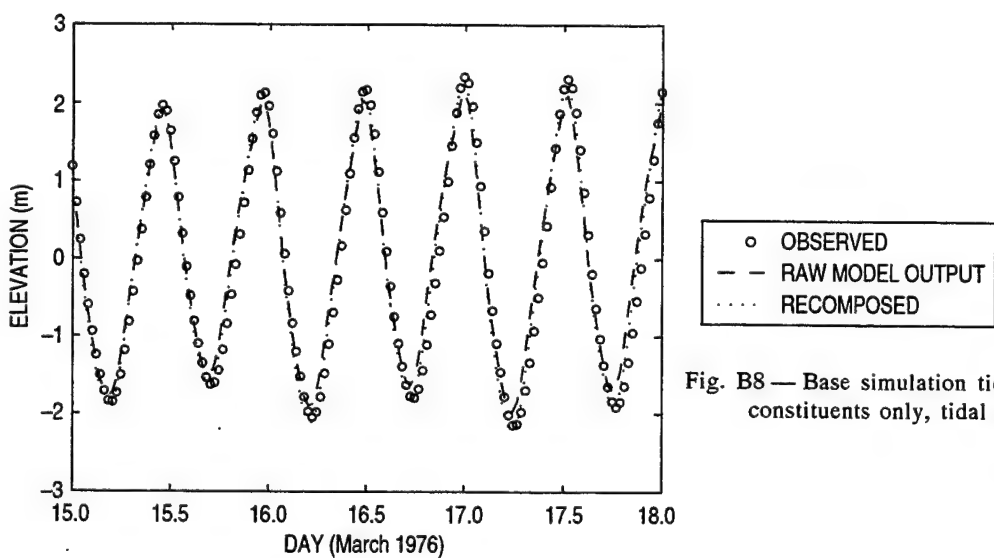


Fig. B8 — Base simulation tidal elevations, 11 TFF constituents only, tidal gauge at Walton

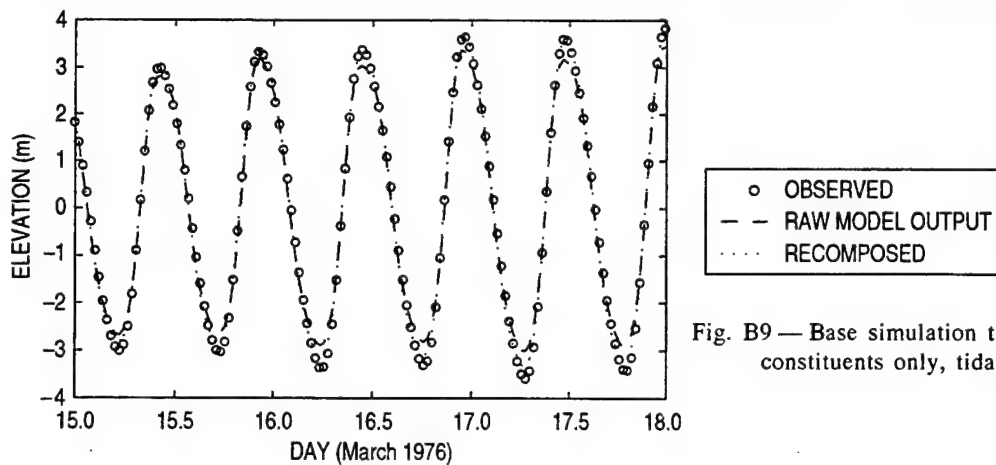


Fig. B9 — Base simulation tidal elevations, 11 TFF constituents only, tidal gauge at Dover

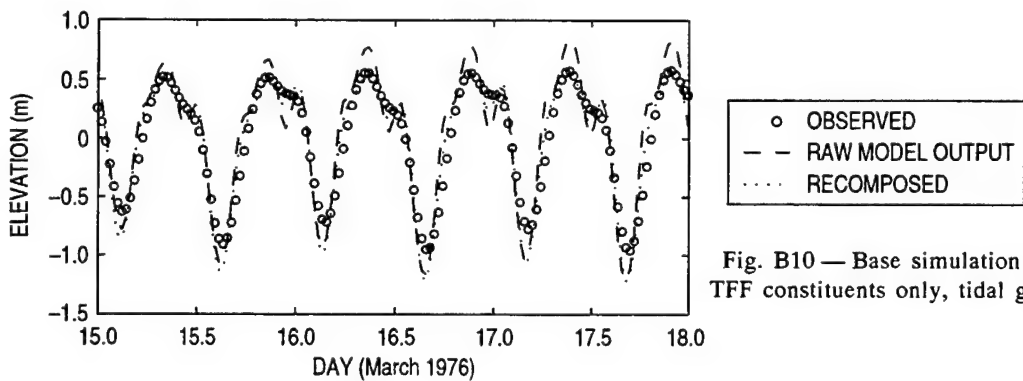


Fig. B10 — Base simulation tidal elevations, 11 TFF constituents only, tidal gauge at Christchurch

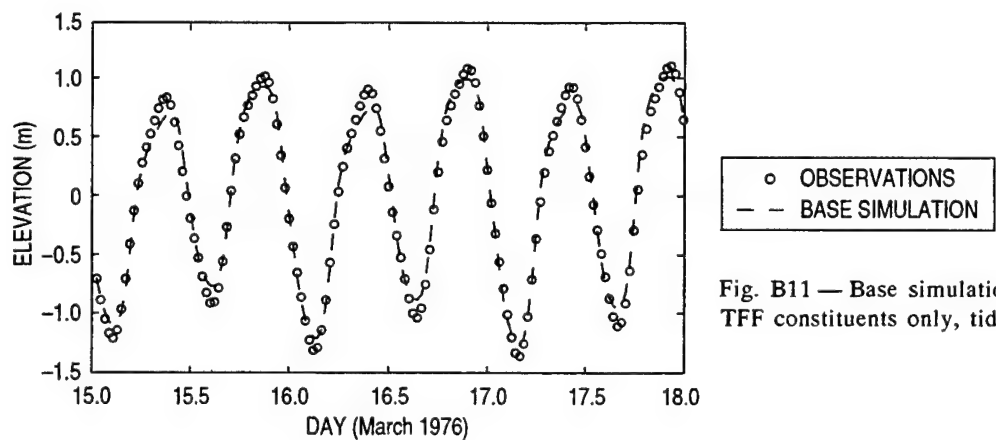


Fig. B11 — Base simulation tidal elevations, 11 TFF constituents only, tidal gauge at Lowestoft

## Appendix C

### TIDAL CONSTITUENT COMPARISONS FOR THE BASE SIMULATION

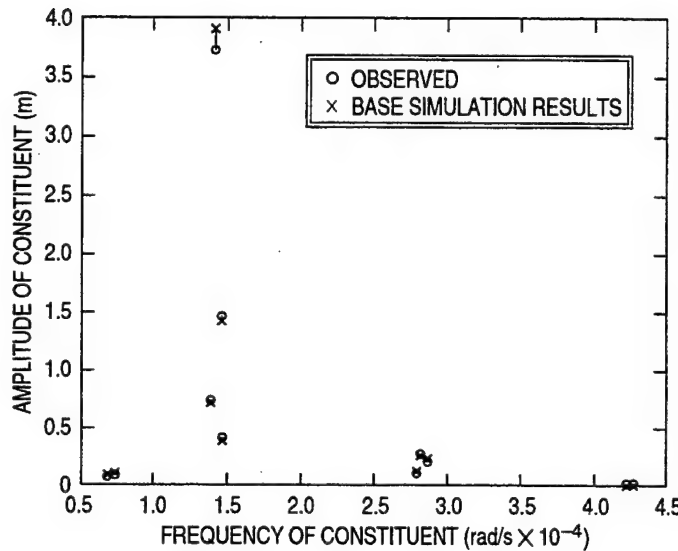


Fig. C1 — Base simulation constituent amplitudes, tidal gauge at St. Malo

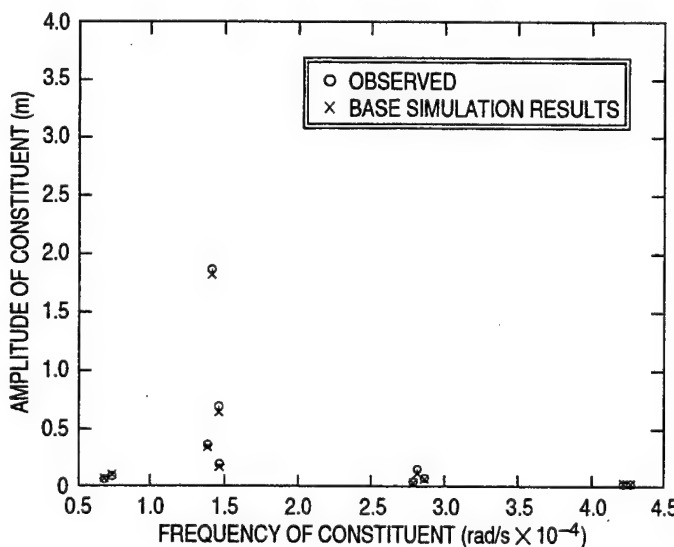


Fig. C2 — Base simulation constituent amplitudes, tidal gauge at Cherbourg

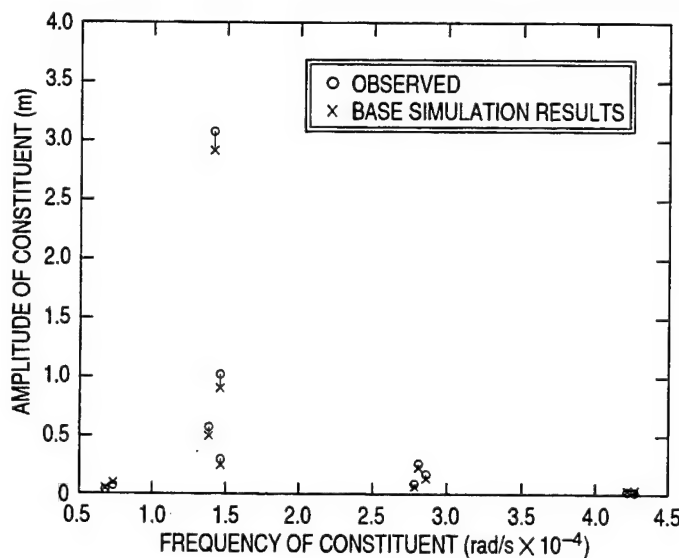


Fig. C3 — Base simulation constituent amplitudes, tidal gauge at Dieppe

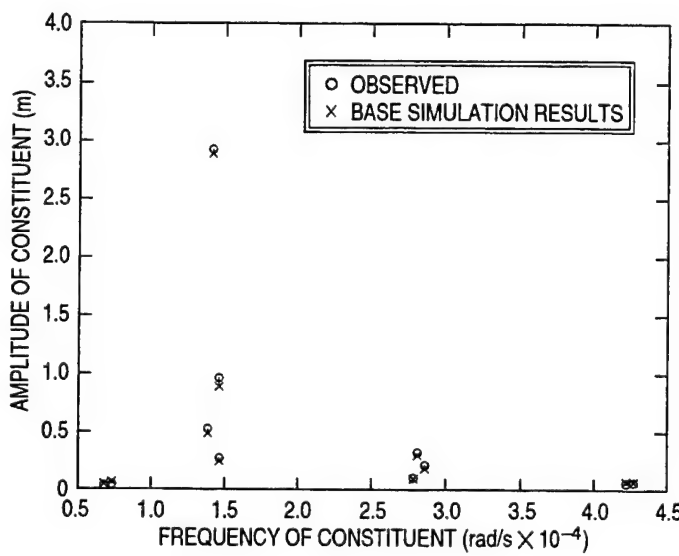


Fig. C4 — Base simulation constituent amplitudes, tidal gauge at Boulogne

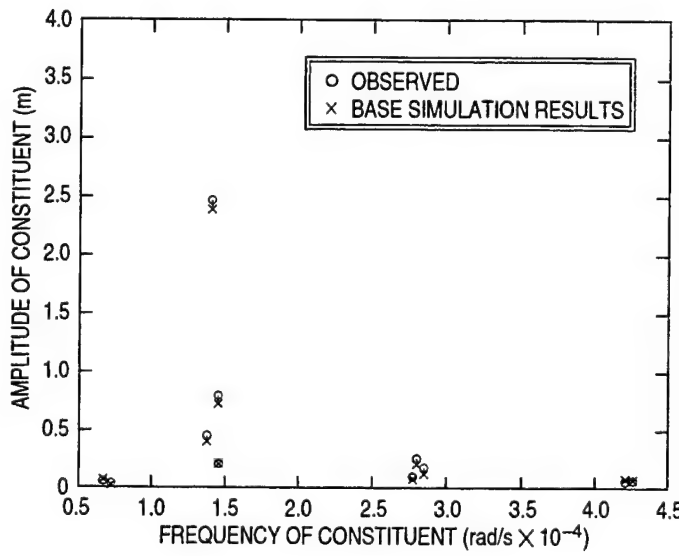


Fig. C5 — Base simulation constituent amplitudes, tidal gauge at Calais

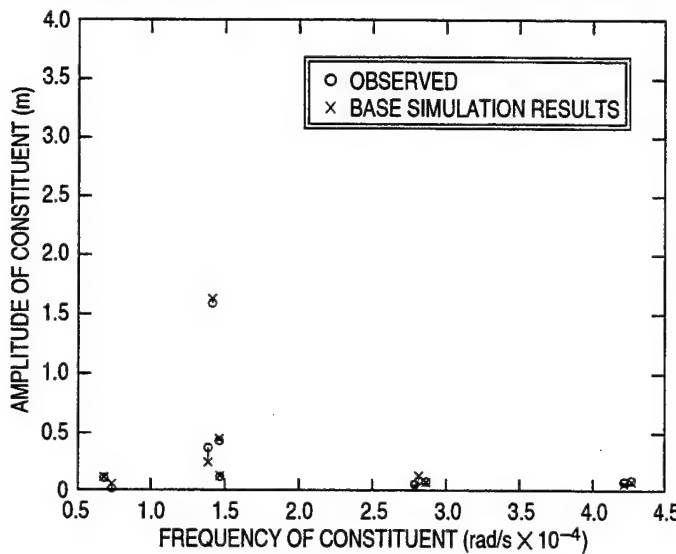


Fig. C6—Base simulation constituent amplitudes, tidal gauge at Zeebrugge

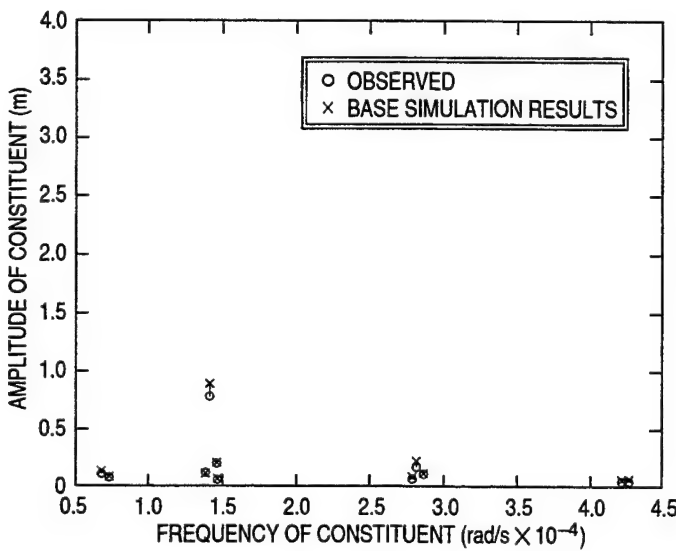


Fig. C7—Base simulation constituent amplitudes, tidal gauge at Hoek van Holland

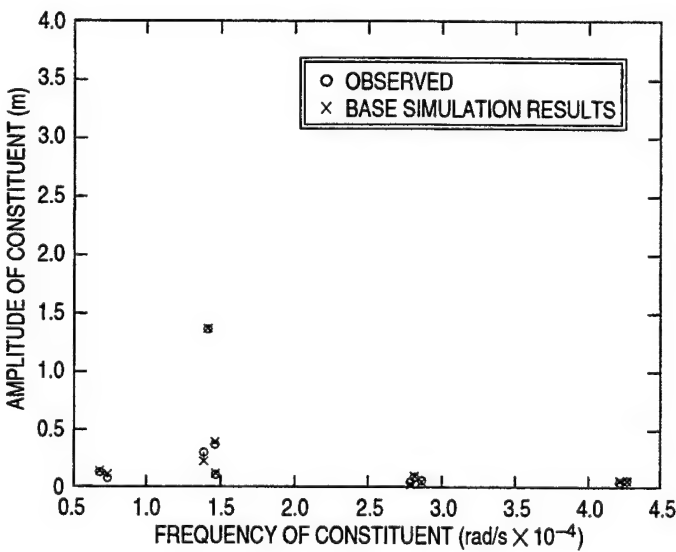


Fig. C8—Base simulation constituent amplitudes, tidal gauge at Walton

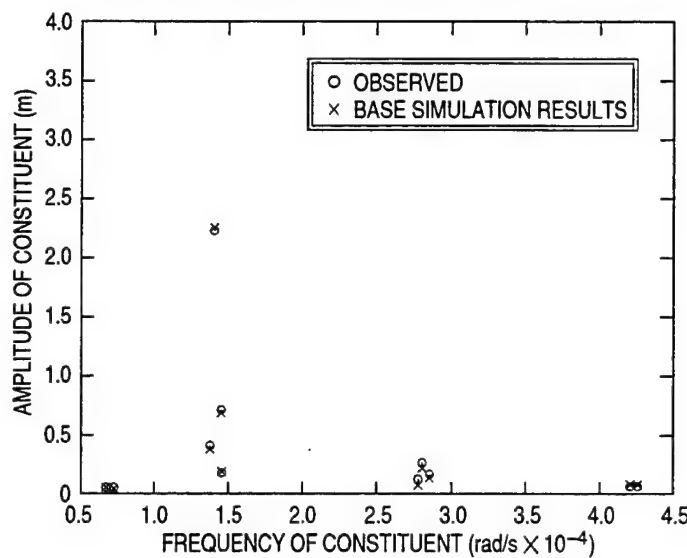


Fig. C9 — Base simulation constituent amplitudes, tidal gauge at Dover

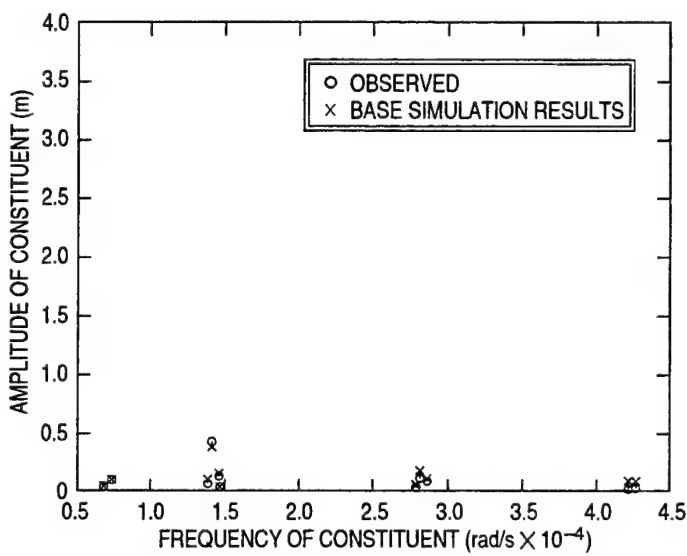


Fig. C10 — Base simulation constituent amplitudes, tidal gauge at Christchurch

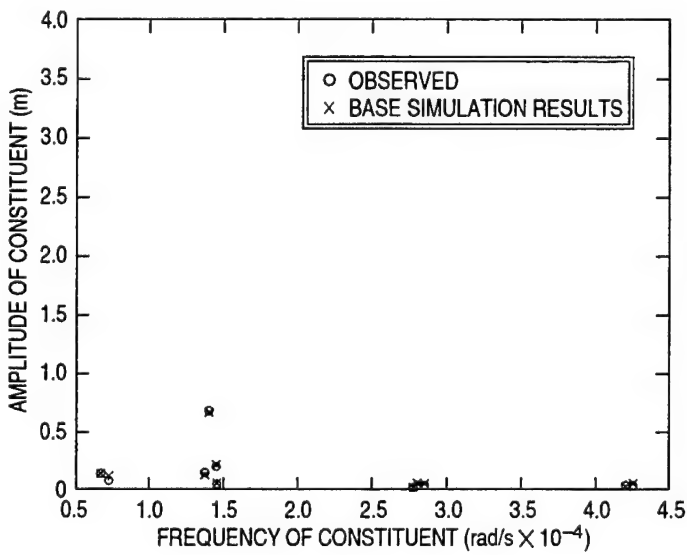


Fig. C11 — Base simulation constituent amplitudes, tidal gauge at Lowestoft

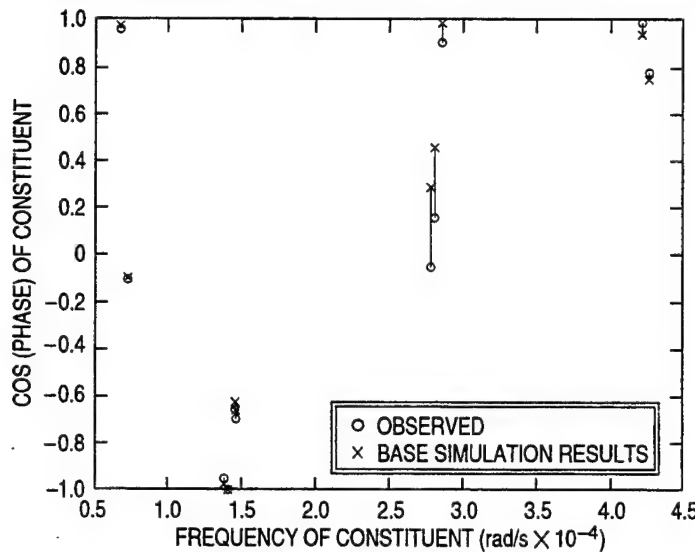


Fig. C12 — Base simulation constituent phases, tidal gauge at St. Malo

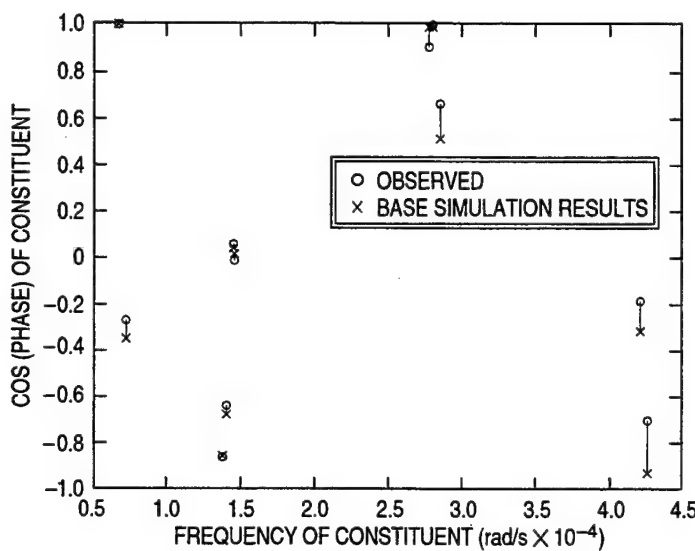


Fig. C13 — Base simulation constituent phases, tidal gauge at Cherbourg

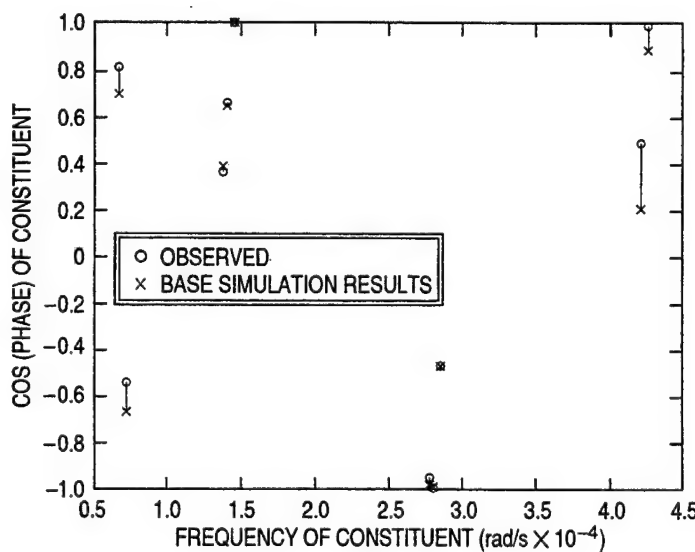


Fig. C14 — Base simulation constituent phases, tidal gauge at Dieppe

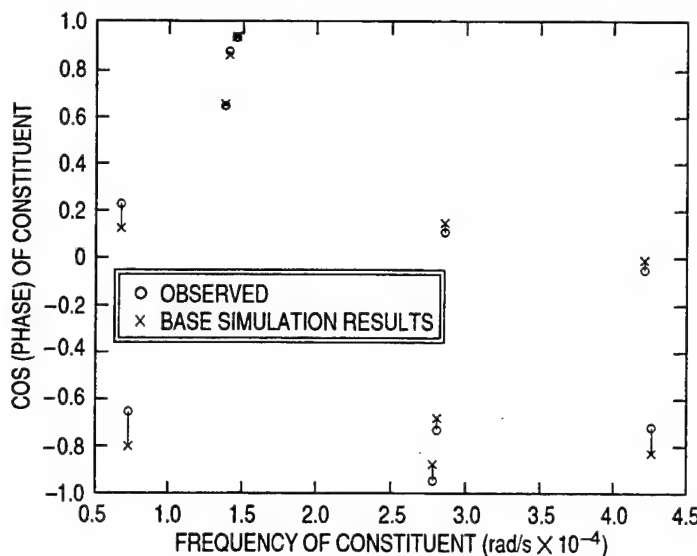


Fig. C15 — Base simulation constituent phases, tidal gauge at Boulogne

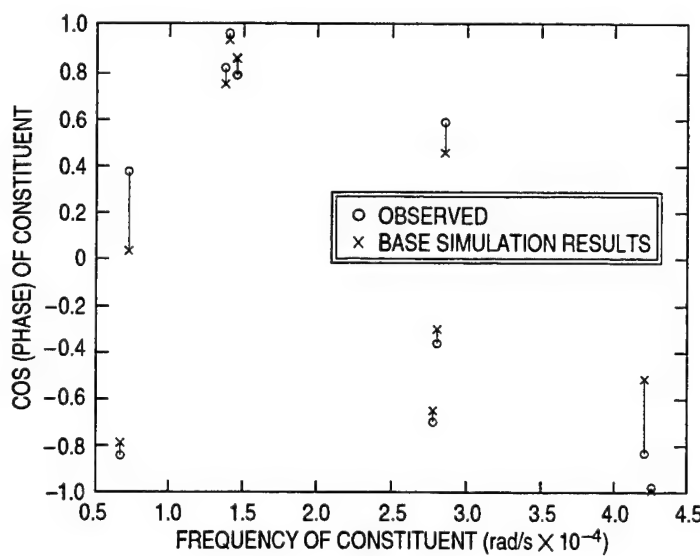


Fig. C16 — Base simulation constituent phases, tidal gauge at Calais

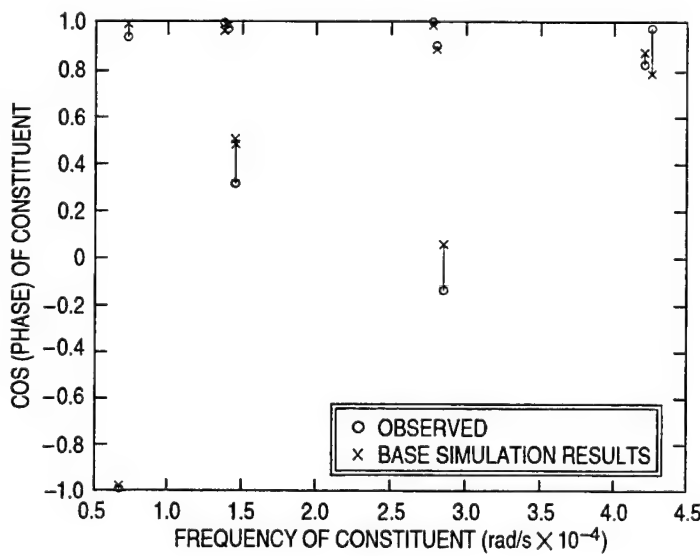


Fig. C17 — Base simulation constituent phases, tidal gauge at Zeebrugge

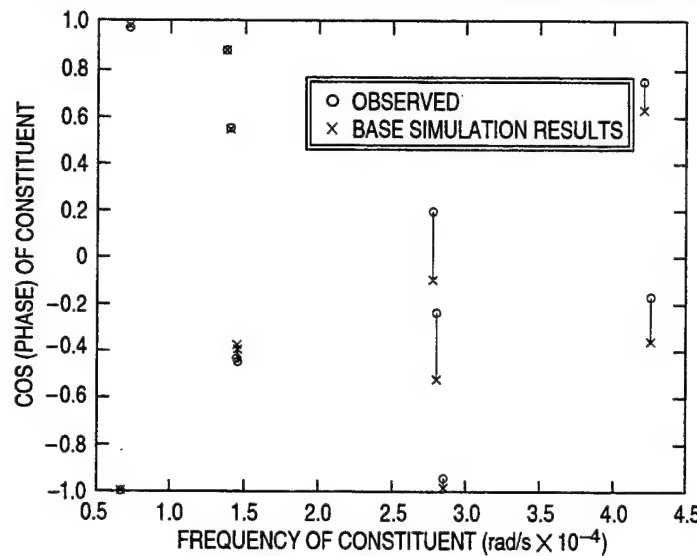


Fig. C18 — Base simulation constituent phases, tidal gauge at Hoek van Holland

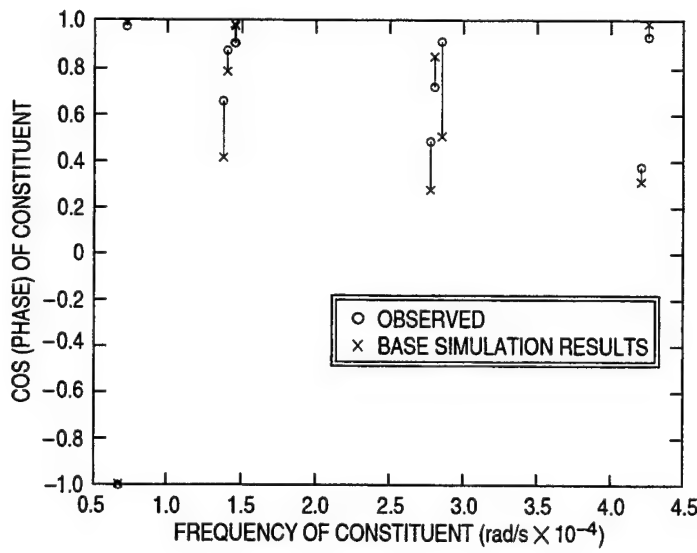


Fig. C19 — Base simulation constituent phases, tidal gauge at Walton

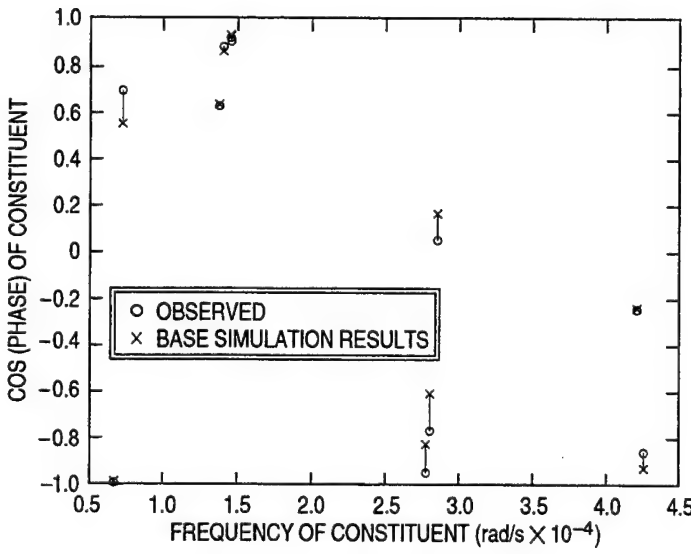


Fig. C20 — Base simulation constituent phases, tidal gauge at Dover

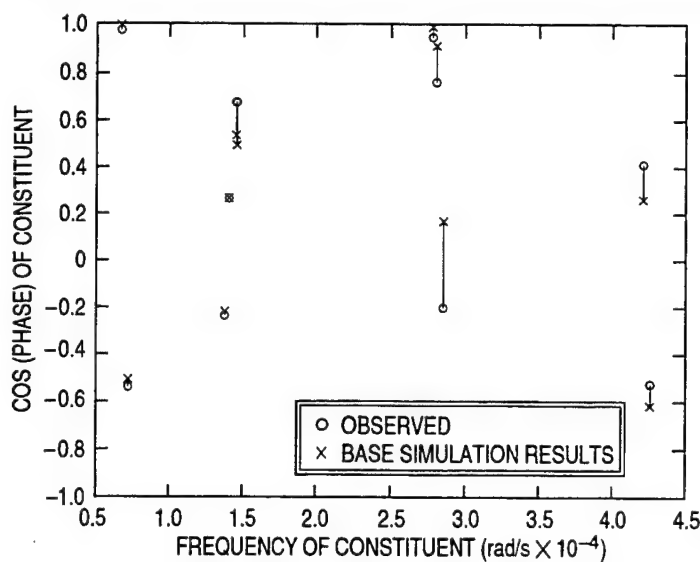


Fig. C21 — Base simulation constituent phases, tidal gauge at Christchurch

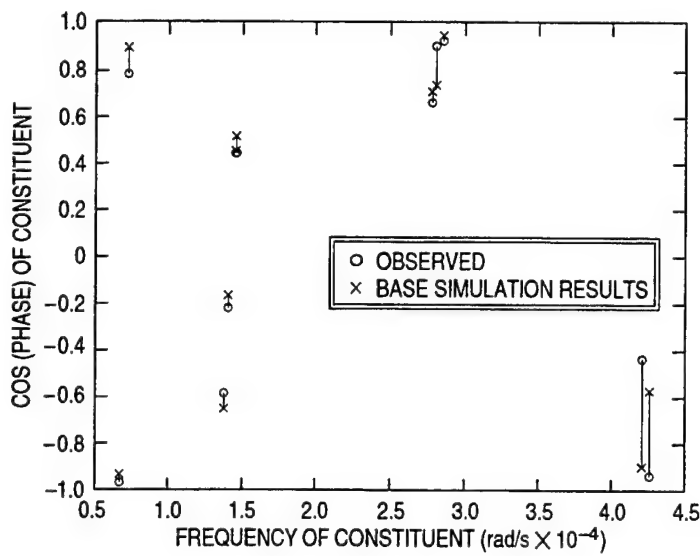


Fig. C22 — Base simulation constituent phases, tidal gauge at Lowestoft

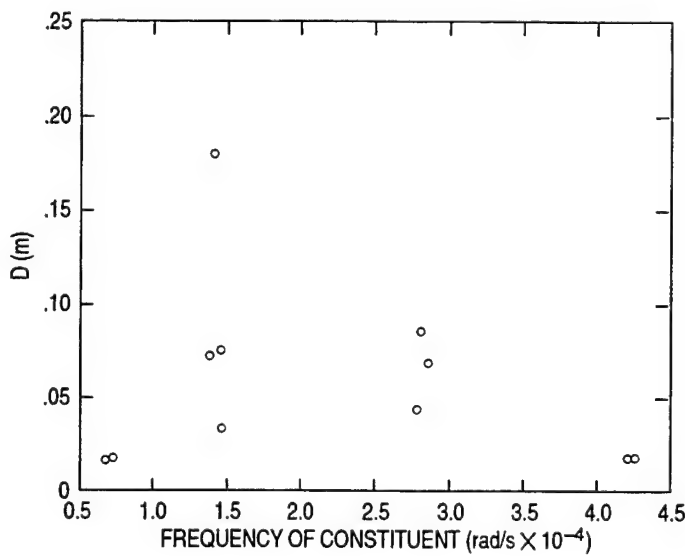


Fig. C23 — Base simulation constituent errors in the complex plane, tidal gauge at St. Malo

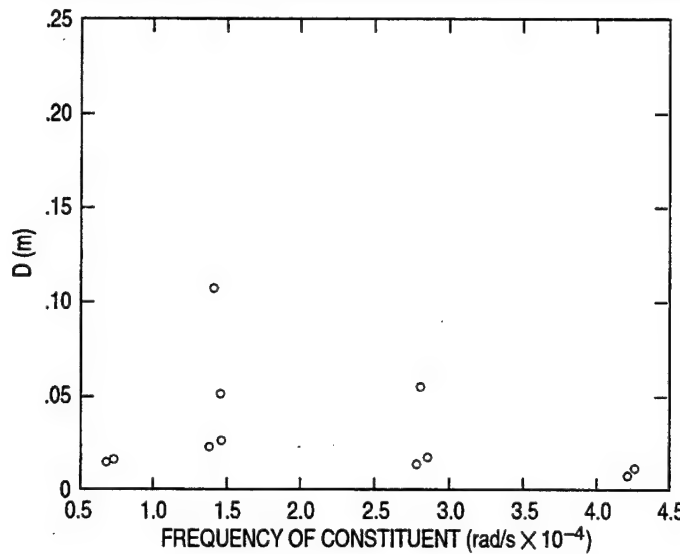


Fig. C24 — Base simulation constituent errors in the complex plane, tidal gauge at Cherbourg

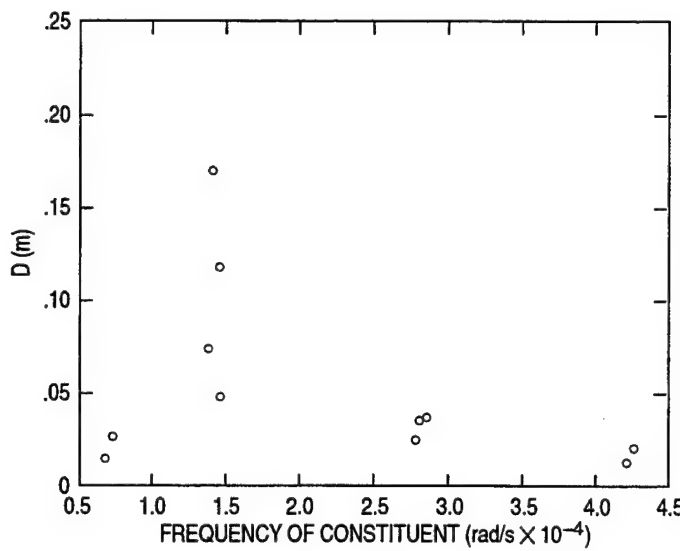


Fig. C25 — Base simulation constituent errors in the complex plane, tidal gauge at Dieppe

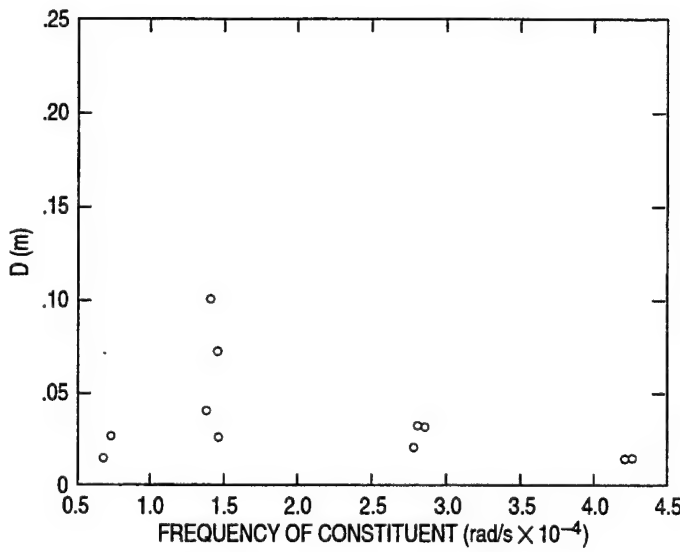


Fig. C26 — Base simulation constituent errors in the complex plane, tidal gauge at Boulogne

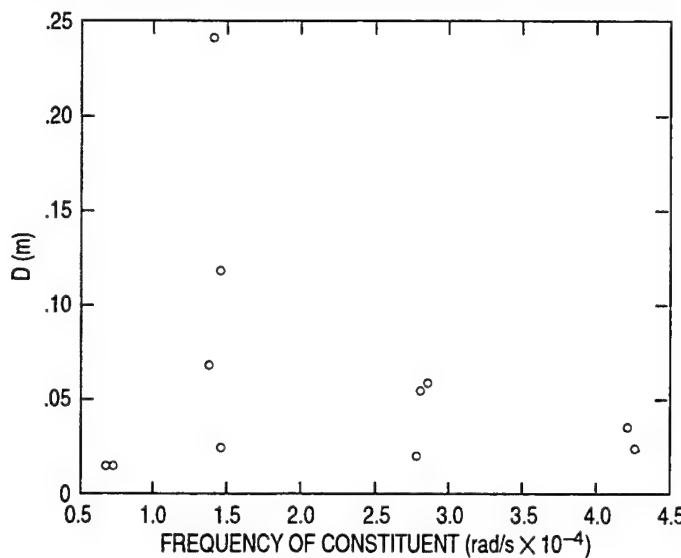


Fig. C27 — Base simulation constituent errors in the complex plane, tidal gauge at Calais

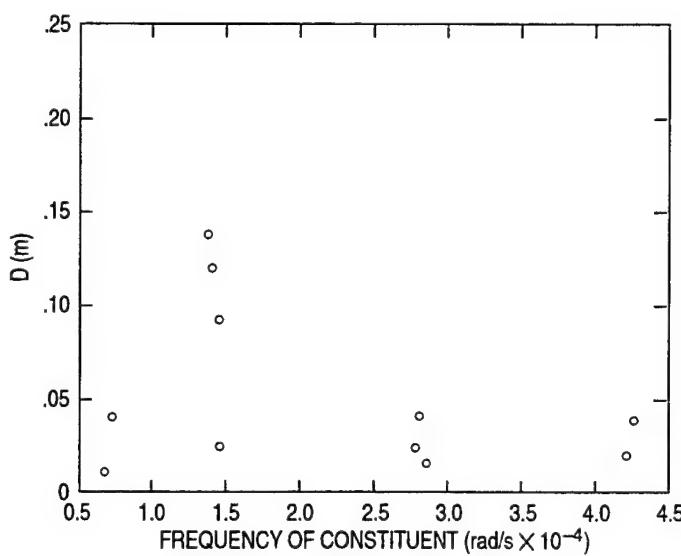


Fig. C28 — Base simulation constituent errors in the complex plane, tidal gauge at Zeebrugge

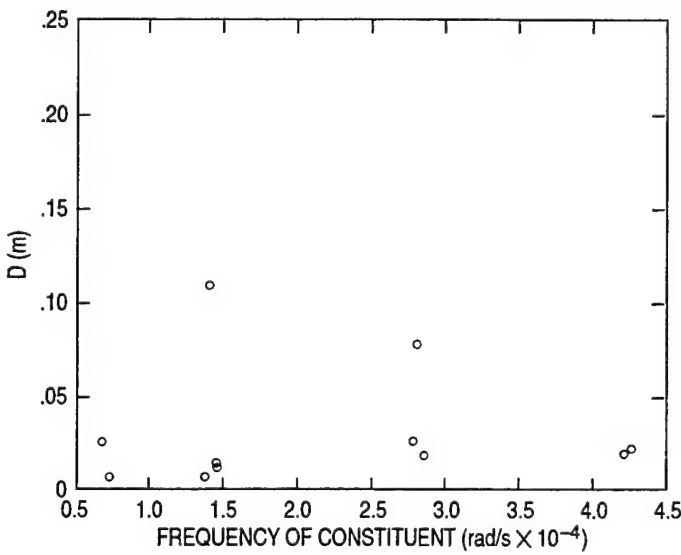


Fig. C29 — Base simulation constituent errors in the complex plane, tidal gauge at Hoek van Holland

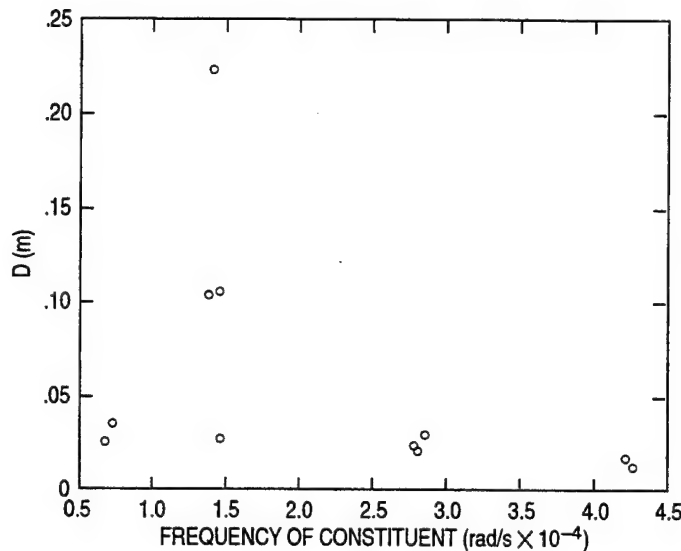


Fig. C30 — Base simulation constituent errors in the complex plane, tidal gauge at Walton

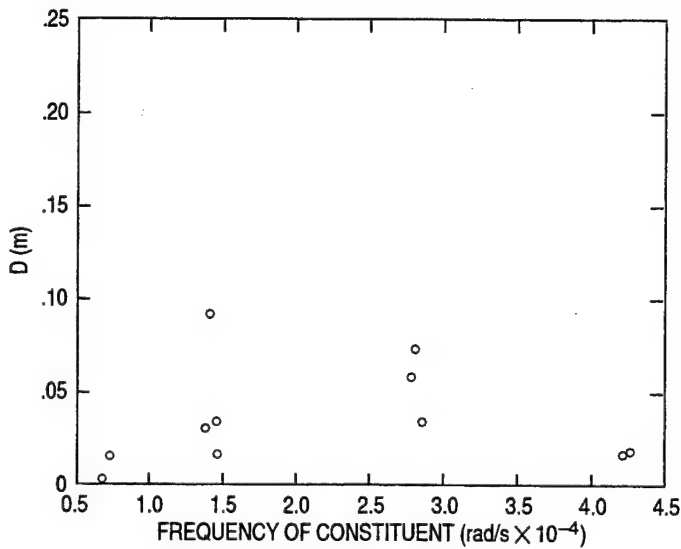


Fig. C31 — Base simulation constituent errors in the complex plane, tidal gauge at Dover

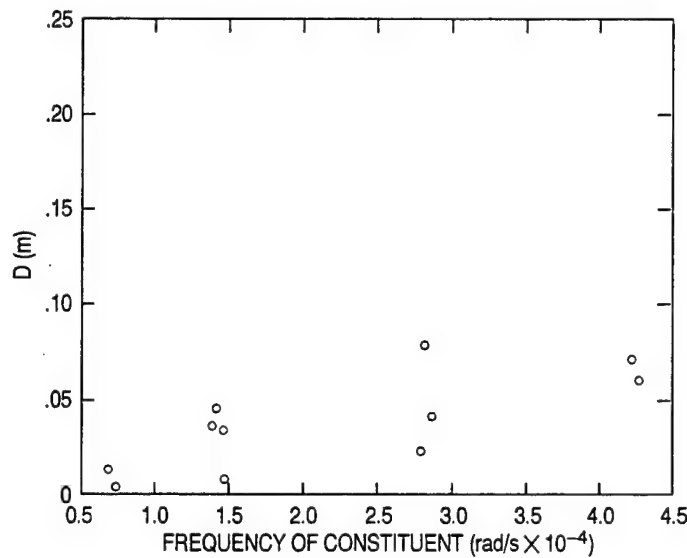


Fig. C32 — Base simulation constituent errors in the complex plane, tidal gauge at Christchurch

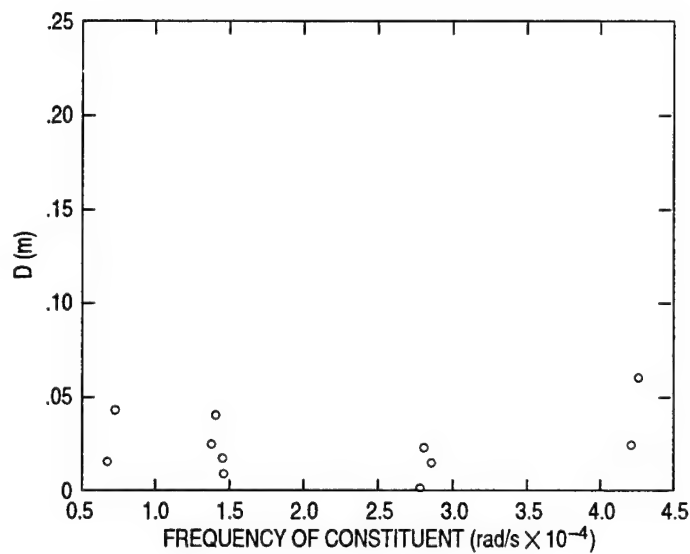


Fig. C33 — Base simulation constituent errors in the complex plane, tidal gauge at Lowestoft

## Appendix D

### MODEL-DATA VELOCITY COMPARISONS FOR THE BASE SIMULATION

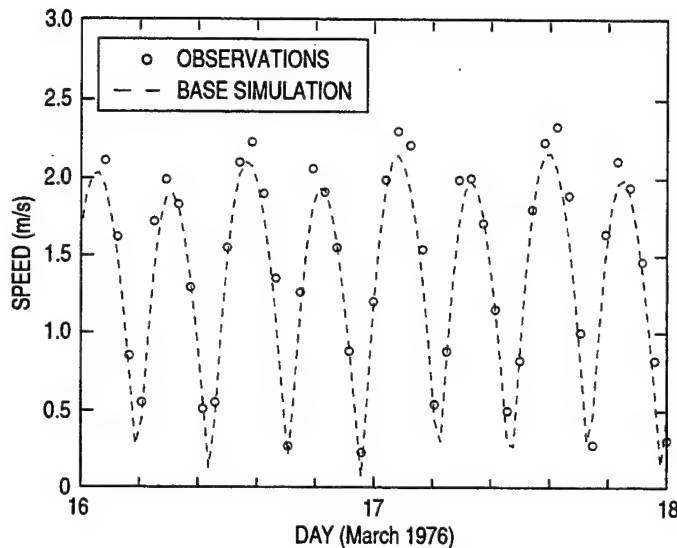


Fig. D1 — Base simulation speeds, velocity gauge 1

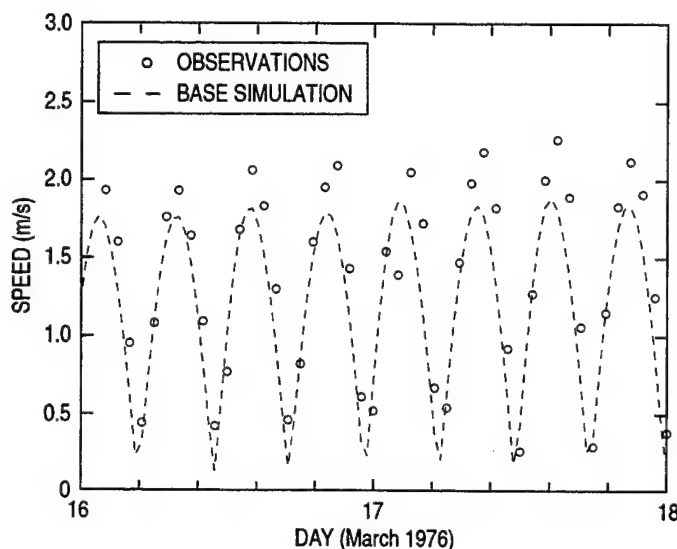


Fig. D2 — Base simulation speeds, velocity gauge 2

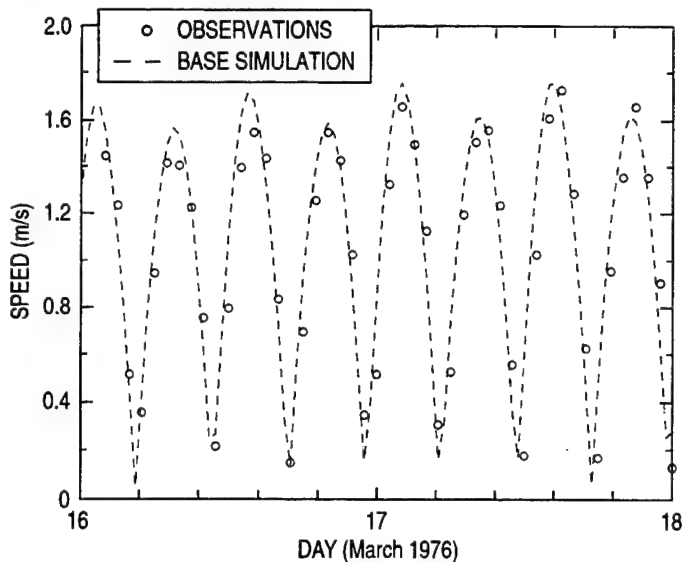


Fig. D3 — Base simulation speeds, velocity gauge 3

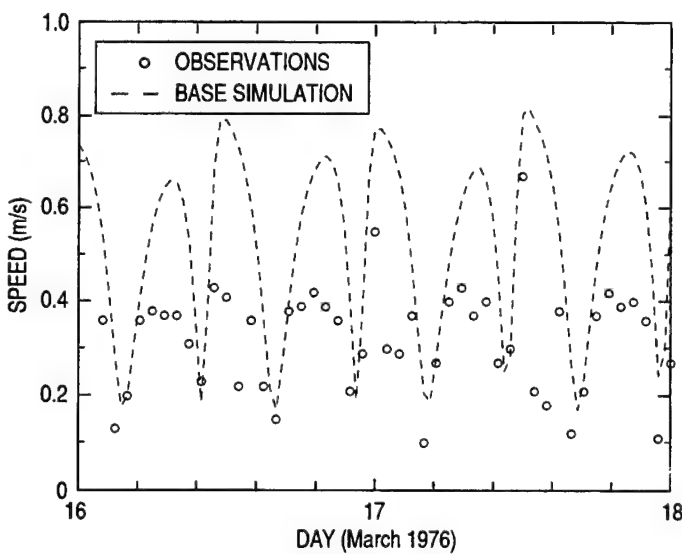


Fig. D4 — Base simulation speeds, velocity gauge 4

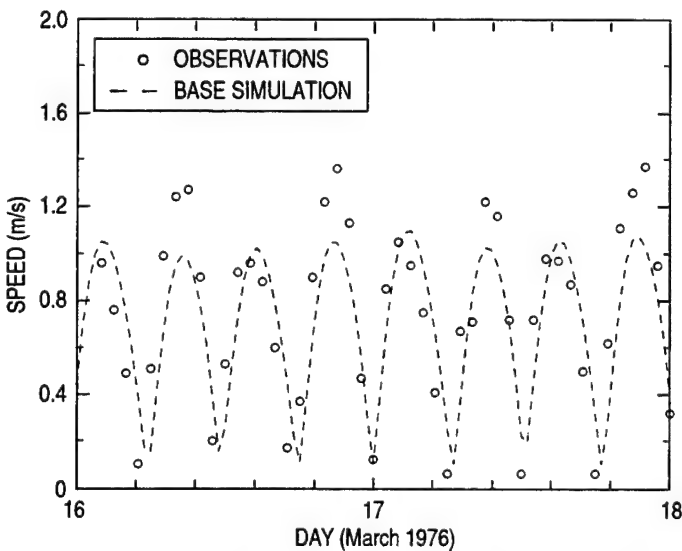


Fig. D5 — Base simulation speeds, velocity gauge 5

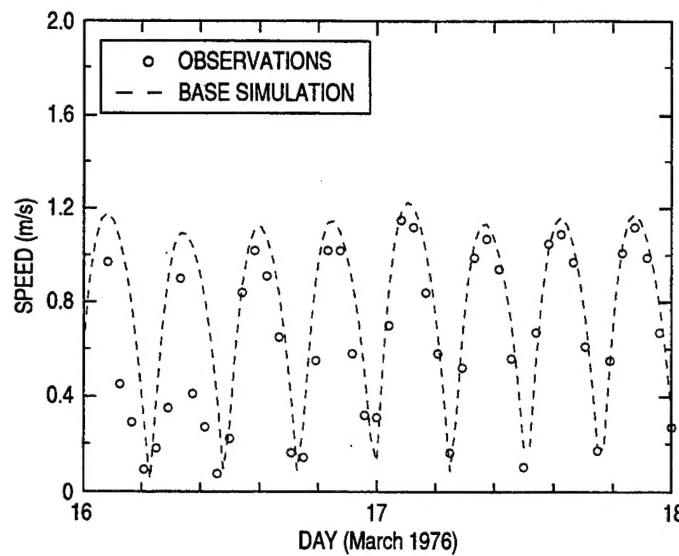


Fig. D6 — Base simulation speeds, velocity gauge 6

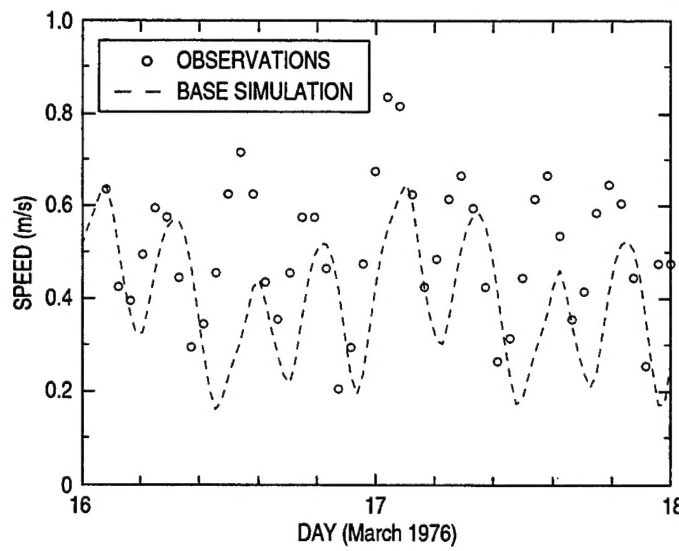


Fig. D7 — Base simulation speeds, velocity gauge 7

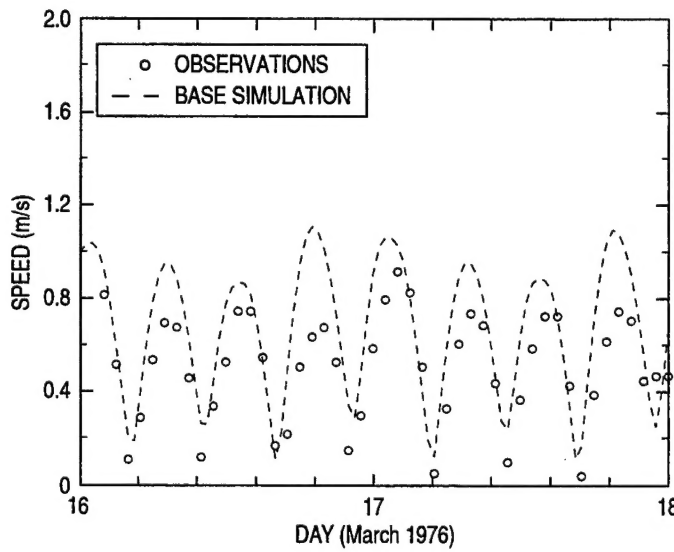


Fig. D8 — Base simulation speeds, velocity gauge 8

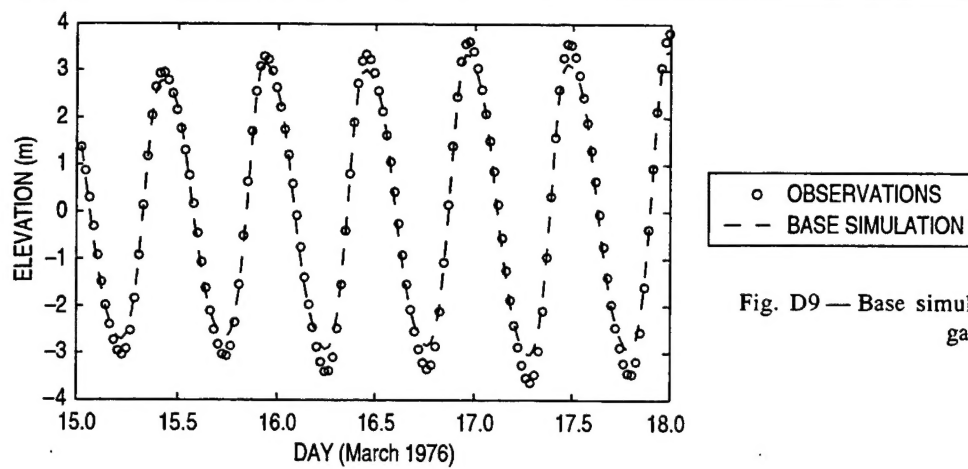


Fig. D9 — Base simulation directions, velocity gauge 1

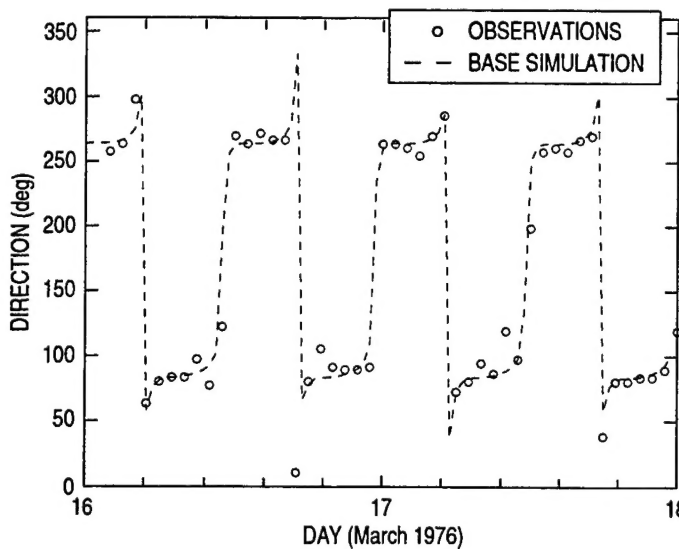


Fig. D10 — Base simulation directions, velocity gauge 2

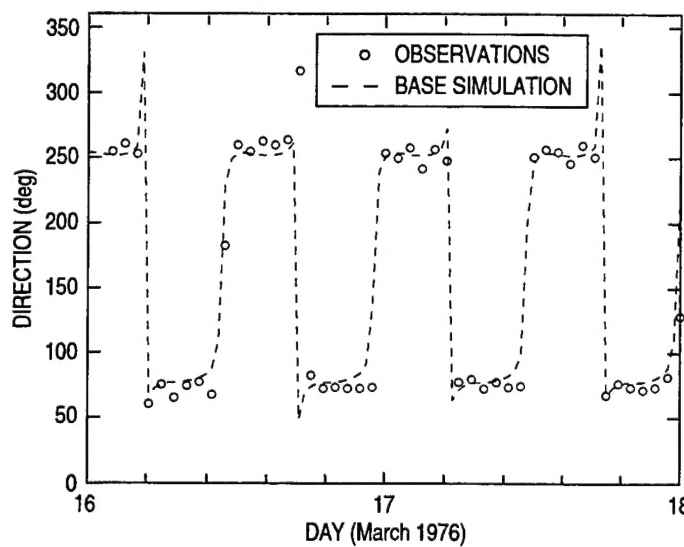


Fig. D11 — Base simulation directions, velocity gauge 3

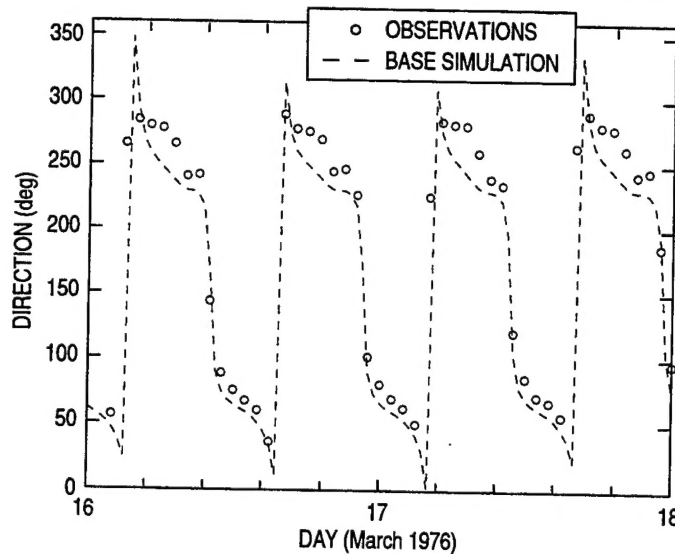


Fig. D12 — Base simulation directions, velocity gauge 4

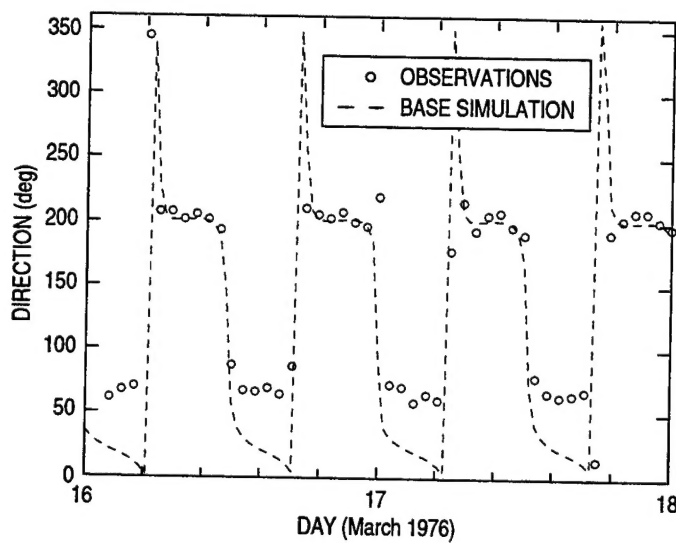


Fig. D13 — Base simulation directions, velocity gauge 5

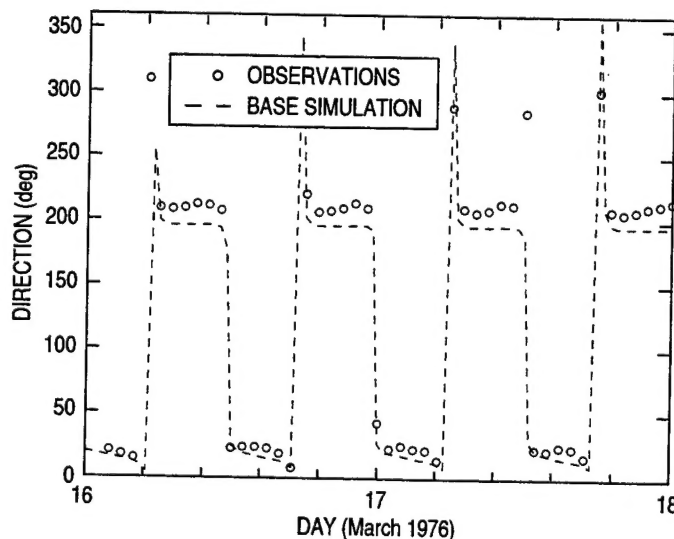


Fig. D14 — Base simulation directions, velocity gauge 6

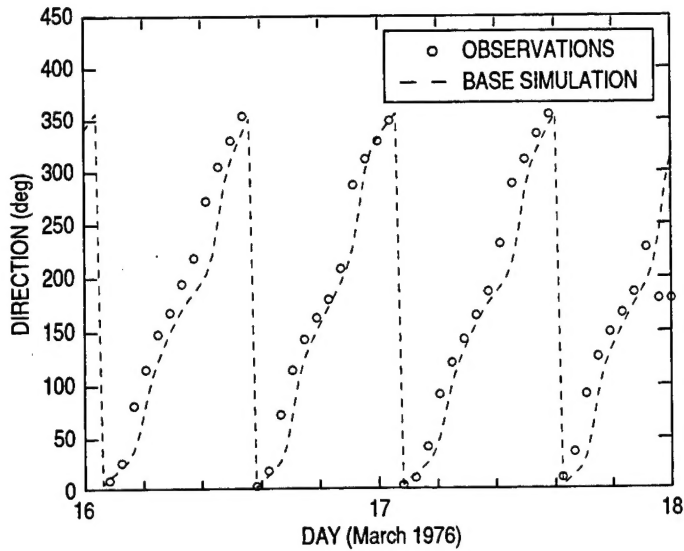


Fig. D15 — Base simulation directions, velocity gauge 7

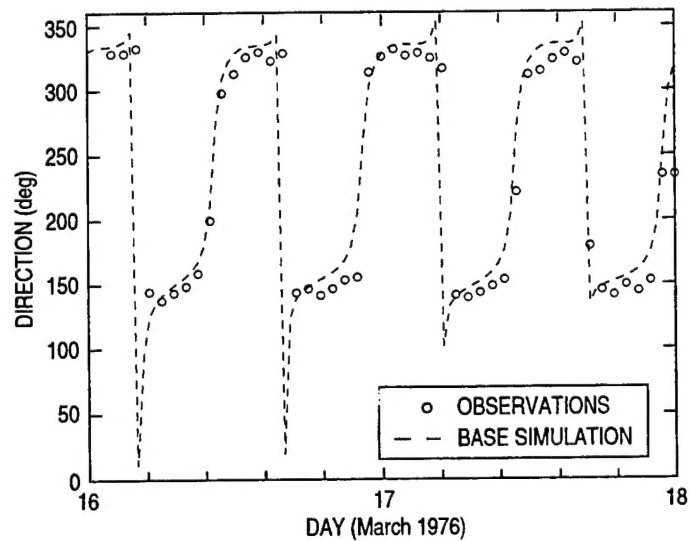


Fig. D16 — Base simulation directions, velocity gauge 8